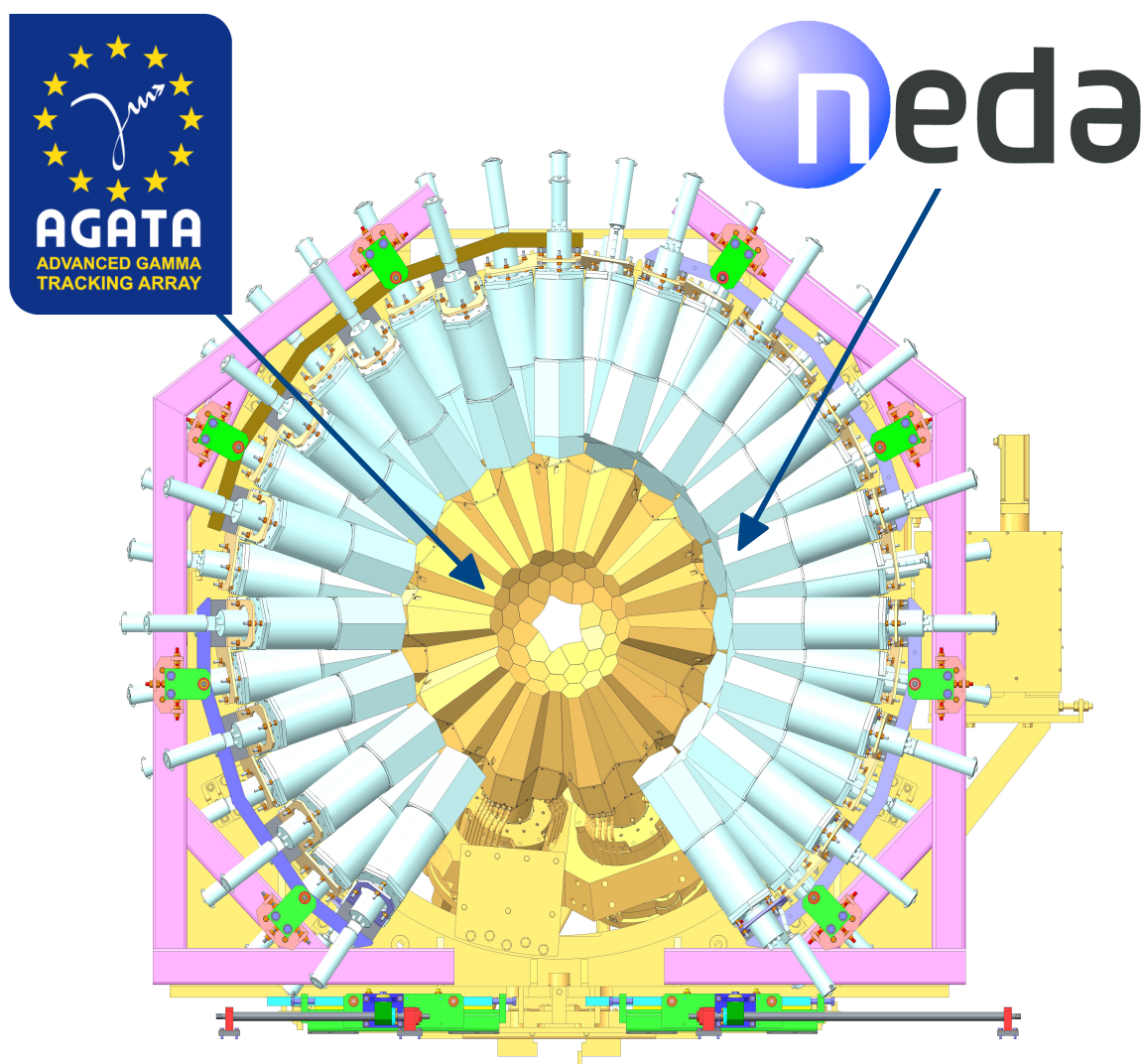


FAIR-Expert Committee Experiments (ECE)  
2014-09-30

# Technical Design Report for NEDA@HISPEC



Edited by J. Nyberg and J.J. Valiente Dobon

# Contents

<b>1</b>	<b>Executive Summary</b>	<b>4</b>
<b>2</b>	<b>Contact Person, Collaboration, Authors</b>	<b>4</b>
2.1	Contact Persons . . . . .	4
2.2	NEDA Collaboration . . . . .	4
2.3	Authors of this Report . . . . .	5
<b>3</b>	<b>Scientific Case of NEDA@HISPEC</b>	<b>5</b>
3.1	Isobaric-Analog Spin-Isospin Resonances and the Neutron Distribution in the Sn Iso- topes . . . . .	5
<b>4</b>	<b>Detector Unit: Simulations</b>	<b>8</b>
4.1	Optimum Length of the Detector . . . . .	9
4.2	Transverse Size (Diameter) of the Detector . . . . .	11
4.3	Times . . . . .	12
4.4	Comparison of BC501A and BC537 . . . . .	15
4.5	Summary and Conclusions . . . . .	16
<b>5</b>	<b>Conceptual Design of the Array</b>	<b>17</b>
5.1	Event Generator . . . . .	17
5.2	Geometries . . . . .	18
5.3	Coupling of NEDA and Neutron Wall . . . . .	19
5.4	Neutron Wall Simulations . . . . .	20
5.5	Neutron Efficiencies and Crosstalk Reduction . . . . .	21
<b>6</b>	<b>Front-End Electronics</b>	<b>23</b>
6.1	Electronics Layout . . . . .	23
6.2	Single-Ended to Differential Board . . . . .	25
6.3	Cable Transmission Features . . . . .	26
6.4	NUMEXO2 Front-End Electronics Hardware . . . . .	27
6.4.1	Power Management . . . . .	28
6.4.2	NUMEXO2 Interface . . . . .	28
6.4.3	Clock Management . . . . .	29
6.4.4	Readout Requirements . . . . .	30
6.5	Sampling FADC mezzanine . . . . .	30
6.6	LINCO2 Readout Board . . . . .	34
6.7	Global Trigger and Synchronisation System . . . . .	35
6.7.1	GTS Crate interface . . . . .	36
6.7.2	GTS Trigger Processor . . . . .	37
6.8	Basic System Firmware and Software . . . . .	38
6.8.1	Virtex-6 Firmware IPs . . . . .	38
6.8.1.1	Input interface ISERDES . . . . .	38
6.8.1.2	Data management . . . . .	39
6.8.1.3	Oscilloscope IP . . . . .	40
6.8.1.4	Inspection Lines . . . . .	40
6.8.1.5	Set-up register bank . . . . .	40
6.8.2	Virtex-5 Firmware IP and Embedded Software . . . . .	40
6.8.2.1	ADC Interface . . . . .	40
6.8.2.2	GTS leaf and PLB Cracus IPs . . . . .	41
6.8.2.3	Embedded PowerPC . . . . .	42
6.8.2.4	I/O Ethernet/PCle . . . . .	42

48	6.9 Implementation of the NEDA Trigger Algorithm . . . . .	43
49	6.9.1 Trigger Algorithms . . . . .	43
50	6.9.2 Charge-Comparison Method . . . . .	45
51	<b>7 Global Trigger and Synchronisation System</b>	<b>46</b>
52	<b>8 Data Acquisition System</b>	<b>48</b>
53	<b>9 Neutron-Gamma Discrimination with BC501A and BC537</b>	<b>49</b>
54	9.1 Scintillators . . . . .	49
55	9.2 Experiment . . . . .	49
56	9.3 Pulse-Shape Discrimination . . . . .	49
57	9.4 Summary . . . . .	52
58	<b>10 Digital Timing Measurements</b>	<b>53</b>
59	10.1 Experimental Setup and Measurements . . . . .	54
60	10.2 Results and Discussion . . . . .	56
61	10.3 Conclusions . . . . .	61
62	<b>11 Optimal Photomultiplier Tube for Neutron-Gamma Discrimination</b>	<b>62</b>
63	11.1 Experiment . . . . .	62
64	11.2 Digital CFD and Average Waveforms . . . . .	63
65	11.3 Photoelectron Yield . . . . .	63
66	11.4 Digital NGD . . . . .	64
67	11.4.1 Pulse-shape Discrimination with the CC Method . . . . .	65
68	11.4.2 Pulse-Shape Discrimination with the IRT Method . . . . .	67
69	11.4.3 TOF Verification of NGD . . . . .	69
70	11.5 Summary and Conclusions . . . . .	70
71	<b>12 Detector Unit: Prototype Design and First Tests</b>	<b>71</b>
72	12.1 Mechanical Description . . . . .	71
73	12.2 Test of Timing Performance . . . . .	72
74	12.3 Test of Neutron-Gamma Discrimination Performance . . . . .	72
75	<b>13 New Detector Materials</b>	<b>74</b>
76	<b>14 NEDA Organisation, Phases, Work Packages and Time Lines</b>	<b>74</b>
77	14.1 Organisation, management, responsible persons . . . . .	74
78	14.2 Memorandum of understanding (MoU) . . . . .	74
79	14.3 NEDA Phases and Campaigns . . . . .	75
80	14.4 Work Packages . . . . .	75
81	14.5 Time Lines and Critical Milestones . . . . .	75
82	<b>15 Cost Estimates and Expected Funding</b>	<b>76</b>
83	<b>References</b>	<b>76</b>

## 1 Executive Summary

This report describes the technical design of the neutron detector array NEDA, which will be used at the HISPEC setup together with AGATA [1], LYCCA [2] and other detectors for measurements of neutrons in the energy range from about 1 MeV to 20 MeV. The NEDA detector units will have the shape of uniform hexagonal prisms with a volume of about 3 litres, and will be filled with a liquid scintillator with good neutron- $\gamma$  discrimination (NGD) properties (BC501A or similar). The design of the units was chosen to optimise the efficiency for detection of neutrons and to have a modular setup, allowing for a placement of the detectors in various geometries and distances from the target position. The full version of NEDA will consist of 331 detector units, which e.g. can be placed at a distance of 1 m from the target position to cover a solid angle of about 50 % of  $4\pi$ .

The main characteristics of NEDA are the following:

- Efficient detection of neutrons in the energy range from 1 MeV to about 20 MeV.
- Superior neutron- $\gamma$  discrimination, which allows the detectors to be used in an environment with a high  $\gamma$ -ray background, and high count-rate capability.
- Sufficient granularity of the array to maximise the detection efficiency for neutron multiplicities larger than one.
- Modular design, which allows for a placement of the detectors in different geometries around the target, optimising neutron detection efficiency and/or neutron energy resolution.
- Advanced digital front-end electronics, which is fully compatibility with the AGATA electronics and data acquisition system.

NEDA will be used in experiments with stable and radioactive beams at NUSTAR/FAIR as well as at other European accelerator facilities, for example at SPIRAL2/GANIL and at SPES/LNL.

This design report describes the developments and construction of a NEDA array consisting of 48 detector units, which will be ready for experiments at HISPEC from 2018. The contents of the report are the following. Section 3 contains a brief summary of some of the possible physics cases to be studied with NEDA@HISPEC. Sections 4 to 8 describe the technical design of NEDA and sections 9 to 13 the performed and ongoing tests of prototypes etc. In section 14 the organisation of the NEDA project, responsibilities, work packages, time lines and critical milestones are described. The cost estimates and expected funding for NEDA@HISPEC are described in a separate document.

## 2 Contact Person, Collaboration, Authors

### 2.1 Contact Persons

Contact person for the NEDA@HISPEC project: Johan Nyberg, Uppsala University, Uppsala, Sweden  
[johan.nyberg@physics.uu.se](mailto:johan.nyberg@physics.uu.se)

Project manager of the NEDA project: José Javier Valiente Dobón, INFN-LNL, Legnaro, Italy  
[javier.valiente@lnl.infn.it](mailto:javier.valiente@lnl.infn.it)

### 2.2 NEDA Collaboration

The NEDA collaboration consists of researchers from 8 countries and more than 10 institutes. Here is a list of the institutes and local contact persons that are most actively involved in the NEDA project:



- University of Sofia, Sofia, Bulgaria, D. Tonev et al.
- GANIL, CEA/DSAM and CNRS/IN2P3, Caen, France, G. de France et al.
- INFN-LNL, Legnaro, Italy, J.J. Valiente Dobón et al.
- Heavy Ion Laboratory, University of Warsaw, Warsaw, Poland, M. Palacz et al.
- National Centre for Nuclear Research, Otwock-Swierk, Poland, M. Moszyński et al.
- IFIC, CSIC University of Valencia, Valencia, Spain, A. Gadea et al.
- Uppsala University, Uppsala, Sweden, J. Nyberg et al.
- Faculty of Engineering and Natural Sciences, Istanbul Sabahattin Zaim University, Istanbul, Turkey, M.N. Erduran et al.
- STFC Daresbury, Daresbury, UK, John Simpson et al.
- University of York, York, United Kingdom, R. Wadsworth et al.

## 2.3 Authors of this Report

Contributions to this report were made by the following persons:

J. Agramunt, G. de Angelis, F.J. Egea, M.N. Erduran, S. Ertürk, G. de France, A. Gadea, V. González, T. Hüyük, M. Jastrzab, G. Jaworski, X.L. Luo, V. Modamio, M. Moszyński, Q. Nishada, A. Di Nitto, M. Palacz, A. Da Re, E. Sanchis, P.-A. Söderström, D. Tonev, A. Triossi, M. Tripon, R. Wadsworth.

## 3 Scientific Case of NEDA@HISPEC

At HISPEC, NEDA will be used for experiments with exotic secondary beams from the Super-FRS. In the regime of low-energy beams, from about 4 MeV/A to 10 MeV/A, fusion-evaporation and multi-nucleon transfer reactions will be utilised. A “classical” setup of AGATA placed in the backward and NEDA in the forward angles around the secondary target is foreseen.

With medium-energy beams, in the range from 10 MeV/A to 100 MeV/A, possible physics cases are studies of proton-rich nuclei along the  $N = Z$  line using inverse kinematics one- and two-proton transfer reactions  ${}^2\text{H}(X, n)Y$  and  ${}^3\text{He}(X, n)Y$ , respectively, and the deuteron transfer reaction  ${}^3\text{H}(X, n)Y$ . Such reactions produce low- to intermediate-energy neutrons, which are emitted in the forward hemisphere.

With high-energy secondary beams, in the range from 100 MeV/A to 200 MeV/A, inverse kinematics charge-exchange reactions  $p(X, n)Y$  for studies of Gamow-Teller and Isobaric-Analog Resonances and neutron-skin effects in neutron-rich nuclei are of interest. This type of reaction would lead to low-energy neutrons (1 MeV to 10 MeV) being emitted around  $90^\circ$  and would be very suitable for a setup with AGATA placed in the forward hemisphere and NEDA around  $90^\circ$ . A more detailed description of a possible first-day NEDA@HISPEC experiment of this type, presented as a letter-of-intent, is given in the following section.

### 3.1 Isobaric-Analog Spin-Isospin Resonances and the Neutron Distribution in the Sn Isotopes

The availability of radioactive nuclear beams of good intensity and optical quality makes possible the use of charge exchange nuclear reactions to investigate fundamental properties such as the nuclear

matter distribution, deformation and the evolution of shell structure very far from stability. The predicted reduction in the spin-orbit term in the nuclear force with increasing neutron excess is believed, together with the tensor component of the residual nucleon-nucleon interaction, to be the main origin of the changes in the single particle energies of intruder states and of the shell quenching effects.

We propose to investigate using the NEDA detector and the FAIR beams, the energy values of the Gamow-Teller and Isobaric-Analog resonances for various isotopic chains. Such information is directly linked to the evolution of the spin orbit term for increasing  $N/Z$  ratios as well as to the difference in slope between neutron and proton radii.

In recent years experiments with radioactive beams from projectile fragmentation facilities have revealed the presence of a neutron halo in several of the lightest nuclei on the neutron drip line. These structures arise when the last one or two neutrons are in low angular momentum orbits and close to the top of the potential well so that their wave functions have very extended distributions, which is manifested in an anomalously large matter radius. In heavy nuclei several calculations predict a different phenomenon to occur. An excess of several neutrons build up so that the neutron density extends out significantly further than that of protons, resulting in a mantle of dominantly neutron matter (see illustration in Fig. 1). The presence of such neutron skin is expected to affect collective modes of nuclear excitation which involve the out-of-phase motion of neutrons against protons, such as the Giant Dipole Resonance (GDR) and the scissors mode. There is also the possibility of a soft dipole mode in which the core nucleus moves against the more weakly bound skin neutrons. Due to the different slope of the neutron density distribution for larger  $N/Z$  ratios, one expects specific terms of the nucleon-nucleon residual interaction, like the spin-orbit term, to be strongly affected or reduced [3, 4, 5, 6].

## THE NEUTRON SKIN

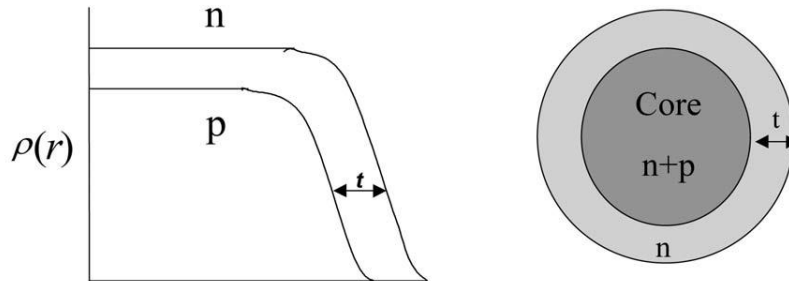


Figure 1: Schematic illustration of the neutron skin. For more extended neutron distributions one expects a reduction of the spin-orbit term of the residual nucleon-nucleon interaction [7].

The predicted reduction in the spin-orbit term in the nuclear force with increasing neutron excess is believed, together with the tensor component of the residual nucleon-nucleon interaction, to be the main origin of the changes in the single particle energies of intruder states and of the shell quenching effects.

One of the ways of investigating the difference in slope between the radii of the neutron and proton density distributions along an isotopic chain is based on the measurement of the excitation energies of the Gamow-Teller resonances (GTR) relative to the isobaric-analog states (IAS) [8]. Nucleons with spin-up and spin-down can oscillate either in phase (spin scalar  $S = 0$  mode) or out of phase (spin vector  $S = 1$  mode). The spin vector, or spin-flip excitations can be of isoscalar ( $S = 1$ ,  $T = 0$ ) or isovector ( $S = 1$ ,  $T = 1$ ) nature. These collective modes provide direct information on the spin and spin-isospin dependence of the effective nuclear interaction. Especially interesting is

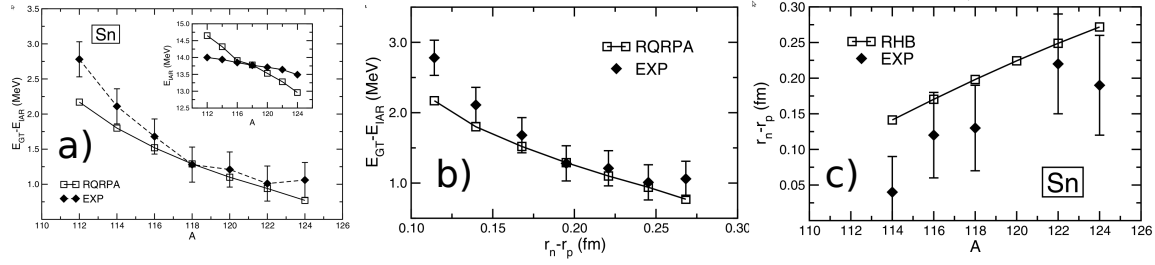


Figure 2: a) The energy difference between the main component of the GTR and the respective IAS for the stable  $^{112-124}\text{Sn}$  isotopes extracted from Ref. [8]. The experimental data are compared with the results of relativistic quasi-particle random phase approximation model. In the inset the calculated excitation energies of the isobaric analog states are compared with the experimental results. b) The calculated and experimental energy differences between GTR and IAS as a function of the calculated differences between the RMS radii of the neutron and proton density distributions of the even-even Sn isotopes [8]. c) The calculated differences between neutron and proton RMS radii compared with the available experimental data.

the collective spin-isospin oscillation with the excess neutrons coherently changing the direction of their spin and isospin without changing their orbital motion, the GTR with spin-parity  $J^\pi = 1^+$ .

The simplest charge exchange excitation mode, however, does not require the spin-flip (i.e.  $S = 0$ ) and corresponds to the well known IAS with spin-parity  $J^\pi = 0^+$ . The spin-isospin characteristics of the GTR and the IAS are related through the Wigner super-multiplet scheme. The Wigner  $SU(4)$  symmetry implies the degeneracy of the GTR and IAS, the resonances completely exhausting the corresponding sum rules. The Wigner  $SU(4)$  symmetry is, however, broken by the spin-orbit term of the effective nuclear potential. Therefore, the energy difference between the GTR and the IAS is expected to reflect the magnitude of the effective spin-orbit potential. Such dependence and the related effects on the proton and neutron average nuclear radii has been investigated in Ref. [8]. Fig. 2a from Ref. [8] shows the energy difference between the main component of the GTR and the respective IAS for the stable  $^{112-124}\text{Sn}$  isotopes. The experimental data are compared with the results of relativistic quasi-particle random phase approximation model. One notices the systematic reduction of the energy differences when moving towards larger  $N/Z$  ratios. Fig. 2b shows the same quantity as a function of the calculated differences between mean neutron and proton radii as well as the systematic dependence of these for increasing mass number in Fig. 2c.

In this letter-of-intent it is proposed to investigate the energy differences between the GTR and the IAS resonances in different isotopic chains, e.g. in the chain of tin isotopes  $^{128-134}\text{Sn}$ . Such information will allow probing the strength of the spin orbit term of the nucleon-nucleon residual interaction as a function of the  $N/Z$  ratio and therefore the mean proton and neutron radii. To populate the GTR and IAS resonances (p, n) reactions have been largely utilised, see Fig. 3. Thus, the charge exchange reaction (p, n) in inverse kinematics [9] is proposed to be used.

Fig. 3 from Ref. [9] shows the  $^3\text{H}$  energy spectra obtained in the  $^{118}\text{Sn} (^3\text{He}, t)^{118}\text{Sb}$  reaction at a beam energy of 200 MeV. The beams of  $^{128-134}\text{Sn}$ , produced by the FAIR RIB facility at energies of about 300 MeV/u, will impinge on a  $\text{H}_2$  target. The neutrons will be detected at about  $90^\circ$  with energies of a few MeV using the NEDA detectors. From the scattering angle and the TOF measurements the velocity vector and the recoil energy information will be reconstructed with a resolution of about 5% sufficient to identify the centroid of the GDR. The production rates of the secondary beams  $^{128-134}\text{Sn}$  at the target position are expected to be in the order of  $10^5$  atoms/s to  $10^8$  atoms/s.

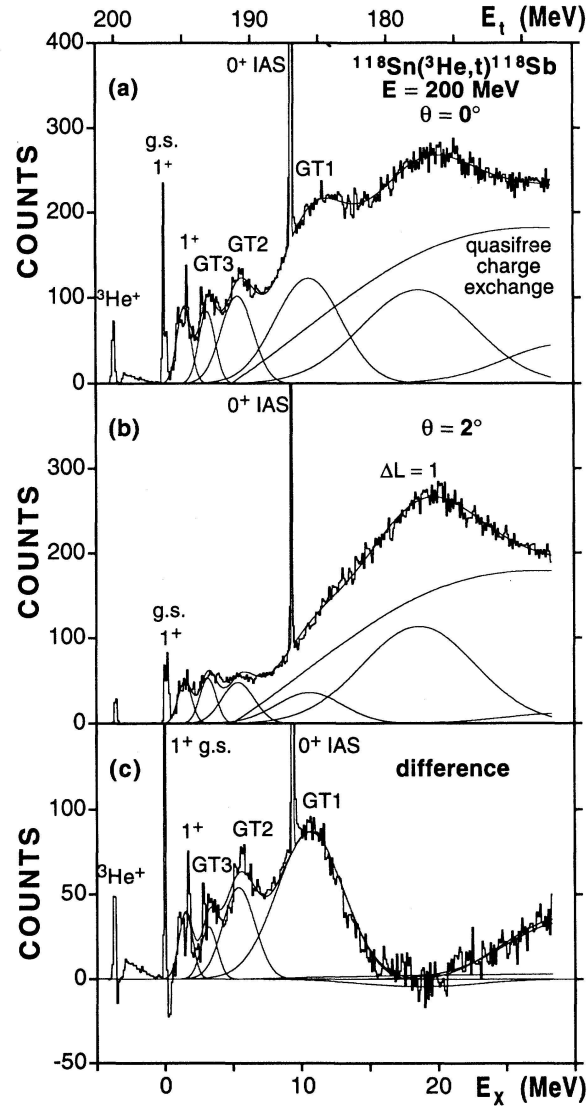


Figure 3:  ${}^3\text{H}$  energy spectra from Ref. [9] for the  ${}^{118}\text{Sn}({}^3\text{He}, t){}^{118}\text{Sb}$  reaction at a beam energy of 200 MeV at (a)  $\theta = 0^\circ$  and (b)  $\theta = 2^\circ$ . (c) shows the difference between (a) and (b). The IAS and GTR resonances are clearly visible. For more details see Ref. [9].

## 4 Detector Unit: Simulations

In this section, the simulations performed to find the optimal size of the NEDA detector unit are described. Two different types of liquid scintillators, the standard proton-based BC501A and the deuterated liquid BC537, were simulated and compared. This work has been published in [10] and the main results are given here. In Ref.[10], the studied neutron energy range was 1 MeV to 10 MeV, which is typical for fusion-evaporation reactions. An extension of the results and conclusions from that paper to be valid up to 20 MeV, which is the maximum neutron energy considered in this TDR, can safely be made.

The GEANT4 framework [11] was the selected tool for the simulations, due to its flexibility and the possibilities to include a large number of different materials and detector shapes. NEDA will be used together with other detector arrays, in particular with AGATA, for which a GEANT4 model exists [12]. The simulations that are presented here were performed using the AGATA simulation

code [12], which is based on GEANT4 and which greatly facilitates combining different devices in one simulation.

Experimentally, neutron detectors count (register) neutrons (or  $\gamma$  rays) if the amplitude of the signal from the PMT exceeds a certain level. The time of the detection is determined using for example a constant fraction discriminator (CFD). A similar procedure was applied in the simulation taking into account that each neutron usually interacts many times in the detector volume. In order to reproduce the experimental situation as close as possible, the interactions were first sorted timewise, then summed up incrementally. The “detection” time of the signal produced is defined as the time when the light produced in the detector exceeds the assumed threshold. In the following discussion, the term *significant interaction*, which refers to a series of interactions leading to a signal above threshold, is used. A threshold of 50 keVee is assumed for the calculations presented in this work.

#### 4.1 Optimum Length of the Detector

In the attempt to find an optimum size of the NEDA detector modules, a systematic study was performed to determine the length of the scintillator detector that is needed in order to register a significant interaction.

A pencil beam of monochromatic neutrons was shot into a scintillator cylinder with a 50 cm diameter and variable length. No detector walls were included in this simulation and the neutron detection efficiency was analysed as a function of the length of the cylinder. The efficiency to detect a neutron, was defined as  $\epsilon_n = N_{\text{detected}}/N_{\text{emitted}}$ , where  $N_{\text{emitted}}$  and  $N_{\text{detected}}$  are the number of neutrons which were emitted and which created a significant interaction, respectively. The diameter was deliberately chosen to be rather large (50 cm), so that the detection probability depended only on the cylinder length and was not influenced by a limitation of the diameter. The results of this study are presented in Figure 4.

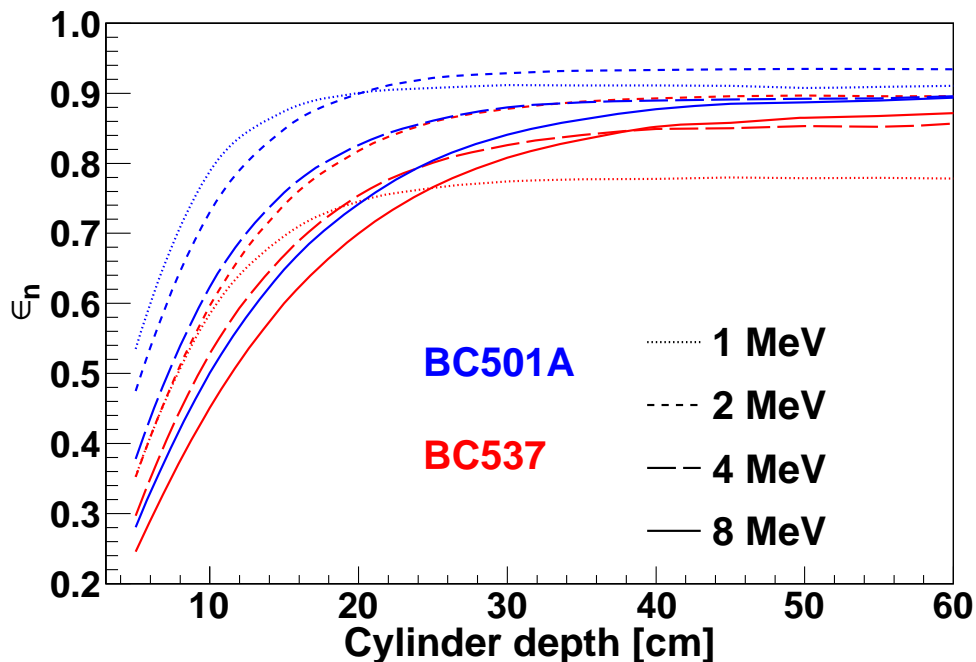


Figure 4: Neutron detection efficiency ( $\epsilon_n$ ) as a function of the cylinder depth (= length) for the two scintillators BC501A (blue lines) and BC537 (red lines) and for 1 MeV, 2 MeV, 4 MeV and 8 MeV neutrons.

The neutron detection probability as a function of the cylinder length reaches a constant value of about 80 % to 95 %, at a cylinder length of 20 cm to about 40 cm depending on the neutron

energy and the type of the scintillator. A further increase of the detector length does not lead to a significant increase of the detection probability. Reaching an efficiency of 100 % is not possible, because in some events neutrons lose energy in reactions which do not produce enough light to exceed the threshold.

The depth distributions of the significant interactions were also analysed. The results shown in Fig. 5 corroborate the above observations based on Fig. 4. The majority of the interactions take place within the first layers of the scintillator (depending on the neutron energy), but the tails of the depth distributions are large, thus the thickness of the scintillator necessary to detect almost all neutrons is also large (compare Fig. 4). The lowering of the mean significant interaction depth at 4 MeV (see insert of Fig. 5) is attributed to the fact that elastic scattering on carbon becomes significant only at this energy (carbon nuclei moving in the scintillator are finally able to produce enough light). Thus, the total interaction cross section increases at about 4 MeV. In turn, at 5.561 MeV the  $^{12}\text{C}(n,\alpha)^9\text{Be}$  reaction channel opens, but the products of this reaction need another 2 MeV to 3 MeV of kinetic energy to be detected, and therefore the significant interaction depths become smaller only at about 8 MeV.

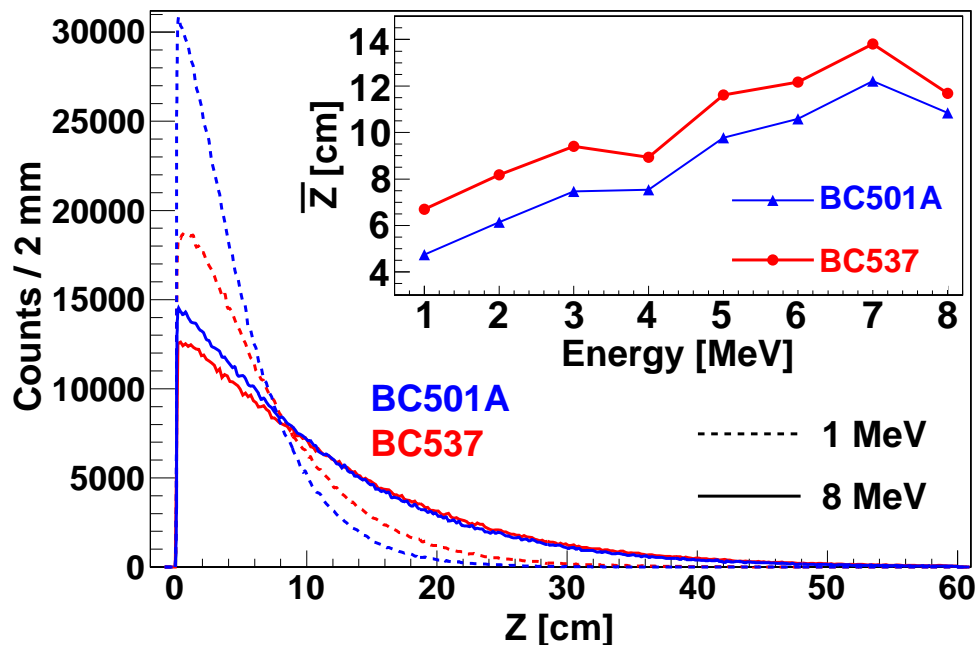


Figure 5: Distributions of the depth of the significant interaction ( $Z$ ) for two neutron energies and two scintillators, BC501A and BC537. The type of the scintillator is marked with blue and red lines for BC501A and BC537, respectively. The line pattern marks the neutron energy as shown in the legend. A total of  $10^6$  neutrons were simulated in each case. The insert shows the dependence of the mean significant interaction depth ( $\bar{Z}$ ) on the neutron energy. Lines connecting the points in the insert are drawn only to guide an eye.

The conclusion regarding the length of the detector unit is that for most of the neutrons emitted with energies up to about 10 MeV the maximum of the detection efficiency will be reached at a detector length of 20 cm to 30 cm. Increasing the detector length by another 10 cm or 20 cm would lead to slightly larger efficiency for the fastest neutrons. Two additional factors should, however, also be taken into account in determining the optimum length of the detector. The first one is the influence of the detector length on the probability that one neutron generates a signal in more than one detector. This is discussed further in section 4.2. The second factor is the relation of the detector size to the quality of the NGD. This effect was not studied in the present work, but the results presented in Ref. [13] indicate that the discrimination deteriorates for larger detectors.

## 4.2 Transverse Size (Diameter) of the Detector

Neutrons undergo significant interactions mainly along the axis of their incoming direction. Distributions of the significant interaction with respect to this axis are shown in Fig. 6. After the first interaction, a scattered neutron may however produce another significant interaction, which is located far away from the initial axis, usually in another detector module. In order to study the distribution of such second significant interactions a setup was evaluated consisting of two coaxial detectors, an inner and an outer detector as shown in Fig. 7. Such a setup is a good representation of a detector module surrounded by a number of other modules, with unimportant geometrical details omitted.

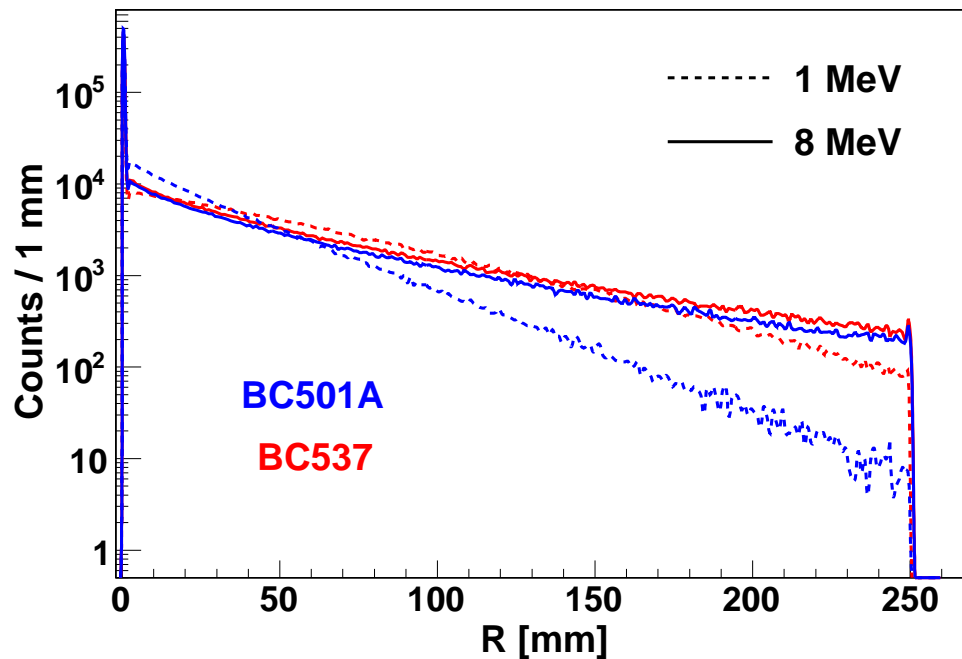


Figure 6: Distribution of the distance ( $R$ ) between the position of the first significant interaction and the axis of the incoming neutrons. The results of the simulations for two neutron energies (1 MeV and 8 MeV) are shown with blue and red lines for the two scintillators, BC501A and BC537, respectively. A pencil beam of  $10^6$  neutrons were shot into the centre of the cylindrical detector in each of the presented cases.

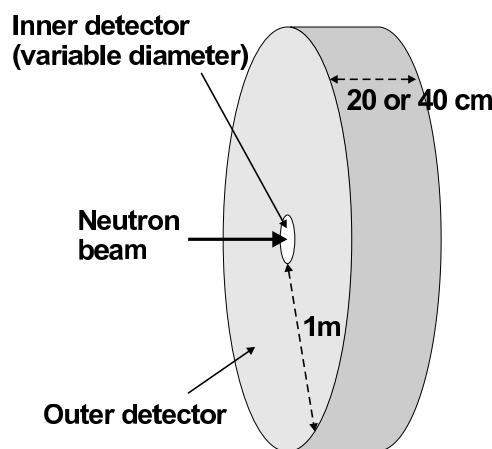


Figure 7: Setup used in the evaluation of the probability that one neutron generates a signal in more than one detector module.

A pencil beam of monochromatic neutrons was directed to the centre of the inner detector. The

probability to register a significant interaction in the outer detector was evaluated for events in which the central detector fired, with the inner cylinder diameter varied within the range from 5 cm to 30 cm. The outer detector had a fixed radial thickness of 1 m and two different thicknesses were used for the inner and outer detectors: 20 cm and 40 cm (see Fig. 7). The results are shown in Fig. 8. The plotted values are defined as  $P_{1n \rightarrow 2n} = N_2/N_1$ , where  $N_1$  and  $N_2$  are the number of neutrons which gave significant interactions in the inner cylinder and in both cylinders, respectively.

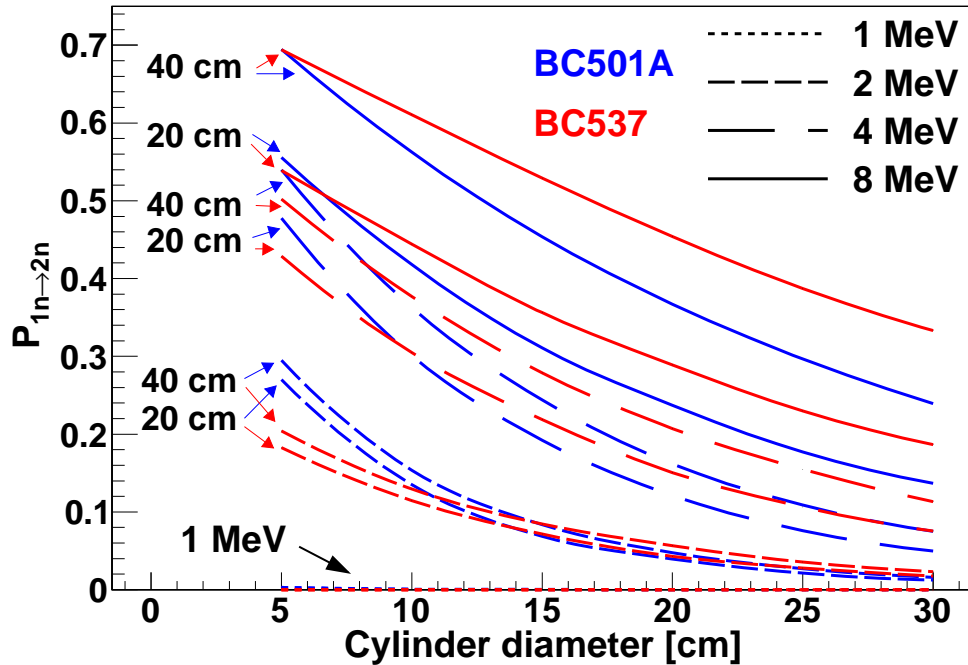


Figure 8: Crosstalk probability,  $P_{1n \rightarrow 2n}$ , as a function of the cylinder diameter. Four sets of lines, corresponding to neutron energies 1 MeV, 2 MeV, 4 MeV and 8 MeV, are shown for each of the two scintillators, BC501A and BC537 in blue and red, respectively. Cylinders with two lengths, 20 cm and 40 cm, were used and the respective lines are marked with text labels and arrows.

Fig. 8 indicates that  $P_{1n \rightarrow 2n}$  is reduced rather slowly with the inner detector diameter. For any practical detector diameters the  $P_{1n \rightarrow 2n}$  values will be large and if  $P_{1n \rightarrow 2n}$  values below 1 % are required (compare Ref. [14]) additional cleaning conditions of the interactions in two detectors cannot be avoided.

The  $P_{1n \rightarrow 2n}$  values are significantly larger for longer detectors, for all energies and for both scintillators. The BC501A scintillator gives larger  $P_{1n \rightarrow 2n}$  values than BC537 for the smallest diameters, but this relation inverts with the increase of the diameter, depending also on the energy of neutrons.

### 4.3 Times

A larger detector may in principle have worse time resolution. This may also impose an important limitation on the detector size, as the TOF parameter is used to distinguish neutrons and  $\gamma$  rays detected in the scintillator as well as for the 1n/2n discrimination. Two different components contribute to the time resolution of a neutron detector:

- intrinsic time resolution, related to the time required to produce and collect the light signal in the scintillator and to the electronic jitter;
- varying TOF due to a distribution of significant interaction depths in a thick detector.

The intrinsic time resolution cannot be evaluated in present simulations, as light production processes and light transportation are not included in the model. It was, however, experimentally shown in



Ref. [15] that the intrinsic resolution of BC501A detectors does not significantly vary with the cylindrical detector length. A value of about 1.5 ns was obtained.

The TOF of a cylindrical detector (the same one as described in Sec. 4.1) was evaluated as a function of the cylinder length. The widths of the TOF distributions are presented in Fig. 9. Here, the intrinsic time resolution of the detector was not taken into account, and the presented values reflect only the variations of the interaction depths.

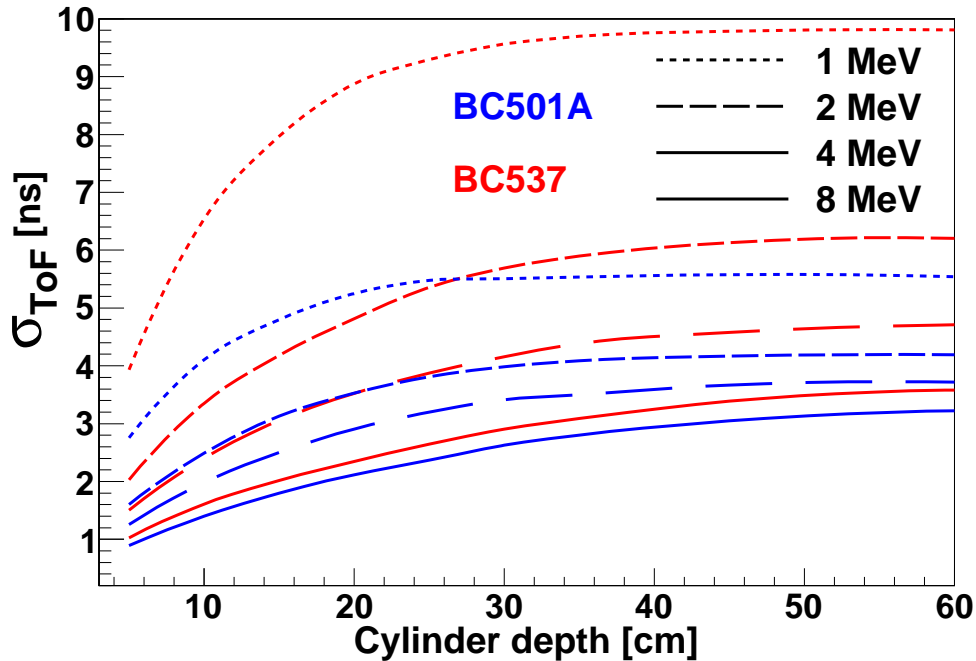


Figure 9: Width (one standard deviation) of the TOF distributions as a function of the cylinder length for BC501A (blue lines) and BC537 (red lines), and for 1 MeV, 2 MeV, 4 MeV, and 8 MeV neutrons.

The width of the TOF distributions as a function of detector length initially rises rather steeply, while for longer cylinders (above 30 cm) it saturates at a certain value. Thus, the simulations do not indicate any limit on the detector length imposed by the TOF resolution. Larger neutron energies lead to smaller TOF variations, which is due to the fact that for a faster particle, variations in the significant interaction depth are less important in terms of TOF. Filling the detector with the BC537 scintillator liquid results in a significantly worse TOF resolution than in the case of BC501A.

Timing effects are important for the  $P_{1n \rightarrow 2n}$  probability. Neutrons interacting in the scintillator usually undergo a series of elastic interactions with the nuclei of the medium and then thermalise or escape from the detector. Thus, light is mostly produced within a few nanoseconds after the neutron enters the detector. Scattering of thermalise neutrons in the scintillator may, however, continue for much longer times (up to milliseconds). If a thermalise neutron is captured by a proton, this leads to a very late light flash, due to the registration of the  $\gamma$  ray emitted in this process. Such effects are more significant for the BC501A scintillator than for BC537, because the cross section for the  $p(n,\gamma)d$  interaction is much larger than for  $d(n,\gamma)t$ . This is illustrated in Fig. 10, which shows times of the interaction in the outer detector of the setup shown in Fig. 7. Indeed, for BC501A, a significant interaction in the outer detector either happens within the first 100 ns or much later with an almost flat distribution up to hundreds of  $\mu$ s. The corresponding spectrum for the BC537 scintillator shows no such late light-flash effect.

The late light flash is often produced far from the initial neutron interaction point, i.e. usually in another detector module. Thus, the BC501A scintillator seemingly shows much larger  $P_{1n \rightarrow 2n}$  values than BC537, if light collection is not limited in time. This is illustrated in Fig. 11 in which  $P_{1n \rightarrow 2n}$

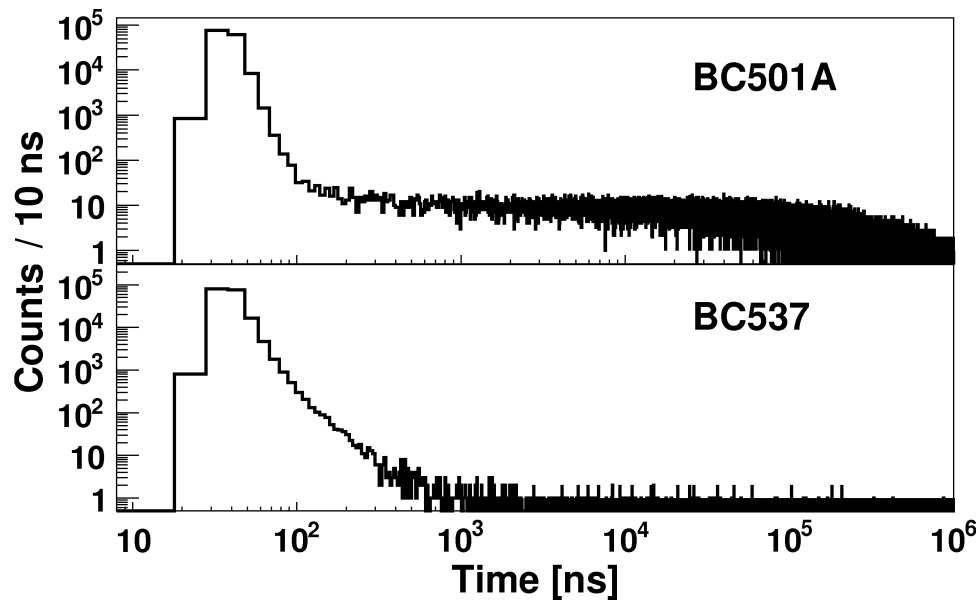


Figure 10: Times of the significant interaction in the outer detector of the two scintillators shown in Fig. 7. A source of 2 MeV neutrons was placed 51 cm in front of the detectors and the time measurement starts when a neutron is emitted from the source. The detectors were 20 cm long and the diameter of the inner detector was 12.7 cm.

values of the two scintillators are compared for calculations with and without a 100 ns time limit for the significant interaction. This indicates the importance of properly setting time limits on the collection of neutron signals, both in experiments and in simulations. For the efficiency and  $P_{1n \rightarrow 2n}$  evaluations presented in this paper, a time limit of 100 ns from the emission of neutrons or  $\gamma$  rays to the first significant interaction was used. Light produced in each detector volume was integrated during 300 ns after the significant interaction.

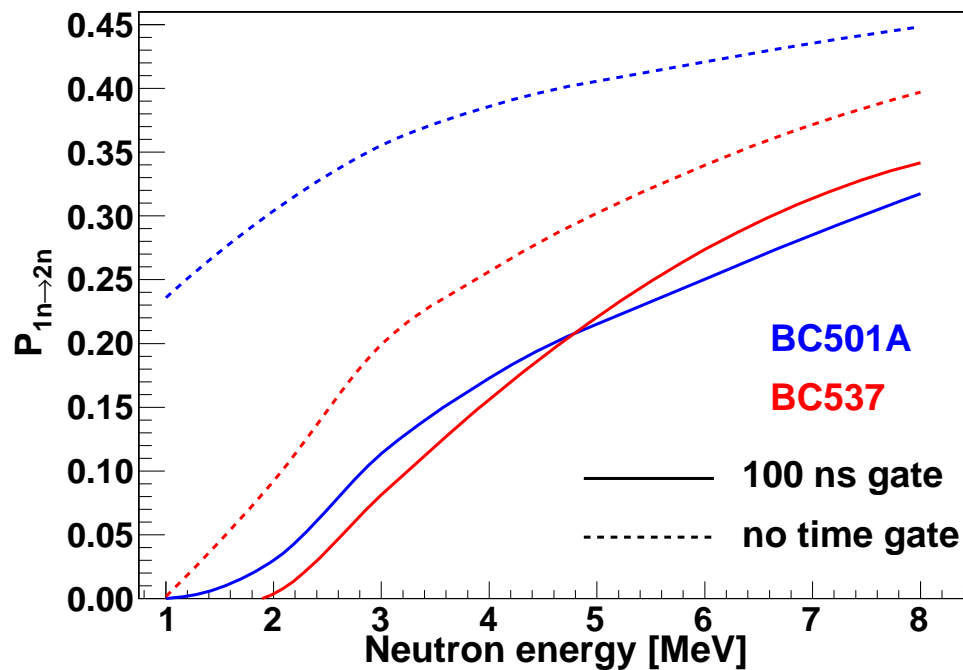


Figure 11: Influence of the 100 ns detection time limit on the  $P_{1n \rightarrow 2n}$  probability.

#### 4.4 Comparison of BC501A and BC537

As mentioned before, the elsewhere reported advantage of the deuterated scintillator (BC537) is its ability to give a better detector response, i.e. signals which are more proportional to the energy of the incoming neutron, than scintillators based on  $^1\text{H}$  (like BC501A). Fig. 12 shows simulated light spectra produced by a pencil beam of 2 MeV neutrons interacting in two cylindrical detectors filled with BC501A and BC537, of two different sizes: a small detector with a 5 cm diameter, a 5 cm length and a volume of 0.1 litre and a large one with a diameter of 12.7 cm, a length of 20 cm and a volume of 2.5 litre. The large detector has a size similar to the size of the NEDA detector module. It can be seen in Fig. 12a that the small BC537 detector indeed gives a pronounced bump corresponding to the incident neutron energy. This bump is not seen in the histogram of the small BC501A detector. However, in the big detector (Fig. 12b), events in which most of the neutron energy is transferred to the scintillator medium in one interaction are relatively rare, and no advantage related to the angular distributions of a single neutron scattering can be observed. Instead, events with multiple neutron interactions dominate, leading to very similar shapes of the spectra for both scintillators. The main difference is that less light is produced in BC537 than in BC501A.

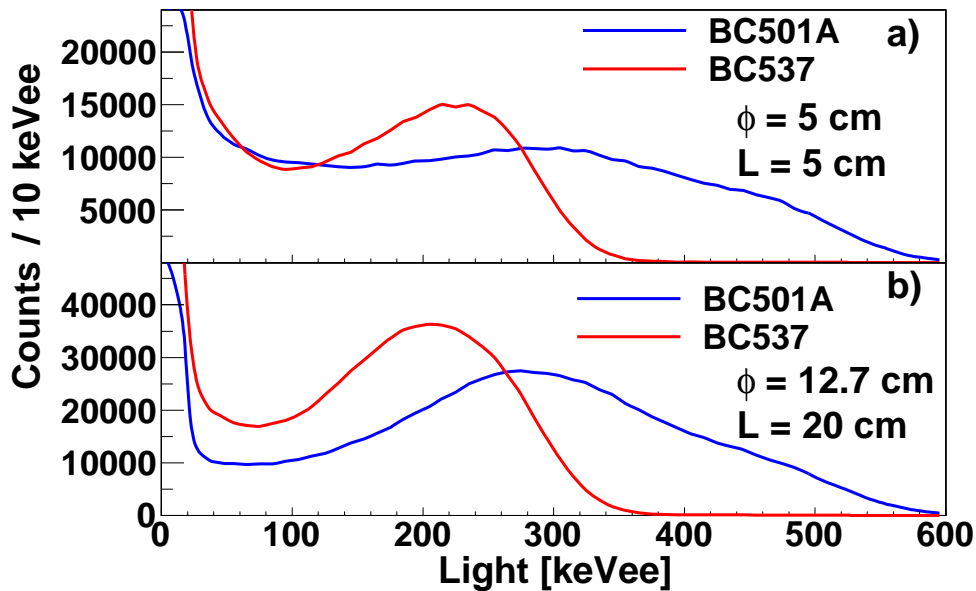


Figure 12: Light produced by a pencil beam of 2 MeV neutrons in two cylindrical BC501A and BC537 detectors of different size: a) a small and b) a large detector. The dimensions of the detectors are shown in the legends.

It has already been shown (Fig. 4), that the BC537 scintillator has a lower efficiency than BC501A. The difference between the two scintillators is additionally illustrated in Fig. 13 in which the detection probability for the cylindrical detector is plotted as a function of neutron energy. Note that at low neutron energies, below 1 MeV, the efficiency difference between the two scintillators is very significant.

It should be pointed out that the observed difference between the two scintillators comes mainly from the higher cross section for the neutron interaction with protons than with deuterons. In addition, there is relatively more carbon in BC537 ( $\text{C}_6\text{D}_6$ ) than in BC501A ( $\text{C}_8\text{H}_{10}$ ) and interactions on carbon give very little light. Also, less light is produced per MeV by deuterons than by protons. Thus, the results of the simulations are easily explained by the physical properties of the scintillation material. A smaller amount of light also results in broader TOF distributions. As far as the  $P_{1n \rightarrow 2n}$  probability is concerned, both detectors exhibit similar behaviour, except for the situations when the efficiency of BC537 is too low to register two significant interactions. Thus, based on the simulations presented here, there is no advantage of using the deuterated scintillator instead of the standard

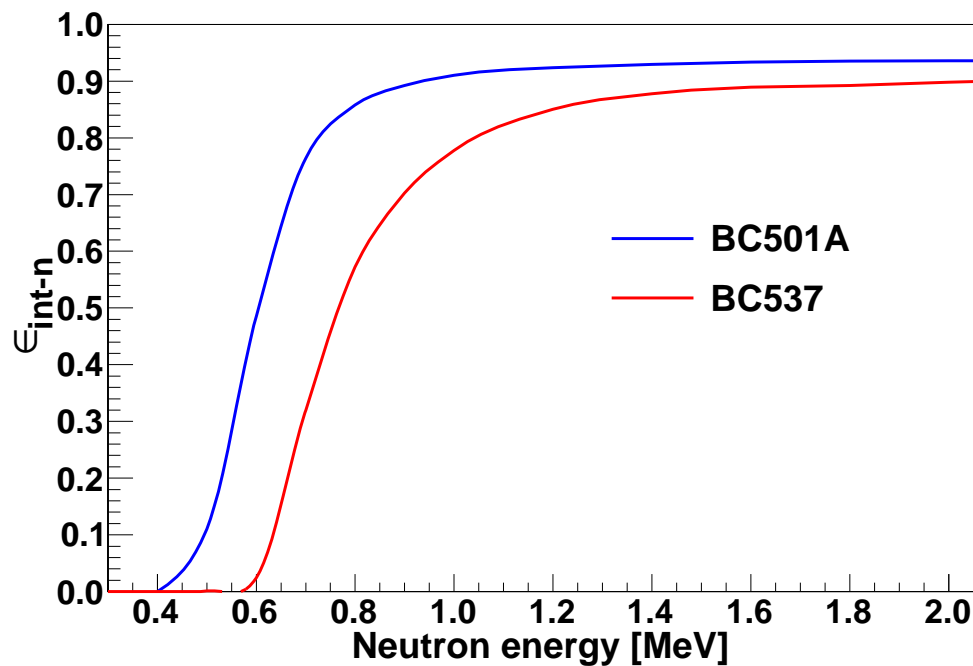


Figure 13: Neutron detection efficiency as a function of neutron energy for the two scintillators BC501A and BC537. The detector had a diameter of 50 cm and was 60 cm long.

one.

## 4.5 Summary and Conclusions

The evaluation of the reliability of the `GEANT4` neutron interaction model lead to the conclusion that this code can be used for NEDA type simulations, although deficiencies of inelastic processes on  $^{12}\text{C}$  and  $^2\text{H}$  can still be identified. The credibility of the `GEANT4` neutron interaction model was concluded after comparing the results of simulations with real detector measurements.

Based on the calculations presented in this work, the conclusion is that a detector with a length of 20 cm is sufficient for detection of neutrons with energies up to about 10 MeV. A longer detector would give only a marginal increase of the efficiency, with a larger probability for a single neutron to generate signals in more than one detector and a possibly worse NGD capability.

A significant fraction of detected neutrons will create a second signal in detectors situated far away from the initial interaction point. Thus, there is little profit in using detectors of the small transverse dimension (diameter). Note that the NEDA array will be situated about 1 m from the neutron emission point (a target) and will cover a solid angle of up to  $2\pi$ . A small transverse dimension would then lead to a huge number of the detector modules, which should be avoided, if it is not especially justified. Therefore, the diameter of the detector should be as large as practically possible, and this means using detectors of about 5 inch diameter, which is the size of the largest PMTs commonly available. An array covering  $2\pi$  of the solid angle and located at a distance of 1 m from the target will consist of about 400 such detectors.

The simulations presented here do not indicate any advantage of using a deuterated scintillator instead of the standard  $^1\text{H}$ -based one.

## 5 Conceptual Design of the Array

In this section, the conceptual design of the NEDA array is presented. A more detailed report regarding this work will be published in Ref. [16].

### 5.1 Event Generator

The simulations have been performed both with the internal event generator of GEANT4 and with LILITA [17].

Neutrons with an energy distribution corresponding to a  $^{252}\text{Cf}$  source were produced using the internal event generator of GEANT4 and with an emission probability as a function of energy according to the expression [18]

$$N(E) = E^{1/2} e^{-E/T}. \quad (1)$$

The energy distribution corresponding to this equation, with  $T = 1.42 \text{ MeV}$  is shown in Fig. 14.

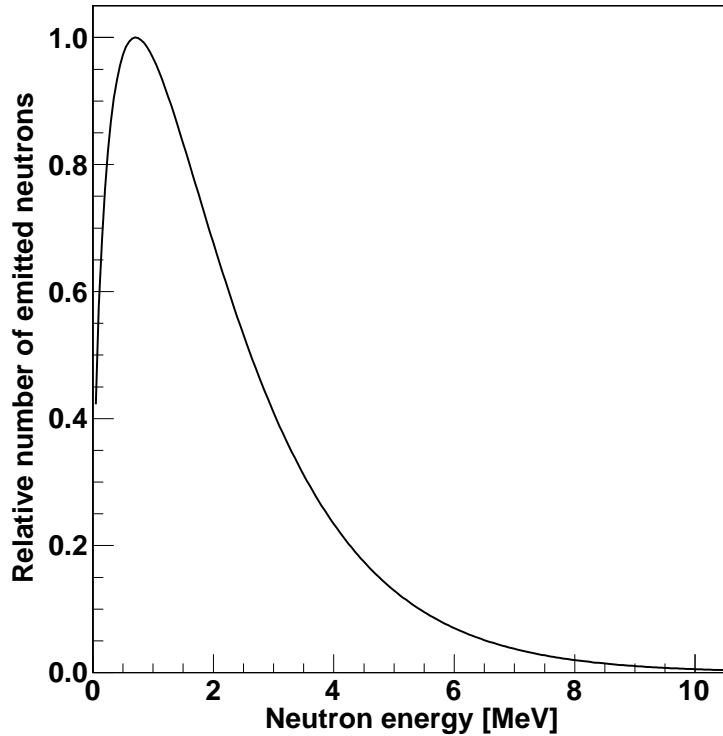


Figure 14: Energy distribution of  $^{252}\text{Cf}$  neutrons according to eq. (1) with  $T = 1.42 \text{ MeV}$ .

The neutron spectra in the fusion-evaporation reaction were simulated with the code LILITA\_N97. The code performs calculations on the basis of the Hauser-Feshbach statistical model. The de-excitation of the compound nucleus is modelled through a multistep emission of light particles (neutrons, protons and  $\alpha$ -particles) adopting the Hauser-Feshbach formulation of the statistical model in conjunction with the Monte Carlo method. The program produces energy spectra and angular distributions in the laboratory frame for light particles and evaporation residues. The code LILITA\_N97 is an extensively modified version of the original LILITA [17] code. It includes several options for transmission coefficients, yrast line, level density and nuclear deformations, some of which are described and discussed in Ref. [19, 20]. Furthermore, for this work a new prescription for the transmission coefficients based on the optical model (OM) was implemented in the code. For the neutrons and protons the global parametrisation of Koning and Delaroche [21] was used. For this parametrisation, the authors fitted the optical model parameters (OMPs) with the available

systematics for elastic scattering of neutrons and protons with nuclei in a wide mass ( $24 < A < 209$ ) and energy ( $0.2 \text{ MeV} < E < 200 \text{ MeV}$ ) range. From this fit they constructed neutron-proton mass-asymmetry dependent global OMPs, which not only improve the description of the observables with respect to all the other existing phenomenological OMPs, but also cover wider mass and energy ranges. These OMPs have been successfully adopted in the systematic work of Ref. [22] to reproduce cross sections measured in neutron and proton induced reactions. Due to the inclusion of the  $N$ - $Z$  dependence, the OMPs are well suited for calculations involving nuclei far from stability.

For the present simulations the fusion-evaporation reaction produced by a  $^{58}\text{Ni}$  beam at 220 MeV impinging on a  $^{56}\text{Fe}$  target with a thickness of  $10 \text{ mg/cm}^2$  was used. The choice of this reaction was motivated by the existence of a comprehensive work [14] used for the characterisation of the Neutron Wall detector array. This reference data set provides a framework for the validation of the simulations. Furthermore, this system is very similar to the ones that will be investigated in the future experiments with NEDA.

A series of simulations were performed to take into account the different energies at which the reaction occurs due to the energy-loss inside the target. In order to reproduce the experimental data, several values were considered for the level density parameter  $a$  were considered, in the range from  $A/12$  to  $A/6$ . The best agreement was obtained with  $a = A/8$ . In addition, the prescription to determine  $a$  as a function of the neutron-proton mass asymmetry, as proposed in [23], was used in the calculation. The effect of the variation of the level density parameter  $a$  on the results is not reported here, because it is negligible on the inclusive neutron energy spectra and angular distributions. The sensitivity to  $a$  is lost due to the convolution of all the decay channels considered. In fact, the effect is smoothed when the evaporation residues approach the valley of  $\beta$  stability. Other observables, like the neutron energy spectra emitted by nuclei far from stability and the cross sections of the evaporation residues are predicted to be more affected [24] and will be studied in a future work.

## 5.2 Geometries

The analysis of possible detector arrangements (geometries) was done with the aid of GEANT4 simulations. Events were generated using both the neutron source model and the fusion-evaporation statistical model code LILITA\_N97.

Only three regular polygons (square, triangle, hexagon) can tile a planar surface without gaps. This can be done by using only one type of these polygons or a combination of several of them. One of the polygons, the regular hexagon, was chosen as the starting point for the NEDA geometry since its area covers the largest fraction of the area of the photocathode of a photomultiplier with a circular cross section. Thus, the NEDA detector unit will have the shape of a uniform hexagonal prism, see Fig. 15. The optimum depth of the detector units, evaluated using GEANT4 simulations, is 20 cm as discussed in Ref. [10], see Sec. 4.1. The side length of the hexagon is 81 mm, selected in order to be suitable for the largest commonly available photomultiplier tubes with 5 inch diameter. The volume of the detector unit is about 3 litres. An aluminum canning with a thickness of 3 mm thickness is used in order to provide a large enough mechanical stability to the detector.

The diversity of experimental conditions expected for NEDA, using both stable and radioactive high intensity beams, require a modularity of the conceptual design. In addition to modularity, four basic conditions have been considered for the design of the array:

1. Efficiency: to be maximised within the geometrical coverage.
2. Target-to-detector distance: necessary for the time-of-flight (TOF) discrimination.
3. Sufficient granularity of the array: required to maximise the detection efficiency for neutron multiplicities larger than one.

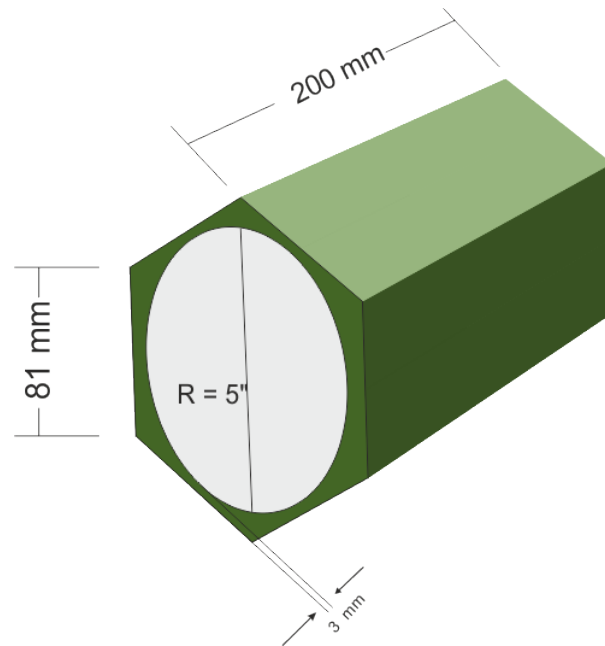


Figure 15: Schematic picture of the NEDA detector unit.

#### 4. Cost: use detectors modules with only one shape.

A larger distance between the target and the detectors provides several advantages. As mentioned, it allows to improve the neutron- $\gamma$  discrimination based on TOF measurements, but also to increase the neutron energy resolution and to reduce the probability of rejecting events in which neutrons were emitted within a small solid angle in reaction channels with neutron multiplicity larger than one.

Taking into account the previous conditions and the detector dimensions already discussed, a few configurations were initially proposed [25]. On the basis of the simulated performance figures, the configuration shown in Fig. 16 was selected for the NEDA array. In this configuration, all detectors are placed at a distance of 1 m from the target. The detectors located between  $\theta = 60^\circ$  and  $\theta = 90^\circ$  were oriented towards the target position to maximise the exposition to the emitted particles. Such a geometry with 331 detector units covers a solid angle of  $1.87\pi$  sr in the forward direction as reported in Table 1. Additionally, a configuration with a spherical surface was created, see Fig. 17. In this configuration, 20 different irregular hexagonal shapes and one type of pentagonal shape were used to form the array. This geometry contains 606 detector units and provides a realistic reference for the simulations with a coverage of a solid angle of almost  $2\pi$  sr. Further properties of this configuration are given in Table 1.

### 5.3 Coupling of NEDA and Neutron Wall

An early implementation of NEDA, together with the Neutron Wall, is proposed for the AGATA campaign at GANIL. The use of the Neutron Wall detectors in combination with NEDA detectors has been proposed considering the fact that the NEDA array is still under production and therefore only a limited number of NEDA detectors will be available. On the other hand, such a combination will provide a higher geometrical efficiency compared to the case when the Neutron Wall is used alone. The two configurations proposed for the combination of NEDA and Neutron Wall are shown in Fig. 18. In the configuration shown in the left hand panel of Fig. 18, the Neutron Wall is placed at its nominal position, i.e. with the front face of the detectors at 510 mm from the target position. The 46 NEDA detector units are placed at the same distance but at larger angles, around  $90^\circ$  with

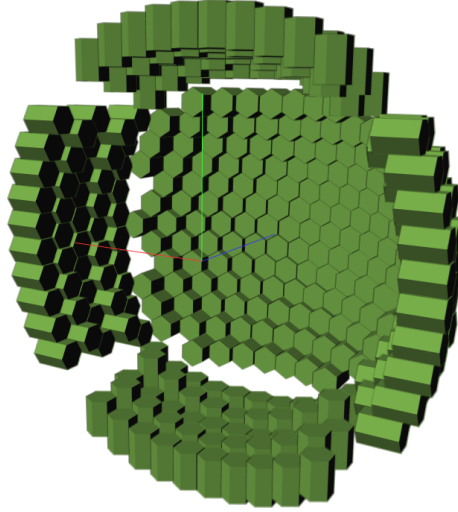


Figure 16: The proposed geometry of NEDA  $2\pi$  consisting of 331 detector units and covering a solid angle of  $1.87\pi$  sr at a distance of 1 m from the target position.

Table 1: Summary of the basic properties of the simulated arrays. In the configuration Neutron Wall + NEDA (b), the Neutron Wall is moved 240 mm downstream along the beam line, which is indicated as 0.75 m in the table.

Configura- tion	Granu- larity	Solid angle [sr]	Average volume/unit [litre]	Total volume [litre]	Distance to target [m]
Spherical $2\pi$	606	$\sim 2\pi$	2.00	1212	1.0
NEDA $2\pi$	331	$1.87\pi$	3.23	1065	1.0
Neutron Wall	50	$\sim 1\pi$	2.92	146	0.51
Neutron Wall + NEDA (a)	96	$1.85\pi$	3.23	294	0.51
Neutron Wall + NEDA (b)	100	$1.32\pi$	3.23	307	0.75, 0.51

respect to the beam direction. In the configuration shown in the right hand panel of Fig. 18, the Neutron Wall is moved 240 mm downstream from the target. This allows for inserting 50 NEDA detector units at 510 mm and at angles somewhat smaller than  $90^\circ$ , in order to have a larger granularity in the forward direction. Configuration (a) allows to cover a larger solid angle with a smaller number of NEDA detectors, while (b) has a slightly larger granularity in the forward angles. Further geometrical properties of the configurations are given in Table 1.

In the following sections the simulations performed to determine the neutron efficiency for the cases of isotropic emission from a neutron source and for a fusion-evaporation reaction are presented and discussed.

## 5.4 Neutron Wall Simulations

In Ref. [16] a series of Neutron Wall simulations were also performed, motivated by the first implementation of NEDA at GANIL, in which NEDA will be coupled to the Neutron Wall as already discussed in section 5.3. A set of the existing  $^{58}\text{Ni} + ^{56}\text{Fe}$  in-beam data, taken with the Neutron Wall, was used to validate the event generator. Simulations were performed for NEDA to get the evaluated performances of the array when a realistic fusion-evaporation reaction is considered.



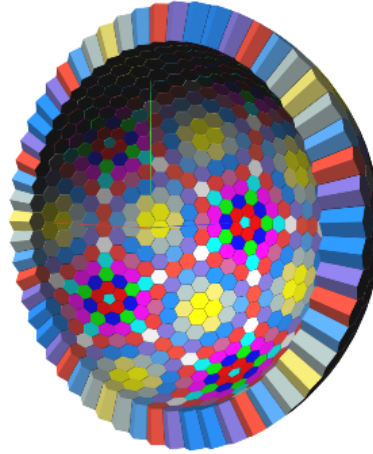


Figure 17: This spherical configuration was designed as a realistic reference. It consists of 606 detector units with 21 different shapes, covers a solid angle of almost  $2\pi$  sr at a distance of 1 m from the target position.

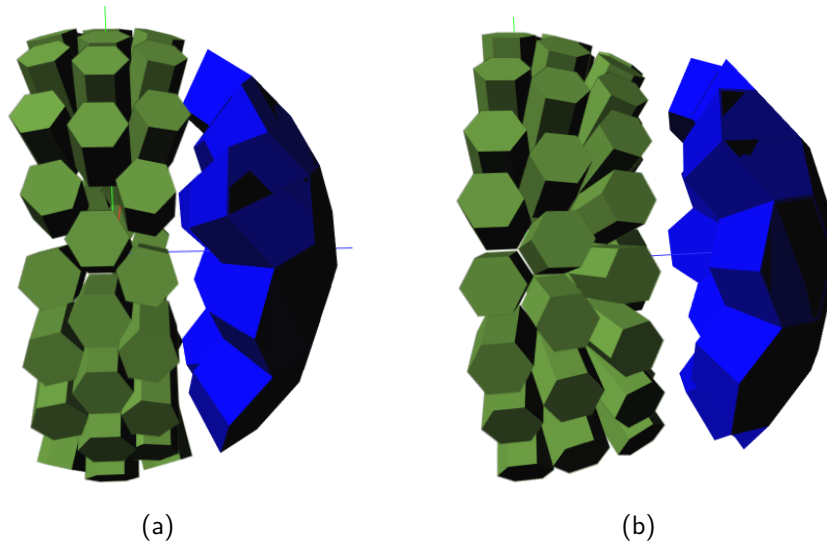


Figure 18: The proposed geometries of the coupling of a) 46 and b) 50 NEDA detectors (green, left-hand-side) and 50 Neutron Wall detectors (blue, right-hand-side) for the AGATA campaign at GANIL.

The summary of the results of the Neutron Wall simulations showed that the simulations are in a very good agreement with the experiment concerning neutron energy and angular distributions. The best agreement was obtained when the material between the target and the Neutron Wall detectors (mainly beam pipe and beam dump) were included in the simulations and the center-of-mass-energy of the neutrons in LILITA\_N97 were increased by 800 keV. The reason for the necessity of increasing the neutron energies is not fully understood. See Ref. [16] for further details.

## 5.5 Neutron Efficiencies and Crosstalk Reduction

In a neutron detector array with a compact geometry, such as NEDA, the probability of neutron scattering is rather large. This leads to an ambiguity regarding the actual number of neutrons emitted versus the number of neutrons measured. In order to decrease this ambiguity and to optimise the

two- and three-neutron efficiency, a method based on the distance between the centroid positions ( $\Delta r$ ) and the difference in TOF ( $\Delta t$ ) of each pair of detectors in the array that registered a neutron interaction in the event, is commonly used [26, 14]. Each pair of coincident neutron signals is investigated to determine its physical origin. If the TOF difference  $\Delta t$  is large enough to cover the distance  $\Delta r$ , assuming a realistic range for the neutron energy, the two signals are assigned to be due to crosstalk, i.e. a single neutron was emitted. Otherwise, they are assigned to be real two neutron events. This procedure can be extended to all possible combinations of two pairs of detectors that fired in each event.

Fig. 19 shows the distribution of  $\Delta r$  versus  $\Delta t$  for simulated single neutron events using the  $^{252}\text{Cf}$  source. By definition, all these data points are associated to crosstalk events and the observed distribution in  $\Delta t$  is due to the differences in the neutron velocities. The area within the triangle corresponds to  $\Delta r$ - $\Delta t$  events that are due to real two neutron events. The diagonal line represents the largest neutron velocity for which a crosstalk event is defined and therefore for a given neutron energy spectrum this diagonal line is independent of the geometry. A few events can be observed inside the triangular gate. Those are neutrons with velocities larger than the velocity corresponding to the diagonal line of the triangular gate. Note that according to eq. (1), the neutron energies can be infinitely large. The number of events for this parametrisation of the neutron energy of the  $^{252}\text{Cf}$  source is about 0.9 %.

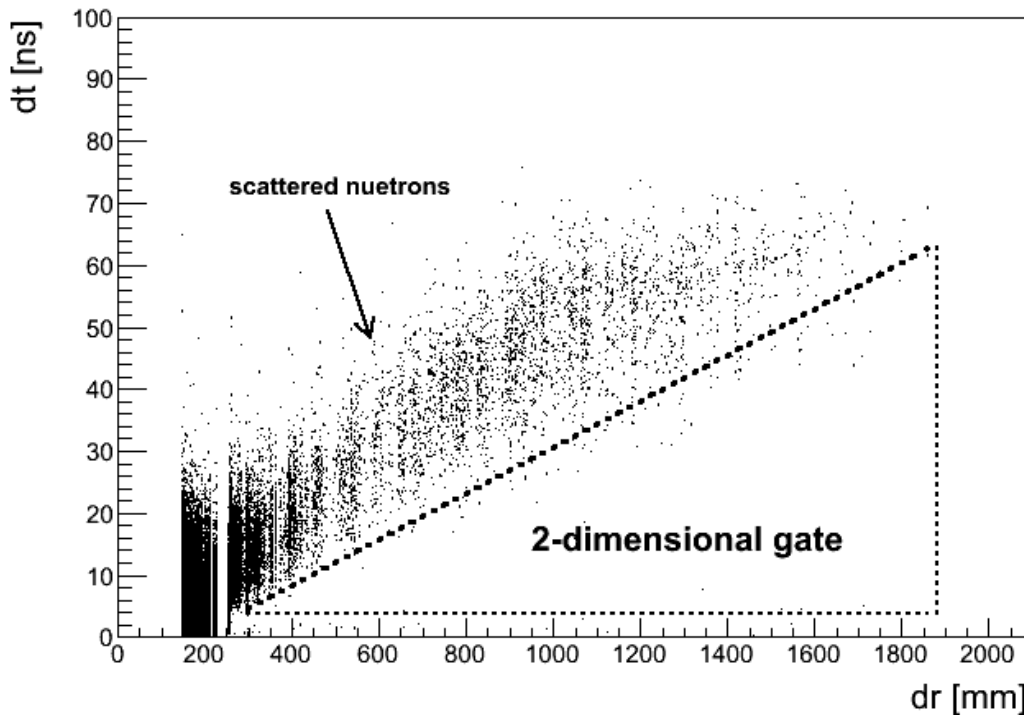


Figure 19: A plot of  $\Delta r$ - $\Delta t$  for simulated one neutron events from the  $^{252}\text{Cf}$  source. The diagonal line represents the largest neutron velocity for which a crosstalk event is defined. The two dimensional triangular gate corresponds to the area where real two- and three-neutron events would be located.

Tables 2 and 3 show the results for neutrons emitted from a  $^{252}\text{Cf}$  source and from the fusion-evaporation reaction  $^{58}\text{Ni} + ^{56}\text{Fe}$ , respectively. The efficiency values given in these tables were reduced by a factor of 0.789 per detected neutron to take into account the loss in efficiency due to the NGD (see Ref. [16] for details).

According to the results of the simulations, the NEDA  $2\pi$  geometry will provide a substantial improvement in terms of efficiency performances. The two-neutron efficiency for fusion-evaporation

Table 2: One-, two- and three-neutron efficiencies obtained from simulations of a  $^{252}\text{Cf}$  source for the different detector configurations.

Geometry	$\varepsilon_{1n}$ [%]	$\varepsilon_{2n}$ [%]	$\varepsilon_{3n}$ [%]
Spherical $2\pi$	20.29	2.16	0.51
NEDA $2\pi$	17.70	1.76	0.35
Neutron Wall	8.41	0.51	0.06
Neutron Wall + NEDA (a)	15.90	1.40	0.21
Neutron Wall + NEDA (b)	12.92	0.88	0.10

Table 3: One-, two- and three-neutron efficiencies obtained from simulations of a fusion-evaporation reaction  $^{58}\text{Ni} + ^{56}\text{Fe}$  at 220 MeV for the different detector configurations.

Geometry	$\varepsilon_{1n}$ [%]	$\varepsilon_{2n}$ [%]	$\varepsilon_{3n}$ [%]
Spherical $2\pi$	43.66	8.62	3.46
NEDA $2\pi$	35.94	6.04	1.75
Neutron Wall	25.99	0.85	0.19
Neutron Wall + NEDA (a)	31.85	2.48	0.34
Neutron Wall + NEDA (b)	26.42	2.38	0.33

reactions is predicted to be about 7.1 larger than what is obtained for the Neutron Wall. There is also a noticeable improvement of the three neutron efficiency, which is predicted to be a factor of almost 10 higher than the value obtained for the Neutron Wall. The spherical  $2\pi$  geometry naturally gives the largest efficiencies. However, the NEDA  $2\pi$  geometry has definitive mechanical and cost benefits. The two configurations shown in Fig. 18a and 18b, for the early implementation of NEDA for the AGATA campaign at GANIL, show similar performances. The two neutron and three neutron detection efficiencies for these two configurations are larger than what is obtained for the Neutron Wall in standalone mode by a factor of about 3 and 1.5, respectively. Configuration (a) has a smaller number of detectors and is therefore the preferred one.

## 6 Front-End Electronics

This section contains a description of the design and tests of the NEDA front-end electronics. Further details can be found in Refs. [27, 28, 29].

### 6.1 Electronics Layout

NEDA electronics design is going to be conducted in three phases. Firstly, the new digital electronics is envisaged to instrument the Neutron Wall array [30, 14] consisting of 50 detectors. Secondly, 48 NEDA scintillator detector modules plus electronics will be produced and used in the AGATA campaign at GANIL in 2016-2017 and for the NEDA@HISPEC experiments at NUSTAR/FAIR from 2018. Finally, the electronics for the full NEDA array, with 331 detectors, will be built in the last phase.

The electronic chain is made of the following parts: front-end single-ended to differential converters, sampling mezzanines and NUMEXO2 pre-processing, LINCO2 PCIe interface, Global Trigger and Synchronisation (GTS) system, and finally data acquisition nodes (workstations).

Each single detector module is readout by one single front-end electronics channel whenever a current signal is provided from the anode output of the corresponding PMT. The anode signals are connected to the front-end connection panel, performing the conversion to differential before sending the signal through a 10 m long cable to the NUMEXO2 digitiser. Each conversion board has 8 channels. Once the signal reaches the NUMEXO2 digitiser, the pulse is sampled continuously by the FADC mezzanines [27] at 200 MS/s with a resolution of 14 bits. The FADC mezzanines are part of the NUMEXO2 digitiser, with each mezzanine board being plugged into the motherboard. As the signal is digitised, it passes by a set of programmable devices based on the FPGA (field-programmable gate array): a Virtex-6 and a Virtex-5. Firstly, a trigger algorithm is applied in the Virtex-6 so that the amount of events produced by  $\gamma$  rays gets drastically reduced, hence optimising the readout bandwidth capabilities. At the Virtex-5 trigger requests, produced mostly by neutrons, are received and sent to the GTS (Global Trigger System) in order to receive a validation or rejection. A timestamp is as well attached to the event buffer. Additionally inside the Virtex-5, an embedded processor containing an embedded Linux OS runs the slow-control tasks of the whole digitiser and the communication ports. Each NUMEXO2 digitiser has the capability to deal with 16 channels and contains one optical connection to the GTS.

In Fig. 20, the global electronics layout is depicted for a total amount of 48 detectors, requiring 3 NUMEXO2 NIM boards. The local GTS in the NUMEXO2 card is optically connected to the GTS tree, which is located in another NIM module in another NIM crate. The connection procedure is detailed in the GTS section 6.7.

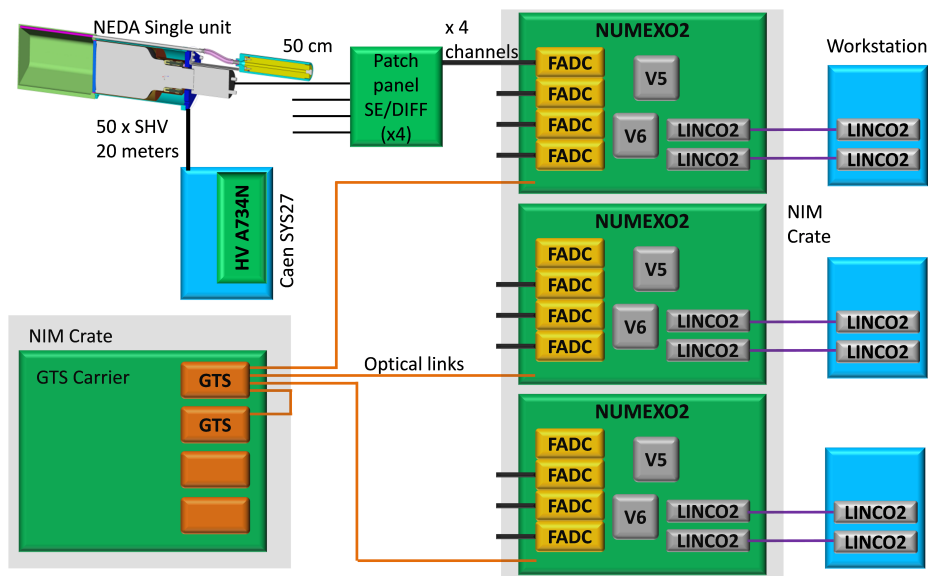


Figure 20: Global electronics layout for 48 NEDA detectors

For 48 NEDA detectors the following is required: 3 NUMEXO2 boards, 12 mezzanines, 6 single-ended to differential boards, 1 GTS NIM motherboard containing 2 GTS V3 mezzanines and two NIM crates. The final NEDA design, consisting of 331 detector units, requires 21 NUMEXO2 boards, 83 FADC mezzanines, 42 single-ended to differential modules, 3 GTS NIM motherboards containing 11 GTS V3 mezzanines and 3 NIM crates. Each of the following sections is aimed to describe in details the aforementioned blocks starting from the front-end single-ended to differential board and finishing by the LINCO PCIe boards.

## 6.2 Single-Ended to Differential Board

Given that fast pulses, with less than 10 ns rise time, must be transmitted to the NUMEXO2 digitiser, placed 10 m away from the detector in a noisy environment, it was preferred to drive the signals in a differential mode, increasing the noise immunity. The first electronic stage is a small box placed close to the PMT of the scintillators. Its role in the processing is to convert the incoming PMT signals to differential mode before being transmitted over the HDMI cable. Fig. 21 shows the block diagram of the front-end electronics board.

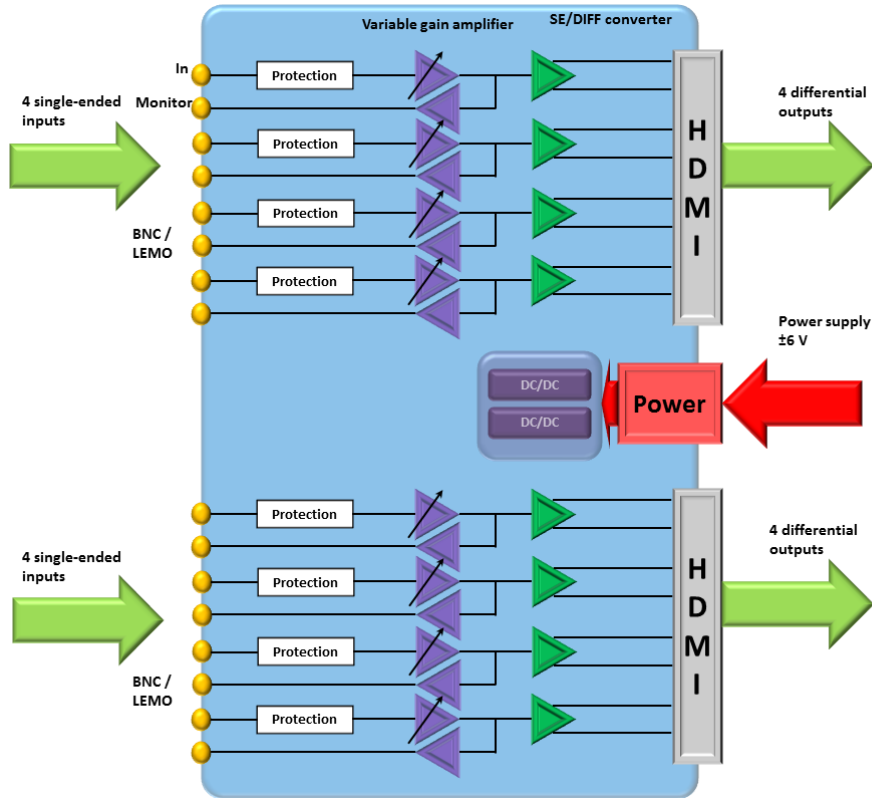


Figure 21: Front-end electronics board.

The design contemplates the following functionalities:

- 8-channel single-ended to differential low-noise stages.
- Protection system against high-voltage peaks, avoiding damage on the front-end and back-end electronics.
- A monitor output set before the conversion to differential to display a signal.
- Capability to adjust the gain.

Regarding the design of the single-ended to differential channel, the topology combines both fully-differential amplifiers using the AD8139 for the conversion to differential, and low-noise operational amplifiers AD4817-1 to provide an easier gain control. To optimise the noise performance on the conversion to differential, a unitary-gain operation mode is selected for the AD8139, while the ADA4817-1 precedes the AD8139 implementing a follower circuit with a potentiometer at the non-inverting input, allowing to control the signal gain. The schematic is presented in Fig. 22.

The part preceding the buffer is composed of an over-voltage protection circuit, a smoothing capacitor  $C_s$ , in case a shaping of the signal is needed (not mounted in the present version) and a terminator in split configuration. The protection circuit is based on low-capacitance ( $< 1.5$  pF) fast-switching Shottky diodes from the BAV99 series, driving overvoltage peaks towards the power

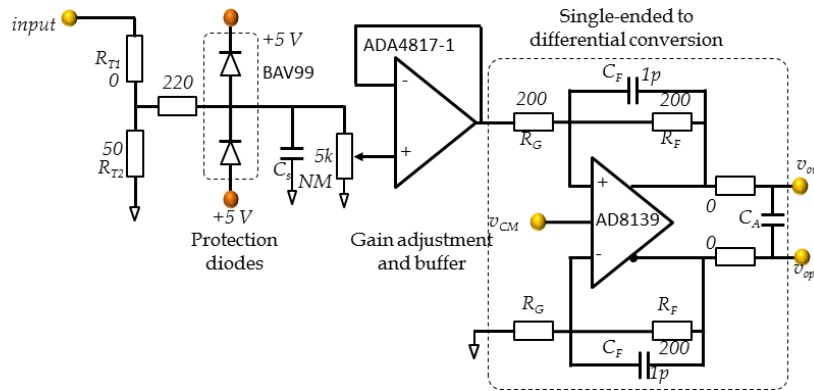


Figure 22: Front-end electronic channel schematics.

supply, 5 Vdc in the current design, with the current being limited by the 220  $\Omega$  resistor. The input terminators  $R_{T1}$  and  $R_{T2}$  may be configured either for current or voltage inputs. In case of a current input (from a PMT) the current input is transformed into voltage with the input voltage divider point. On the other hand, for standard voltage inputs from a signal generator,  $R_{T1}$  is set to 0  $\Omega$  and  $R_{T2}$  to its corresponding termination impedance, typically 50  $\Omega$ .

### 6.3 Cable Transmission Features

Due to the fast nature features of the signals, a test bench has been developed to characterise a set of different cables and determining the best solution for NEDA, by applying bandwidth (BW), crosstalk and EMI tests. The candidates for connection to the front-end are:

- MDSM coaxial cable, containing 19 coaxial connections.
- HDMI cable.
- HDMI v1.4. Infinite.
- PoCL-Lite camera cable.

The procedure to measure the bandwidth consists of driving sinusoidal input signals with constant amplitude across a frequency sweep, measuring the amplitude degradation at the output versus the frequency. The bandwidth is then calculated as the frequency at which the output to input voltage ratios are 3 dB below the value at low frequency. The results for all cables are shown in Table 4.

Table 4: Cable bandwidths.

Cable under test	-3 dB point (BW)	-6 dB point
MDSM	-	-
HDMI	70 MHz	230 MHz
HDMI v1.4 Infinite	120 MHz	> 240 MHz
PoCL-Lite	35 MHz	130 MHz

Crosstalk tests are performed by driving on one of the pairs a differential pulse and measuring the induced voltage on a second victim pair at the far-end. Specially, it is interesting to study the effect for different signal rise times. The measurements have been carried out at 10 ns and 2.5 ns, even though the latter is out of the specifications, and therefore aimed mostly at measuring the cable robustness against coupling. The waveforms used for these tests consists of square waveforms of

1 Vpp. It is important to terminate the unused pairs in order to avoid reflections from the victim pairs. The crosstalk measurements are summarised in Table 5 for signals with rise times 10 ns and 2.5 ns. The values given are the differential crosstalk (not the induced crosstalk on each conductor of the pair).

Table 5: Crosstalk test comparison for different cables at different rise / falling times.

Cable	$t_r = 10 \text{ ns}$	$t_r = 2.5 \text{ ns}$
MDSM	14 mV	43.8 mV
HDMI	2.73 mV	3.82 mV
HDMI v1.4 Infinite	3.94 mV	8.02 mV
PoCL-Lite	3.16 mV	4.18 mV

Since the experimental area will contain processes that involve radiation, it is of major interest to test the shielding and grounding robustness against high-voltage peaks susceptible to be induced into the cable. EMI measurements can be implemented by applying high-voltage pulses induced to the cable using a conductive surface such as a piece of foil paper embracing part of outer surface of the cable. As for the crosstalk measurements, it is required to terminate correctly each unused pair, preventing the cable from undesired reflections that could falsify the measurements. A high-voltage pulse generator NSG1025 from Schaffer was used to inject 1 kV high-voltage pulses of 1  $\mu\text{s}$  width and with a frequency of 50 Hz. Besides, a copper plate was used to ground the whole testbench by grounding the equipment chassis. The EMI results for the tested cables are summarised in Table 6.

Table 6: EMI results for different cables.

Cable under test	Peak-to-peak of the induced voltage
	for a 1 kV voltage peak
HDMI v1.4 Infinite	356 mV
HDMI	1.077 V
PoCL-Lite	6.252 V

In conclusion, according to all the results obtained, the best cable choice is the HDMI v1.4 Infinite cable, since is the only one capable to deal with the NEDA signals by having a bandwidth of 120 MHz. In addition to the bandwidth results, HDMI v1.4 Infinite shows the best performance regarding crosstalk, EMI measurements, thus being finally the most suitable option for NEDA.

## 6.4 NUMEXO2 Front-End Electronics Hardware

NUMEXO2 is the core of the NEDA front-end electronics. The NUMEXO2 digitiser and pre-processing system has been designed in synergy with GANIL, providing a common solution for more detection systems, reducing time and resources. The digitiser functionalities can be summarised as follows: A/D conversion, data pre-processing, connection to the GTS system and communication links management for 16 channels. The system is composed of a motherboard and a set of 4 FADC mezzanines, which perform the A/D conversion for 4 channels each. NUMEXO2 owes its flexibility due to the use of FPGAs, facilitating the firmware algorithm design. Particularly, NUMEXO2 comprises 2 high-performance FPGAs, a Virtex-6 and a Virtex-5 from Xilinx. Fig. 23 illustrates the main NUMEXO2 block diagram, including the FPGAs, FADC mezzanine and communication links.

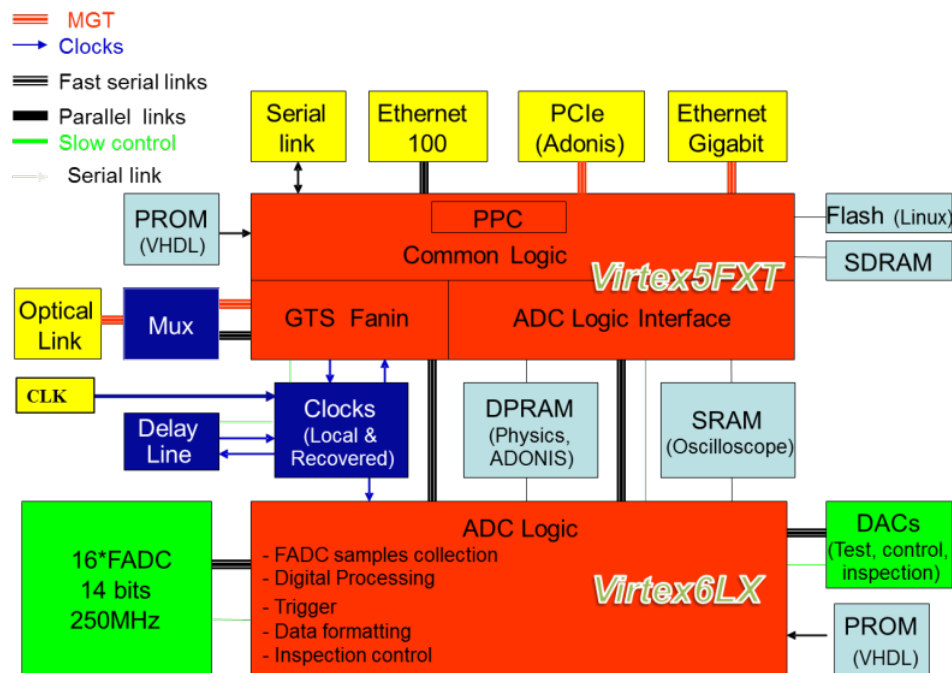


Figure 23: NUMEXO2 general block diagram.

### 6.4.1 Power Management

NUMEXO2 is design to be located in a NIM crate from Caen capable of delivering up to 2000 W, from which the power supply is delivered to the rest of the electronics within the digitiser, including the FADC mezzanines. For this specific crate, the voltages and currents provided are:  $\pm 6\text{ V}$  (90 A),  $\pm 12\text{ V}$  (20 A) and  $\pm 24\text{ V}$  (10 A). This allows for a maximum of 130 W per NUMEXO2 unit when hosting 12 digitisers in the crate. The usage of FPGAs normally involves a big assortment of different voltages to supply all blocks correctly. Fig. 24 shows the power supply block diagram.

In practice, the average total power consumption per digitiser, running at 200 MS/s and with both FPGAs running the firmware is not expected to be higher than 100 W.

### 6.4.2 NUMEXO2 Interface

NUMEXO2 is interfaced outwards by connections both at the front and rear panels. Also, internally QFS connectors are provided for communication with the FADC mezzanines.

Connections on the front panel:

- The data is driven differentially from the front-end modules using four HDMI (19 pins) cables. 12 of the pins are used as inputs while the rest remain grounded. Additionally, a screwing tool strengthens the connection against mechanical vibrations.
- Two HDR PoCL-Lite connectors. Used to deliver the power supply to the front-end electronics.
- Four double LEMO 00 connectors to drive 4 inspection lines from signals capable to be visualised. Each inspection line can be daisy-chained to another digitiser, requiring 2 connectors per inspection line. From the 4 inspection lines, 2 are digital and 2 are analog.
- Four LEMO connectors with the following functionalities: external clock, external acquisition stop, external trigger and output clock.

Connections on the rear panel:



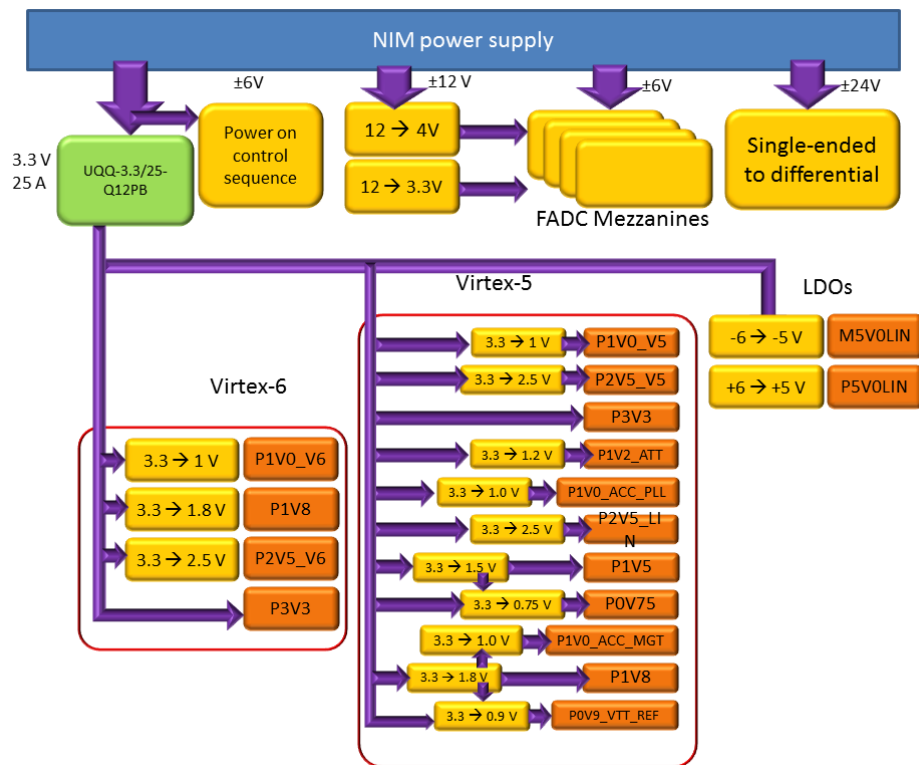


Figure 24: NUMEXO2 power supply distribution.

- One RJ-45 connector used for the TCP/IP readout protocol.
- One RJ-45 connector used to monitor the embedded software booting process using an RS-232 embedded protocol.
- Two LEMO connectors for hard reset and power off.
- An SFP optical connector to link the GTS leaf in Virtex-5 to the V3 mezzanines inside the GTS crate.
- An SFP optical transceiver for the PCIe data transmission. The connector is provided with 4 bidirectional channels.
- An SFP connector to provide the clock the LINCO2 boards.

Internal board-to-board connectors:

- Each FADC mezzanine is interfaced to NUMEXO2 using two QFS-026-04.25-L-D-PC4 connectors from which the power supply, data, clocks and slow control is provided. Eight connectors are required per digitiser to communicate properly with all the mezzanines.

### 6.4.3 Clock Management

The 100 MHz frequency reference of the analog to digital conversion and processing units is delivered by three different sources: The 100 MHz clock of the local oscillator, the 100 MHz remote clock of an external generator and a 100 MHz clock recovered from the GTS system. The choice of the 100 MHz source is controlled by software. By default, the 100 MHz reference clock is sourced by the local oscillator.

The block diagram in Fig. 25 shows two parts:

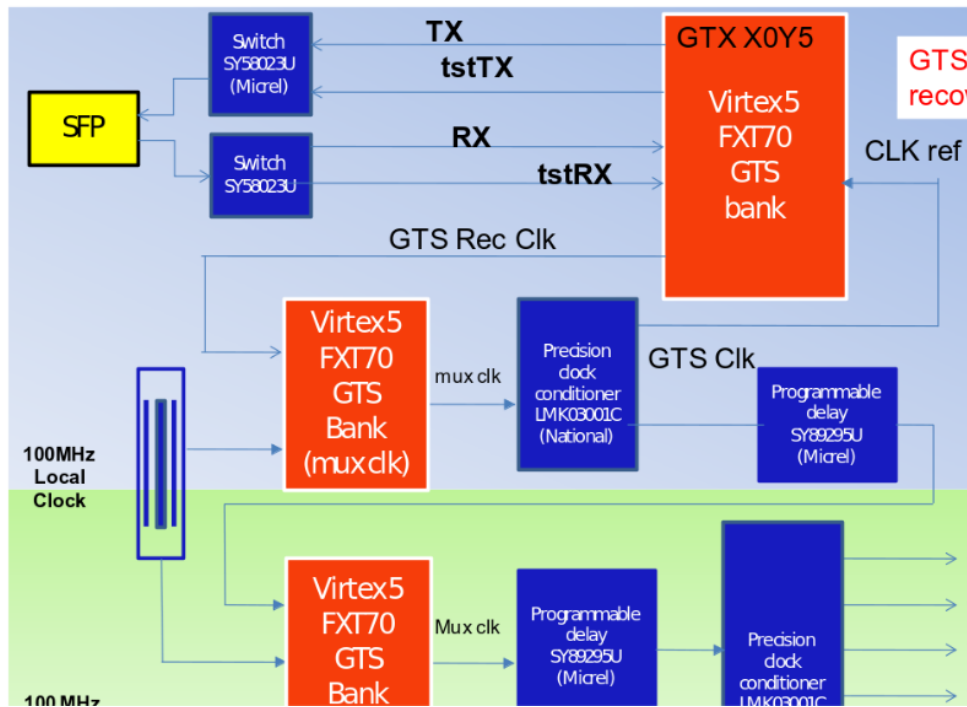


Figure 25: NUMEXO2 clock management block diagram.

- GTS clock: the 100 MHz clock is recovered from the optical communication with the GTS system. Once the GTS is locked by the PLL, the 100 MHz GTS clock is sent to a multiplexer. The delay line aims to tune the fine coarse alignment of the clock phase regarding the timing of the messages recovered from GTS communication.
- 100 MHz clock selection: the selected clock is sent to a delay line and to a PLL aiming to tune the phase and to distribute the 100 MHz to FPGAs and FADC mezzanines.

#### 6.4.4 Readout Requirements

Fig. 26 shows the different requirements in terms of data throughput at several points inside NUMEXO2.

Taking into account that the experimental conditions are expected to work maximally at a counting rate of 50 kHz, the FADC mezzanine maximum sampling frequency at 250 MHz (in practice 200 MHz will be used), and the 14 bit resolution (stored in 2 bytes), the throughputs and data rates can be derived as follows. Assuming that the length of the data packet to send between both FPGAs is 250 samples, and the counting rate is 50 kHz/channel, it can be calculated that the average amount of data per channel is  $50 \text{ kHz} \times 250 \text{ samples} \times 2 \text{ bytes}$ , which gives 25 MB/s/channel. The fast link between the V6 and V5 contains 8 lanes to drive the data retrieved from 2 channels, which increases the total amount of data per lane to 50 MB/s (400 MB/s for all channels). Therefore, taking into account the 4 lanes provided by the PCIe readout in terms of bits/second, one obtains 3.2 Gbps in total and 800 Mbps per PCIe lane. The maximum data rate of PCIe is 10 Gbps, verifying the protocol suitability for this application.

#### 6.5 Sampling FADC mezzanine

Fig. 27 shows the FADC mezzanine block diagram. The digitiser chosen for this application is the dual FADC ADS62P49, with 14 bits and 250 MS/s. Considering the jitter and noise specifications

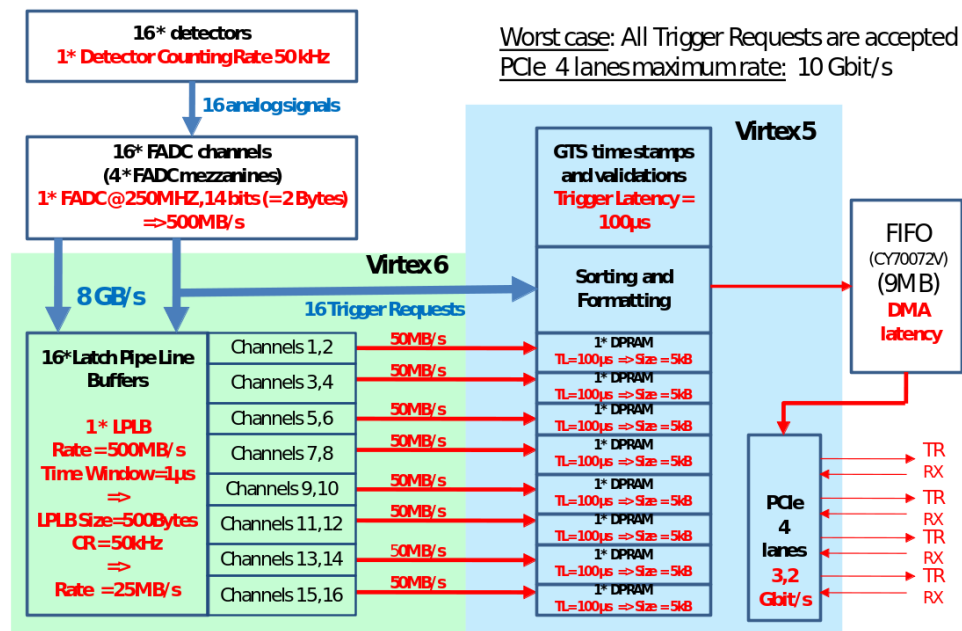


Figure 26: NEDA readout requirements block diagram.

of the FADC, the rest of the devices, such as jitter cleaner, analog coupling stages, DACs, power regulators and connectors, have been selected.

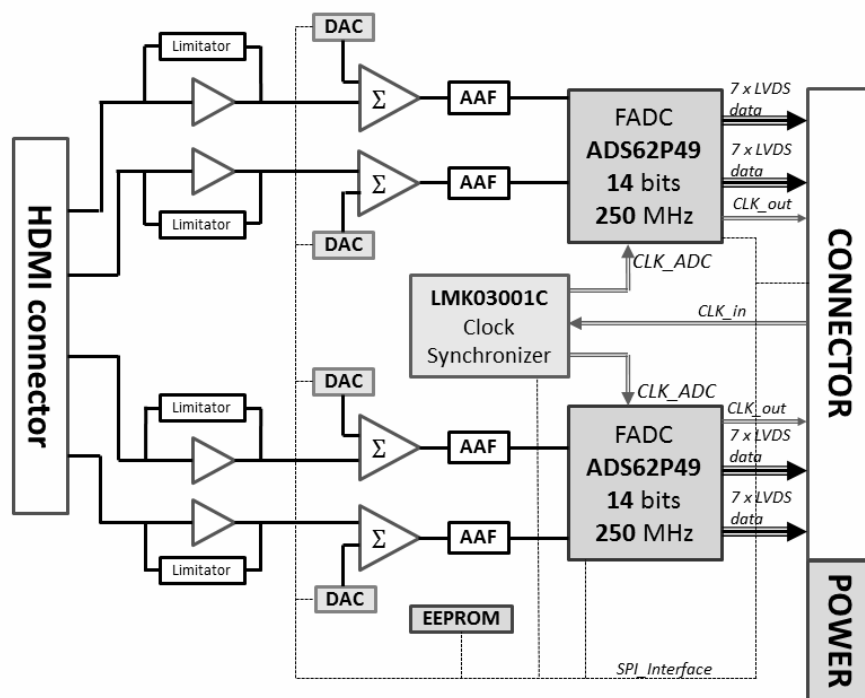


Figure 27: FADC mezzanine block diagram, including the most important blocks, such as the FADC device, PLL, DACs, operational amplifiers and connectors.

The analog input stage coupled with the FADC is the most critical in terms of noise. Additionally, extra offsets are added in order to take full profit of the FADC dynamic range, allowing the acquisition of both unipolar and bipolar signals. After a careful study, the coupling is performed by means of AD8139 fully-differential amplifiers (FDA). At this stage, also the gain control is carried out to select

a range of either 6 MeV or 20 MeV.

The aforementioned energy ranges can be translated at the level of the mezzanine as voltage-to-voltage gains, which are, 1 and 0.25 respectively. Due to stability facts, the amplifier must work minimally under unitary gains, as lower gains make it unstable. Moreover, the noise performance conditions are optimal for unitary gain, worsening for higher gains. Due to the noise constraints and stability issues, the design strategy consisted of using two AD8139-based stages working under unitary gain. The attenuation factor of 0.25 can be then achieved by adding a T-divider in between both stages so that the division ratio and the impedance seen backwards from the amplifier can be designed independently. Based on the schema in Fig. 28, the high-speed analog driver can be designed by applying the following expressions:

$$\text{Gain} = \frac{R_{F2}}{R_{G2}} \frac{1}{R_1} \left( \frac{1}{\frac{1}{R_1} + \frac{1}{R_2} + \frac{1}{R_{G2}}} \right) \quad (2)$$

$$R_{F2} = R_{G2} + R_1 \parallel R_2 \quad (3)$$

$$R_T \parallel R_{G1} = 50 \Omega \quad (4)$$

where  $R_{Fi}$ ,  $R_{Gi}$  refer to the feedback and input resistors of each  $i$ -th analog AD8139 stage respectively,  $R_1$  and  $R_2$  are the T-divider resistors, and  $R_T$  is the input terminator. Equation (3) must be applied in order to make the AD8139 work as a unitary-gain amplifier while eq. (2) is obtained after applying Kirchhoff's laws to the T-divider and second stage input nodes. Finally, eq. (4) is used to match the terminator impedance with the cable impedance provided that the cable has a differential impedance of  $100 \Omega$ .

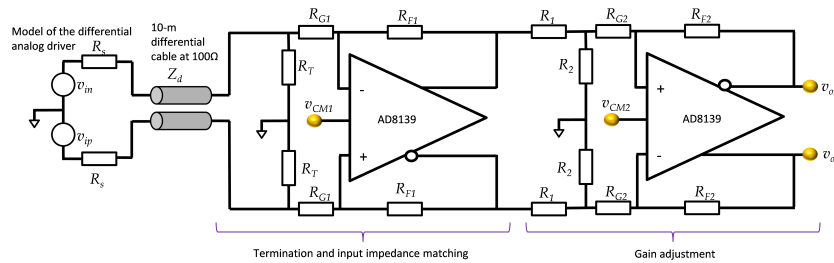


Figure 28: FADC mezzanine block diagram, including the most important blocks, such as the FADC device, PLL, DACs, operational amplifiers and connectors.

A lower-speed analog driver consists of driving the offset voltages from the DAC towards the high-speed analog stage using a side summing branch. Finally, the analog stage contains an anti-aliasing filter set before the FADC device. It is based on a single-pole RC filter with 100 MHz cut-off frequency.

Another important point is the connection to the mezzanine from the front-end electronics. Several quality tests of different cables, such as bandwidth, crosstalk and EMI, were performed. The HDMI v1.4 Infinite was finally chosen as the best solution, see section 6.3. The other interface is connected using a two board-to-board connector to NUMEXO2, connecting slow-control signals, high-speed data, clocks and power nets.

The power supply design must take into account that FADC mezzanine requires several voltages for both analog, mixed and digital devices. The main devices such as the FADC and PLL are supplied

independently by their own LDOs. This strategy was followed not only by power consumption and temperature reasons, but also in order to isolate the noise produced by the clock lines into the A/D converters.

A testbench platform was developed to test the FADC mezzanine performance, involving on one hand standard A/D conversion parameters such as SINAD, ENOB, THD and, on the other hand parameters linked to the quality of acquisition in the field of nuclear physics, such as the energy resolution and neutron- $\gamma$  discrimination performance. The mezzanine was tested using a ML605 Evaluation Module (which contains a Virtex-6 FPGA), to buffer, read out the data and program the FADC mezzanine via SPI. A second additional board, foreseen as a prototype for the NEDA front-end electronics, connects the laboratory equipment to the FADC mezzanine. The software part is performed using a GUI made in LabView to allow the user to communicate with the firmware and with the mezzanine via a serial port. Hence, the user is able not only to visualise and handle the mezzanine registers, but also to watch the data analysis process on-line.

The following describes the parameters that characterise the acquisition system, including measurements of interest for the nuclear physics field. The noise performance of the electronics can be calculated from waveforms containing only the baseline using the expression [31]

$$\sigma_e = \frac{R}{\sqrt{12} \cdot 2^{\text{ENOB}}} \quad (5)$$

Here  $\sigma_e$  is the noise standard deviation in ADC counts obtained experimentally, and  $R$  is the dynamic range, also in ADC counts ( $R = 16384$  for a 14 bit ADC). The measurements have been applied as a function of the ADC range since the resolution varies with the input voltage applied. Fig. 29 summarises the results obtained at 200 MHz for all channels.

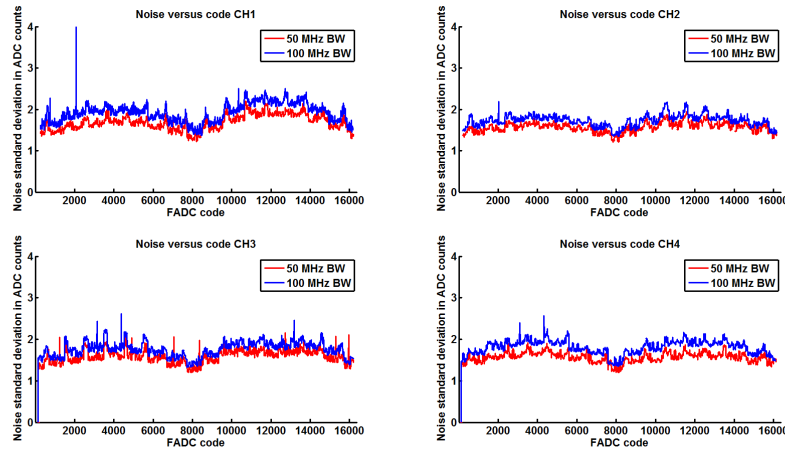


Figure 29: Baseline resolution results in ADC counts. Results have been obtained for all channels at 200 MS/s and for two bandwidths, 50 MHz (red) and 100 MHz (blue)

The figure reveals that for the baseline levels, which are the extreme and middle values,  $\sigma_e$  is about 1.4 and increasing to about 2 for some specific cases, verifying the correct behaviour of the system. Eq. (5) gives  $\text{ENOB} = 11.7$  with  $\sigma_e = 1.4$ .

Energy resolution measurements were performed at GANIL in February 2014 with  $^{60}\text{Co}$  and  $^{152}\text{Eu}$  sources and an HPGe detector. The energy spectra, were measured using the firmware prepared for NUMEXO2 in EXOGAM2 containing a MWD (Moving Window Deconvolution) algorithm and the NARVAL data acquisition system [32, 33]. The results of the spectra are shown in Fig. 30. The measured energy resolution of the 1332 keV peak was  $\text{FWHM} = 2.3$  keV.

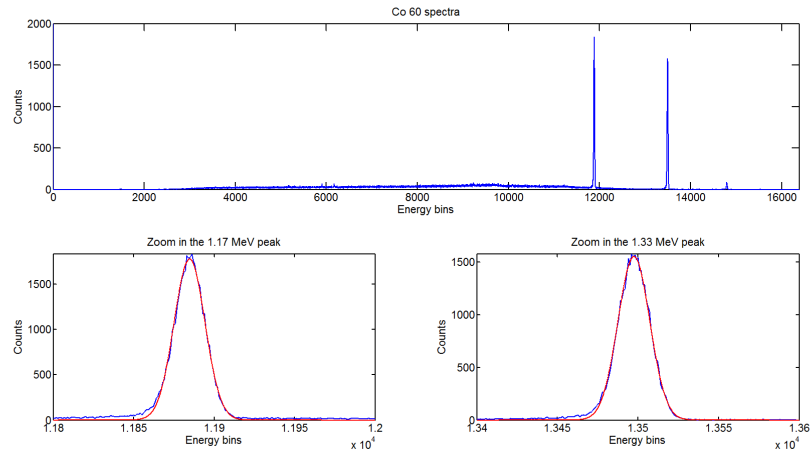


Figure 30: Above: a  $^{60}\text{Co}$  spectrum measured with a HPGe detector and the NUMEXO2. Below: a zoom around the 1173 keV and 1332 keV peaks.

## 6.6 LINCO2 Readout Board

The LINCO2 boards are a set of adapter boards to translate the PCI express signals to/from the optical physical layer to legacy bus standards such as PCI, cPCI, VME, etc. Fig. 31 shows a picture of the LINCO2 board.

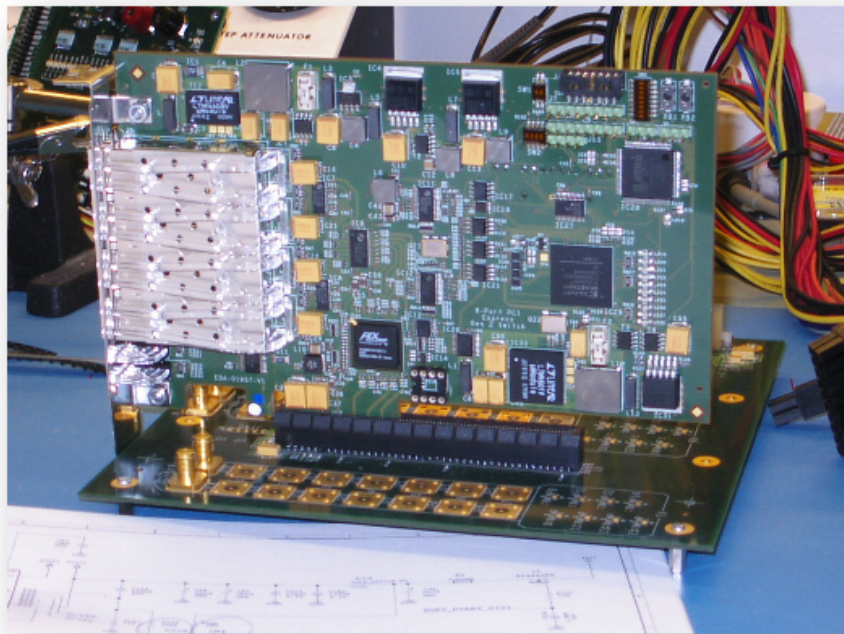


Figure 31: LINCO2 board.

LINCO2 boards have already been used for AGATA and for CMS at CERN in harsh environmental conditions. Each LINCO2 board contains 4 SFP optical connectors, a set of high-speed multiplexers, which allow for a selection of either clock or data signals, and a PLX high-speed switch PEX 8609 capable of working up to 20 Gbps for the interface between the optical fibers and the PCIe finger. A Spartan-3A device is used to configure the high-speed blocks providing 3 different configurations:



1) capability to transmit 4 clocks, 2) 4 data lanes or 3) 2 clocks and 2 data lanes. In Fig. 32, a block diagram of the LINCO2 board is shown.

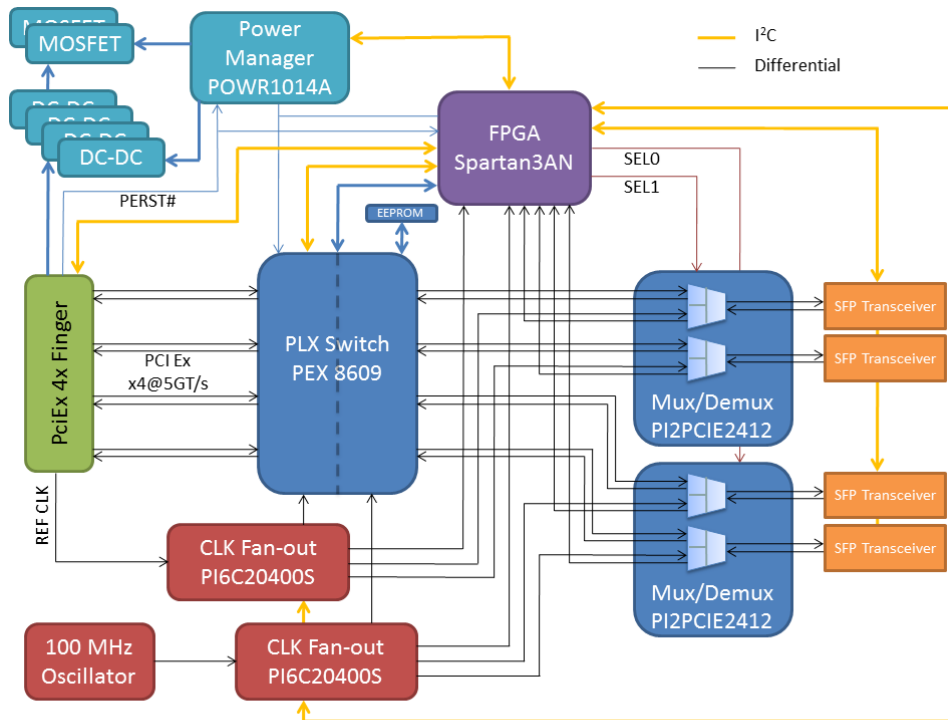


Figure 32: LINCO2 board block diagram.

## 6.7 Global Trigger and Synchronisation System

An upgrade towards a full digital system requires the implementation of a system capable of synchronising all channels and to cope with event validation/rejection. Inherited from AGATA, and being implemented for the NEDA electronics, this is explicitly the task that the GTS performs. One of the most interesting features it provides is the possibility to use it with different detectors, making it possible to have different combinations of detector couplings.

GTS is based on a tree topology (see Fig. 33) containing three different types of firmware depending on the hierarchical solution: GTS leafs, GTS fan-in/fan-out and GTS root. The GTS leafs are located at the bottom of the tree and placed inside the Virtex-5 in the NUMEXO2. The GTS fan-in/fan-out and the GTS root firmware programs are downloaded into the GTS V3 mezzanines, which are located in NIM units in a separate NIM crate that is reserved for the GTS. Fig. 33 shows a picture of the GTS V3 mezzanine. Each GTS V3 has one upstream and three downstream optical links, where each upstream link either from a GTS leaf or from a GTS fan-in/fan-out unit is connected to a downstream link from the upper GTS level. Finally, all nodes converge at the GTS root node, whose upstream link is connected to the GTS trigger processor. The trigger processor is the element at the top of the GTS tree and it is in charge of the event validation and rejection.

The full NEDA array (331 detectors) will use 21 NUMEXO2 boards, capable of sampling up to 336 channels and will require a total of 11 GTS V3 units, 10 of them used as 3-to-1 fan-in/fan-out units and one as a root module. For the setup with 48 NEDA detectors, two GTS V3 (one fan-in/fan-out and one root node) are required since only 3 NUMEXO2 boards would be used.

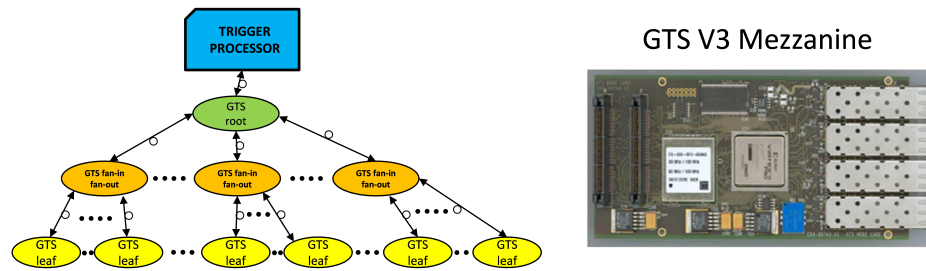


Figure 33: Left: hierarchical topology of the GTS tree, Right: GTS V3 mezzanine.

### 6.7.1 GTS Crate interface

The connections of the GTS V3 mezzanine are the following:

- One SFP connector for the upstream optical link to the top of the tree.
- Three SFP connectors for the downstream optical links to the bottom of the tree.
- Two Mictor connectors for power supply, control and trigger.

Depending on the position in the GTS tree, the proper file (`root.mcs`, `fanin-fanout.mcs`, `leaf.mcs`) must be downloaded to its Xilinx PROM. Firmware and embedded software (VxWorks OS) files are obtained from the GTS experts in Padova that are working on the AGATA project. A block diagram of the GTS NIM module is shown in Fig. 34.

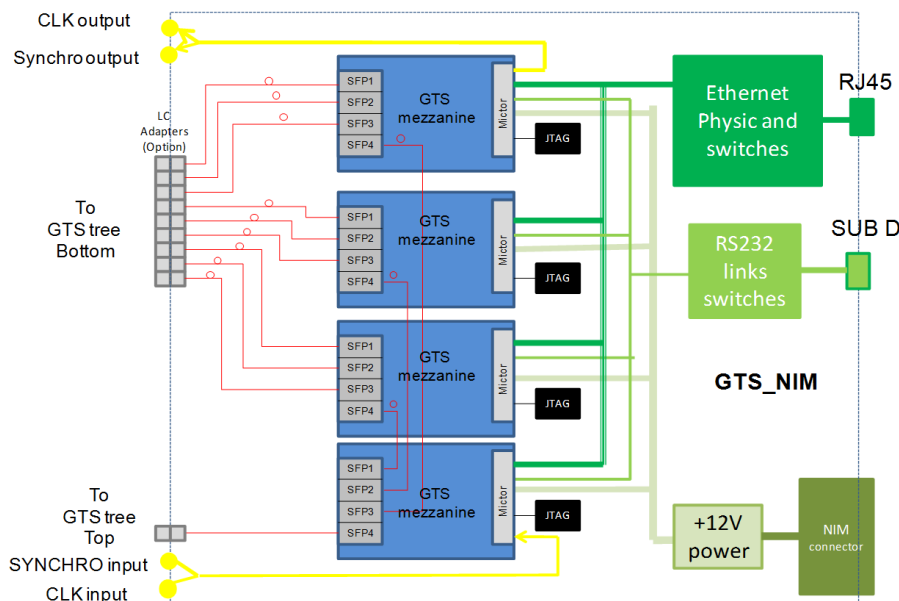


Figure 34: Block diagram of the GTS carrier NIM module.

The GTSN NIM module contains the following:

- Four GTS V3 mezzanines implemented on one NIM carrier board. One of the GTS V3 mezzanien, the so called top mezzanine, is linked to the three other GTS V3 mezzanien, the so called bottom mezzanien. The three downstream SFP connectors of the top GTS V3 are optically linked to the upstream SFP connector of the three bottom GTS V3s mezzanien.
- Front panel:
  - Nine downstream links of the 3 bottom GTS V3 towards the bottom of the tree. Front



panel connectors could be SFPs of the GTS V3 or LC fiber optic adaptors.

- One upstream link of the top GTS V3 towards the top of the tree. Front panel connector could be SFP of the GTS V3 mezzanine or LC fiber optic adaptor.
- One differential PECL 100 MHz clock output sourced by one bottom GTS V3 from a Mictor connector. Front panel connectors are SMA or double Lemo 00. Jumpers select the connection of signals to connector pins or to 50  $\Omega$  GND pulldown resistor.
- One differential PECL synchronisation signal output sourced by a bottom GTS V3 from the Mictor connector. Front panel connectors are SMA or double Lemo 00.
- One differential PECL 100 MHz clock input, sourcing the top GTS V3 from the Mictor connector. Front panel connectors are SMA or double Lemo 00.
- One differential PECL synchronisation signal input, sourcing the top GTS V3 from the Mictor connector. Front panel connectors are SMA or double Lemo 00.

- Rear panel:

- One Ethernet 100 link for control purpose of GTS V3. Each mezzanine has an IP number and is addressed through the Mictor connector. An Ethernet switch is implemented to select one of the four GTS V3 mezzanines. The rear panel connector is RJ45.
- One serial link for debugging GTS V3. Each mezzanine is addressed through the Mictor connector. Jumpers select one of the four GTS V3 mezzanines. Rear panel connector is DB9.
- One NIM connector providing the power for the GTS V3 mezzanines: 12 V, 3 V and GND.

- Inside the module:

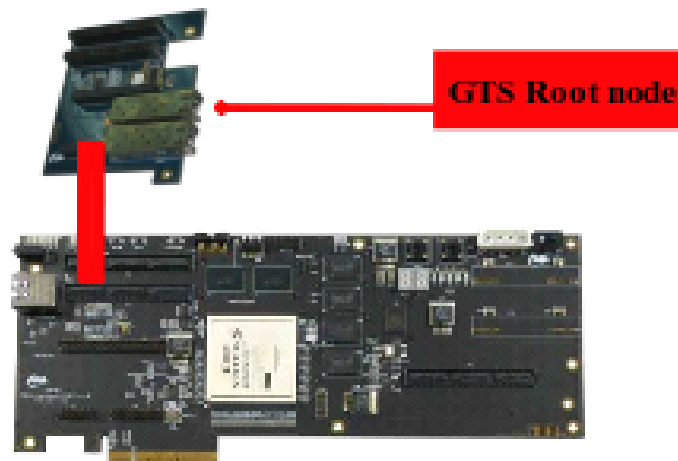
- Four ( $2 \times 7$  pins) JTAG connector devoted to download FPGA firmware files and debugging. Because the GTS V3 is provided with its FPGA code programmed into the PROM, a downloading action can be avoided. There is one JTAG connector per GTS V3.
- 50  $\Omega$  resistors must be put between each unused PECL 100 MHz clock output pin and GND.

## 6.7.2 GTS Trigger Processor

Most of the hardware, firmware and software components are retrieved from AGATA. The main hardware component of the trigger processor which is optically connected to the GTS V3 root is a commercial PCIe card plugged into a PC, the Xpress GenV5ä200. A photograph of the trigger processor board is shown in Fig. 35.

The trigger processor algorithms, which establish either a validation or a rejection of the event, can be various depending on the experimental context. The most common algorithm is the detection of the multiplicity within a coincidence time window. When performing this algorithm the trigger processor collects the timestamps of the incoming trigger requests. Inside the trigger processor, a coincidence time window is used as buffer, within which the timestamps of surrounding events are compared. A validation is provided in case the number of events (multiplicity) within the coincidence time window overcomes a certain threshold. Fig. 36 shows the algorithm structure.

### SFP with Gbit links: SFP HSI



### XpressGen2V5 200 development board

Figure 35: Trigger processor board.

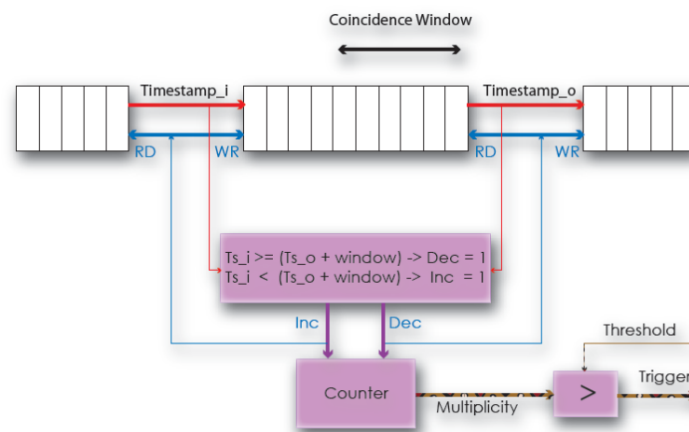


Figure 36: Multiplicity trigger algorithm implemented in the GTS Trigger processor.

## 6.8 Basic System Firmware and Software

Model V6-LX130T of the Virtex-6 FPGA from Xilinx is the largest device in NUMEXO2. It carries out most of the pre-processing tasks such as de-serialisation, triggering algorithms, configuration and oscilloscope. Fig. 37 shows all the firmware blocks of the Virtex-6 device.

### 6.8.1 Virtex-6 Firmware IPs

#### 6.8.1.1 Input interface ISERDES

The first stage of data readout is performed by using a customised arrangement of serialisation/de-serialisation data sub-blocks (called ISERDES), prepared to work at rates higher than 400 Mbps. Internally, the concatenation of the ISERDES blocks include always their own IODELAY coping properly with the delay adjustment. (The ISERDES and IODELAY sub-blocks belong to the Xilinx corporation as well as the arrangement of those to be prepared to work on for data collection of the

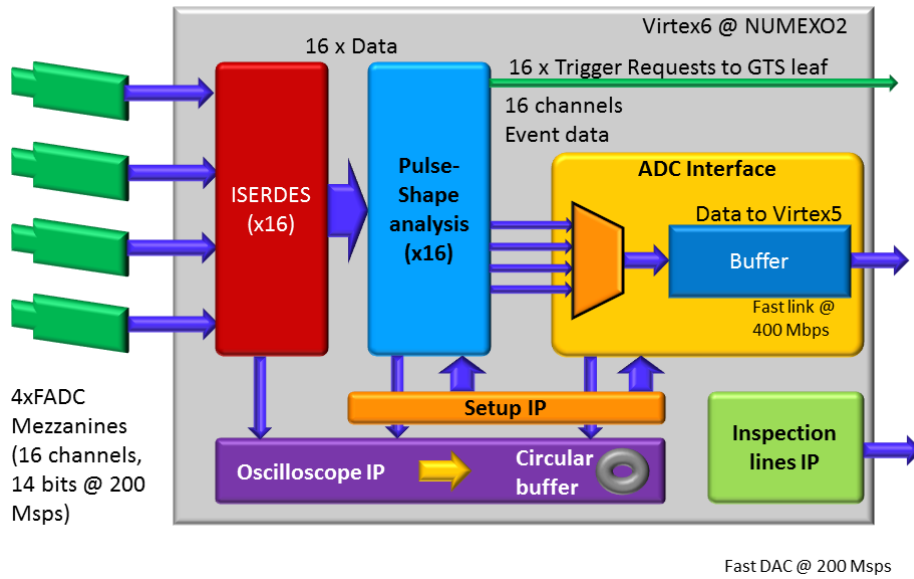


Figure 37: NUMEXO2 Virtex-6 block diagram.

889 ADS62P49.)

890 ISERDES IP has been implemented to deliver four 14 bit outputs, each containing the corresponding  
 891 even/odd samples of 2 FADC channels as shown in Fig. 38, while at the inputs there are 14 LVDS  
 892 channel, containing even/odd multiplexed bit duplets. The de-serialisation is performed with a DDR  
 893 clock latching the odd bits on the rising edge and the even bits on the falling edge, requiring two  
 894 clock cycles of the FADC output clock to create an output sample at the ISERDES IP output.  
 895 Additionally, a half-rate clock is delivered too, which is used as the Chip Scope Pro logic analyser  
 896 sampling clock.

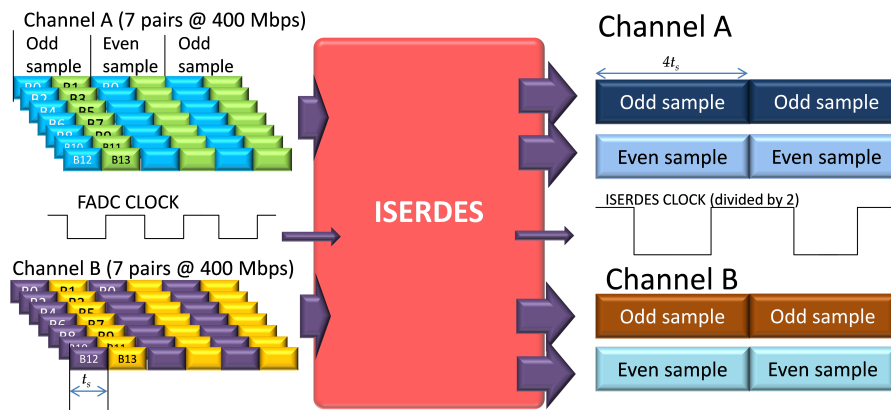


Figure 38: ISERDES functional block diagram.

### 897 6.8.1.2 Data management

898 Sources of NEDA data are the 16 channel samples from FADC mezzanines. Once raw samples are  
 899 de-serialised, only 250 samples of each channel are kept and sent to the Virtex-5. For each of the  
 900 16 channels, the selection window is triggered by the digital discrimination of the raw sample input.  
 901 The protocol is synchronous and 8 bit data are sent on each transition of the clock. The clock  
 902 transfer and the FADC clock are synchronous.

### 6.8.1.3 Oscilloscope IP

Oscilloscope aims to control digital signals at different points of the processing of the 16 channels. The maximum frequency of the 2 byte signal is 200 MHz and up to four probes can be connected simultaneously. The binary samples of each probe are continuously stored into a 32 kbytes (16 kwords) circular buffer and its content is frozen as soon as a trigger is occurring. For each probe, the type of trigger and the time can be controlled by software:

- Trigger: input threshold, software command.
- Time base: 5 ns (FADC sampling frequency), 10 ns, 20 ns, 40 ns, 80 ns, 160 ns, 320 ns, 640 ns, 1280 ns, 2560 ns, 5120 ns, 10 240 ns, 20 480 ns, 40 960 ns, 81 920 ns, 163 840 ns.

The higher the time base is, the longer is the time inspection window. For example, time base = 163 840 ns (1 of 32768 samples is kept) gives an inspection window of about 2.68 s.

### 6.8.1.4 Inspection Lines

Mainly envisaged to monitor internal signals, enhancing the testability of the NUMEXO2. At the front panel, 2 analog and 2 digital signals can be visualised using LEMO connectors. The wide assortment of selectable signals can be accessed by means of the internal multiplexers inside the V6 and the 2 fast digital-to-analog converters (DACs), allowing visualisation of analog signals. Signals that can be selected are the raw-data input, the output of the trapezoidal filter and the analog-wise conversion of the formatted frame. Regarding the digital lines, several clock sources, trigger signals from the digital CFD and other internal control lines can be selected.

### 6.8.1.5 Set-up register bank

Contains a set of registers used to configure the rest of the blocks within the Virtex-6, aiming to provide a flexible, dynamic and easy-to-configure device. Registers can be read and written using the software tool GECO (Ganil Electronic COntrol), working under the TCP/IP protocol via the Virtex-5. Some of the parameters that the setup block can set are the IODELAY step value, the parameters of the neutron- $\gamma$  discrimination algorithm, the timescale for the oscilloscope mode and the possibility to either choose parametric or oscilloscope mode in case of using EXOGAM2 electronics via the slow link.

## 6.8.2 Virtex-5 Firmware IP and Embedded Software

A second programmable device on the NUMEXO2 is the Virtex-5 FX70T device, which manages the data reception from the Virtex-6 after the processing. It also manages the communication ports and includes the GTS leaf, linking NUMEXO2 with the GTS. Fig. 39 shows the multiple blocks inside the Virtex-5, described in the following subsections.

### 6.8.2.1 ADC Interface

The ADC interface block carries out multiple functionalities on the other side of the Virtex-6. Firstly, it receives and unpacks the data frame from Virtex-6 putting it into a buffer and sends the event data to the GTS leaf waiting for it to be validated/rejected. Also, at this level, if the event was validated from the GTS, the leaf attaches the received timestamp and the ADC interface takes the data bundled with the timestamp either to the PowerPC (PPC) in the testing phases of NEDA or to the PCIe through the LINCO2 interface when NEDA is used in real experiments.

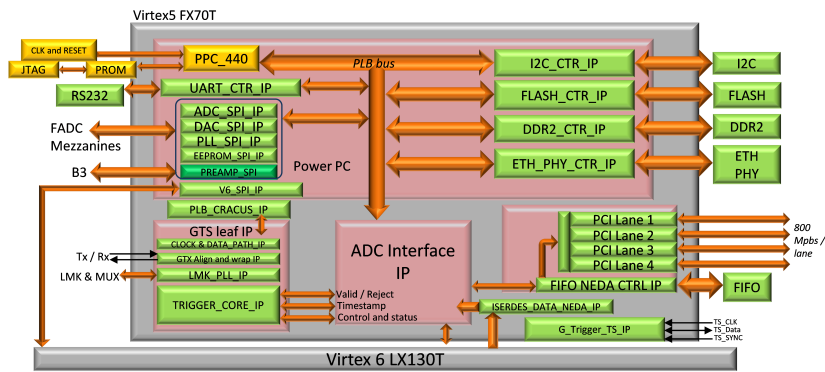


Figure 39: NUMEXO2 Virtex-5 internal block diagram. Courtesy of GANIL.

### 6.8.2.2 GTS leaf and PLB Cracus IPs

Inherited from AGATA, the GTS system aims to provide synchronisation in digital multichannel systems and event acceptance/rejection. Considering that the GTS system as a tree-structure, the GTS leaf is hierarchically placed at the bottommost part, and transmits the events from the ADC interface to the rest of the GTS, placed outside the Virtex-5. Each NUMEXO2 contains one GTS leaf, connected optically to the GTS NIM crate and is capable of managing 16 channels.

PLB\_cracus is a set of 32 bit registers, which interface the PLB bus and the GTS leaf IP. There are three types of registers: `reg_ctrl_i` (written by the PPC), `reg_ctrl_default_i` (register values at power on), and `reg_status_i` (read by the PPC).

A block diagram of the GTS leaf is shown in Fig. 40.

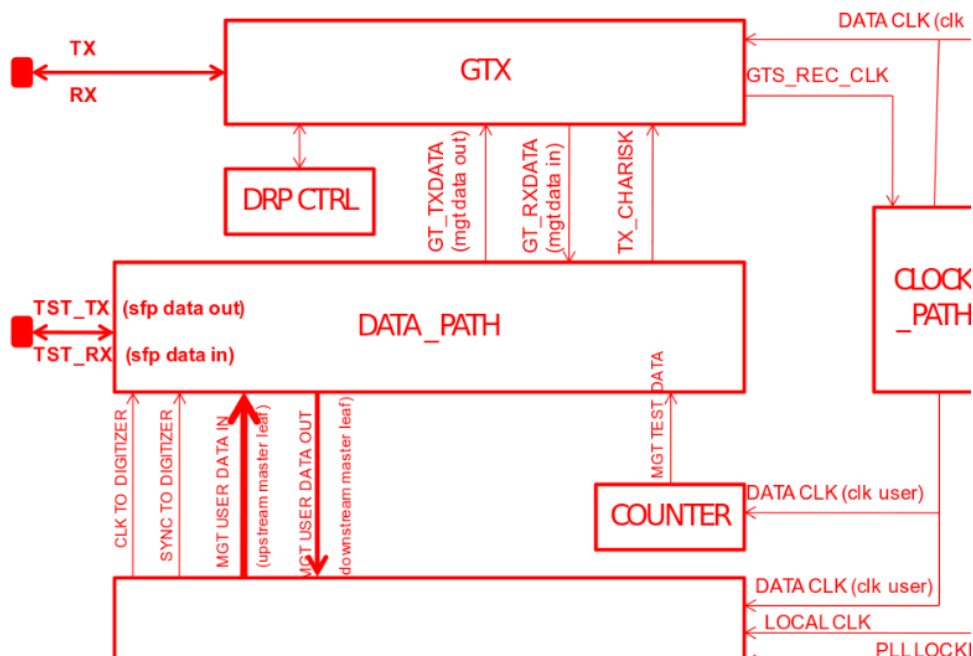


Figure 40: GTS leaf block diagram.

Other functionalities of the GTS leaf:

- Optical transceiver/receiver control: a clock multiplexer that allows the selection between several input clock sources (local oscillator, recovered from the GTX, external), providing it to a PLL.

- Data path block: aiming to equalise the phase of the GTX and control the data direction (TX or RX).
- Trigger core: mainly used to exchange messages between the Virtex-6, the trigger request and the transceivers.
- At the leaf level: the timestamp is generated and attached to the validated/rejected event. It consists of a 48 bit counter, with a resolution of 10 ns.

The trigger validation/rejection can be sketched easily with the chronogram shown in Fig. 41. After the triggering algorithm identifies the pulse to be due to a neutron, a trigger request is sent to the GTS leaf. Inside the leaf, a timestamp is attached, which is used to tag the moment at which the trigger request was stored with a resolution of 10 ns. Then, the GTS leaf sends the event to the trigger processor, waiting to be validated/rejected. The time elapsed between the trigger request and the notification to the trigger processor is called local latency, which mainly the GTS leaf is responsible for and which usually is 1 clock cycle. Together with the validation/rejection signal received, the field (named `val_rej_tag[7:0]`), contains the timestamp of the event that was previously sent to the trigger processor, and the event counter, which is placed in the last three bytes.

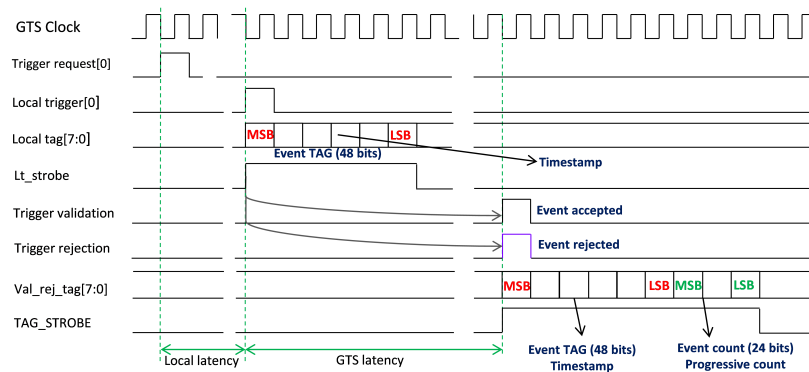


Figure 41: GTS chronogram cycle.

### 6.8.2.3 Embedded PowerPC

Virtex-5 includes a hardware PowerPC 440 processor with an embedded Linux OS, facilitating to cope with the complexity of the TCP/IP protocol. The processor carries in itself a good part of tasks among which one can find the configuration of the rest of the blocks inside the Virtex-5, such as the Ethernet Gigabit management, configuration of the PCIe setup registers, the GTS leaf setup (performed through the PLB Cracus IP), interaction with the Virtex-6 setup, FADC mezzanine SPI registers, B3 registers, as well as the management of external Flash (256 MB) and DDR (1 GB) memories and a serial port which allows to monitor the status of the booting of the Linux OS. Although Virtex-5 can be clocked from many sources as detailed in GTS leaf paragraph 6.8.2.2, the PPC is the only device in the whole NUMEXO2 module that always must be clocked from a local clock.

### 6.8.2.4 I/O Ethernet/PCIe

NUMEXO2 includes as well an optical link containing 4 PCIe Endpoint lanes, capable to run up to 3.2 Gbps (800 Mbps each), fulfilling NEDA specifications in terms of data throughput. In the middle of the PCIe driver there is a FIFO used to buffer the data between the ADC interface and the driver itself. Fig. 42 shows the block diagram of the PCIe and PCIe\_FIFO IPs.

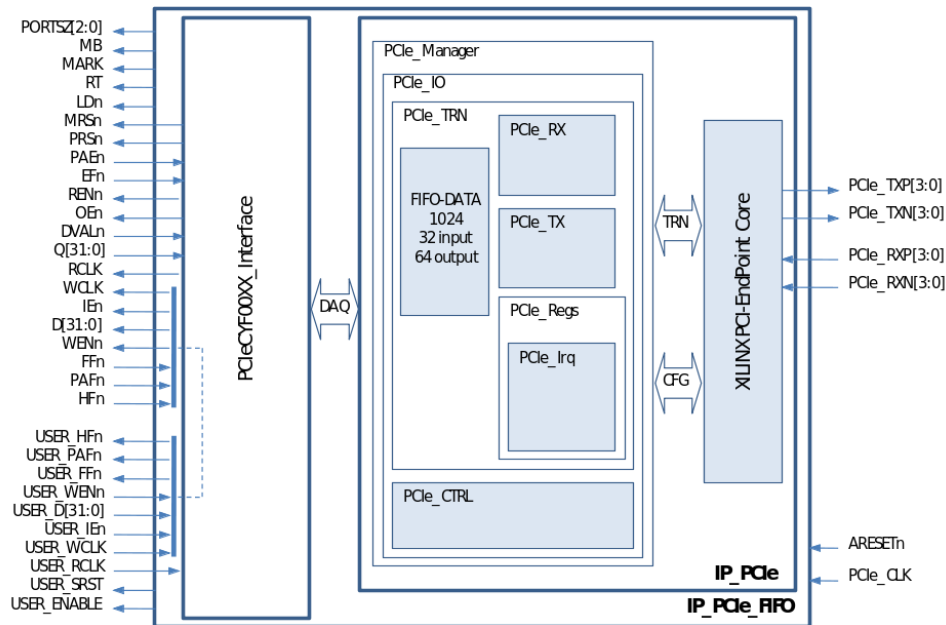


Figure 42: PCIe block diagram.

## 6.9 Implementation of the NEDA Trigger Algorithm

The task of NEDA, when combined with a  $\gamma$ -ray spectrometer, is to provide a clue of the reaction channel for a certain nucleus, using the number of detected neutrons as a probe. The neutron detectors of NEDA are based on organic scintillators, which also are sensitive to  $\gamma$  rays. Therefore a method to distinguish between neutrons and  $\gamma$  rays is required. By using a real-time processing technique, to perform the discrimination of neutrons and  $\gamma$  rays on-line. an increase of the overall system efficiency would be achieved if only events produced by neutrons are of interest and if events produced by  $\gamma$  rays could be rejected.

Since the beginning of the study of the particle interaction with matter, a wide set of methods were developed to deal with the discrimination between particles based on PSA techniques. Although some of the methods provide remarkable discrimination ratios, when dealing with hardware implementation, it was preferred to focus on simple algorithms capable of providing good efficiency. Hence, the goal of the PSA implemented in the FPGA is to provide a first basic discrimination aimed to reduce the events produced by  $\gamma$  rays. Two methods are proposed: charge comparison and zero crossover.

### 6.9.1 Trigger Algorithms

The charge-comparison (CC) method provides a discrimination based on the integrated charge at different positions of the waveform after the start of the pulse. Amplitude-normalised average  $\gamma$  ray and neutron waveforms are shown in Fig. 43. As seen, there is a clear difference in the tail of the pulses. The CC method uses the ratio between the integral of the tail of the pulse (named slow component) and the integral covering the rising edge and part of the falling edge after the peak (called fast integral). This ratio, here called  $\delta$ , is then used to discriminate between neutrons and  $\gamma$  rays.

In the digital domain,  $\delta$  becomes  $\hat{\delta}$ , and  $\alpha$  and  $\beta$ , which are the integration limits over the fast and

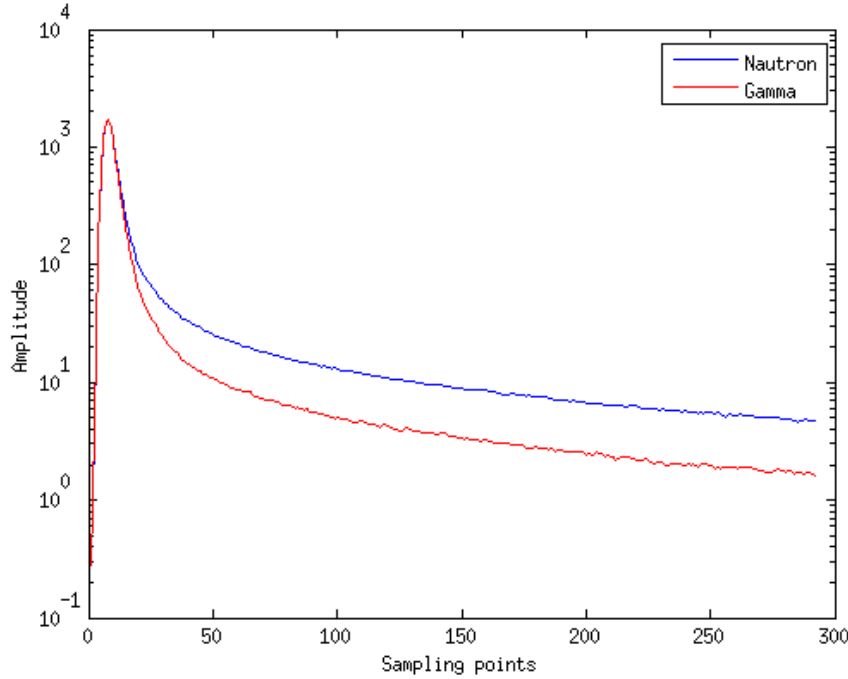


Figure 43: Examples of average neutron (blue) and  $\gamma$  ray (red) waveforms.

slow components, respectively, become sums according to this expression:

$$\delta = \frac{\int_{\beta} v(t) dt}{\int_{\alpha} v(t) dt} \rightarrow \frac{\sum_{n=\alpha+1}^{\beta} v(n)}{\sum_{n=1}^{\alpha} v(n)}. \quad (6)$$

The zero-crossover (ZCO) method is based on a shaping (either analog or digital shaping) of the pulse into a bipolar signal and on measuring the time between the leading edge of the original pulse, usually obtained by a CFD, and the zero-crossover of the bipolar signal. Neutrons give a larger zero-crossover time than  $\gamma$  rays as illustrated in Fig. 44.

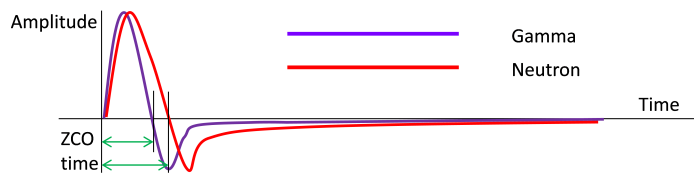


Figure 44: Illustration of the ZCO method for neutron- $\gamma$  discrimination.

In a similar manner as an analog shaper works, a digital shaper can be designed by means of difference equations by applying a conversion technique to the original analog transfer function. The resultant signal contains a fast component with positive sign and a slow component with negative sign. Comparing the response to the CR-RC, the convolution can be divided into three terms analogously to the integral and differential terms of the analog response. Additionally a smoothing function is used to make an average of each sampling point and its neighbors. Hence, the function can be written as

$$f(t) = h(t) * p(t) = h_s(t) * h_i(t) * h_d(t) * p(t). \quad (7)$$

Here,  $h_s(t)$  is a smoothing function,  $h_i(t)$  the integral term corresponding to the RC part and  $h_d(t)$  is the differential term. Finally,  $p(t)$  is the input and  $f(t)$  the output. The ZCO is computed



between the polarity change and the time when the original signal overcomes the threshold. The quality for the discrimination depends also on the time resolution of the ZCO time. Usually it requires interpolation techniques on the polarity change to enhance the resolution.

A comparison of the figure-of-merit values of the neutron- $\gamma$  discrimination performance was made for the CC and ZCO methods. In view of the smaller amount of resources required, especially in terms of hardware multipliers and the simplicity of control, the CC method was selected to be implemented in the Virtex-6 for on-line discrimination of neutrons and  $\gamma$  rays.

## 6.9.2 Charge-Comparison Method

The block diagram in Fig. 45 shows how the CC algorithm can be implemented in the FPGA. Given the raw data at 200 MS/s at the input, the algorithm delivers a signal to the GTS if the event detected was a neutron.

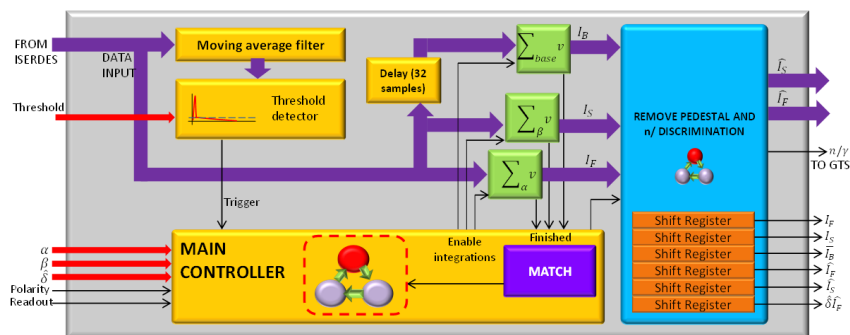


Figure 45: Hardware block diagram of the charge-comparison method.

Taking a closer look at the block diagram, the system architecture consists of a main controller based on a FSM, and a set of slave blocks used for threshold, integration and pedestal removal. Each sub-block has as well a local controller inside in case of complex operations. The blocks are the following:

- Main controller: enables/disables the rest of the blocks according to a set of parameters and to an execution sequence.
- Moving average filter: precedes the threshold detector. By using this filter, the threshold detection avoids spurious noise sources providing more robustness. For this case, an 8th order moving average is used.
- Threshold detector: delivers a pulse to the main controller if the signal crosses a certain level set by the user as a parameter.
- Integrators: using the recursive addition method, the integrators provide the slow, fast and baseline integrals  $I_S$ ,  $I_F$  and  $I_B$ , the last one being calculated over 32 samples preceeding the trigger. After an integral is finished, it sends a flag to the main controller indicating that the operation has been finished.
- Match unit: a sub-block inside the main controller, takes the flags after the integrations have been calculated and waits until the last integration is done. Afterwards, it sends a flag to the pedestal correction unit to start the following calculation process.
- Pedestal correction unit and neutron- $\gamma$  discrimination: gathered in the same block due to the reusability of the hardware resources, this multifunctional block calculates both the part of the integral that should be subtracted from the pulse and provides the trigger to the GTS after comparing both integrals with the parameter. Besides, it incorporates a set of 6 PISO

(Parallel-In Serial-Out) registers in case results of the integration is required to be read with a minimal amount of resources from a logic analyser. Hence, taking as the inputs  $I_S$ ,  $I_F$  and  $I_B$ , the block delivers:

$$\hat{I}_S = I_S - \beta \bar{I}_B \quad (8)$$

$$\hat{I}_F = I_F - \alpha \bar{I}_B \quad (9)$$

$$\begin{aligned} n/\gamma &= 1 & \text{if } \hat{I}_S \geq \hat{\delta} \hat{I}_F \\ n/\gamma &= 0 & \text{if } \hat{I}_S < \hat{\delta} \hat{I}_F \end{aligned} \quad (10)$$

To calibrate the values of  $\alpha$ ,  $\beta$  and  $\hat{\delta}$ , a normalised and averaged set of  $\gamma$ -ray and neutron waveforms have been used. Originally, the samples were collected by a Struck module at 500 MS/s. Afterwards, the waveforms were produced using an arbitrary waveform generator (Agilent 33522A). Fig. 46 shows the results obtained for different values of  $\alpha$  and  $\beta$ .

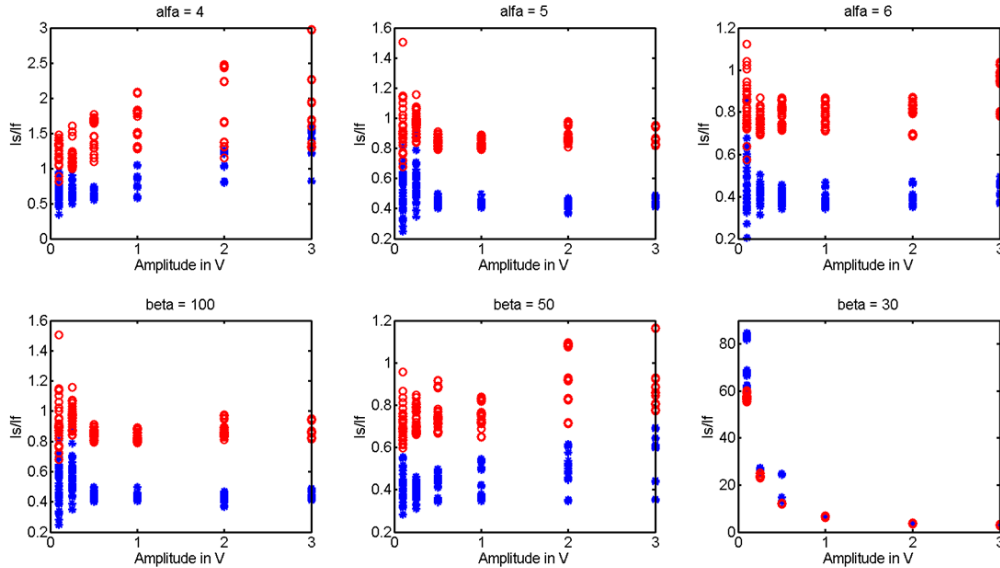


Figure 46:  $\hat{I}_S/\hat{I}_F$  versus signal amplitude. Upper: sweep across several  $\alpha$  values with  $\beta = 100$ . Lower: sweep across several  $\beta$  values with  $\alpha = 5$ . Events produced by  $\gamma$  rays are plotted as blue stars and neutrons as red circles.

In Fig.46, it can be seen that for  $\beta$  values smaller than 50, the neutron- $\gamma$  discrimination is completely lost. Good discrimination values have been obtained for  $\beta = 100$  and  $\alpha = 5$  and  $\alpha = 6$ . After scaling the decimal values of the integrals and applying a  $2^N$ -power factor to the result of  $\hat{I}_F$ , the  $\hat{\delta}$  value can be chosen as an integer number to facilitate the calculations.

## 7 Global Trigger and Synchronisation System

The Global Trigger and Synchronisation (GTS) system is responsible for the data synchronisation, clock distribution and trigger management in NEDA; as such, it is conceived as a stand-alone system completely decoupled from the readout chain. Its development has been inspired by the TTC (Timing, Trigger and Control) system at CERN LHC [34]. The GTS system is already fully operational in the AGATA experiment since 2009 [35, 36]. Nevertheless it has to be adapted for the NEDA requirements.

The NEDA data stream relies on an absolute time being available at the digitisation and pre-processing level. This implies the distribution of a high number of phase-locked and phase-matched clocks to all the digitising modules. The requirements on the GTS system may be summarised as follows:

- The clocks at the sampling FADCs have to be synchronised with a sub-ns precision. This avoids calibration steps that are time-consuming and impractical in NEDA, due to the high number of acquisition channels.
- The system must be able to sustain trigger validations at a rate of 1 MHz with channel multiplicity of 1 (e.g. a candidate event made of a single energy deposit in a pre-selected time window), and at a rate of 50 kHz with a channel multiplicity 30 (e.g. a candidate event made of up to thirty energy deposits in a pre-selected time window).
- The percentage of trigger loss, namely the trigger requests that can't be processed, has to be lower than a few percent.
- The system has to be scalable: going from 2 to 200 detectors should not induce any conceptual change in the hardware or software involved.

All data sent from one detector are processed on an NIM board called NUMEXO2 carrier that contains in total four mezzanine cards with two FADCs each. A pulse-shape analysis algorithm implemented in the core mezzanine issues a trigger request whenever a neutron is discriminated from  $\gamma$  rays. The GTS system forwards the requests to the global trigger processor and sends back the timestamp identifying the trigger requests. The timestamps of the trigger requests are used by the trigger processor for correlating requests from several detectors in order to possibly validate simple or time delayed coincidences. Upon receiving the trigger timestamp, the readout electronics records a snapshot of the incoming signals, filters them and waits for a possible validation. A validation or rejection of the candidate event eventually arrives from the trigger processor with a maximum latency of 20  $\mu$ s. Several requests can be sent before the arrival of the validation/rejection, hence the validation has to contain the timestamp of the original trigger request. Indeed, the order in which trigger requests are sent can differ from the order of reception of the validations; the sequence depends on the configuration of the trigger rule (e.g. delayed coincidence). Trigger requests and trigger validations include also an identification of the channel that is used by the trigger processor as geographical information for possible partitioning of the complex detector at the trigger level. The acceptance of a timestamp validation to a given channel triggers its local readout.

The readout electronics stores data in internal FIFOs. The system can be immediately rearmed after a trigger request and can accept other trigger requests as long as the internal buffers are not full. The trigger processor, which is the root of the GTS tree, assigns the event number, while forwarding its decision (validation or rejection) to the GTS mezzanine. When the event is accepted, the data are forwarded to the carrier board memory and hence, through a PCIe optical link, to the acquisition computer.

The design of the front-end readout follows a synchronous pipeline model: the detector data are stored in pipeline buffers at the global NEDA frequency, waiting for the global trigger decision. The time between the firing of a trigger request and the consequent validation or rejection is called the trigger latency. This latency is not required to be constant for each trigger request (and actually it is not), but it should fit within the pipeline buffer length. The whole system behaves synchronously; for a proper operation of the system, synchronisation at different levels has to be achieved and monitored. Table 7 summarises the five types of synchronisation present in the AGATA readout.

A variable but finite number of global time referenced signals are needed for guaranteeing synchronism of the system elements. In AGATA, they are conveyed through serial optical bidirectional links. These links connect the front-end and readout electronics of each crystal with a central global timing and synchronisation control unit in a tree-like structure, see Fig. 47. They merge together the three

Table 7: Synchronisation types

Synch. type	Description
Sampling	Synchronisation of the detector signals with the clock phase
Serial Link	Recovery of parallel data words from the serial bit stream
Trigger Requests Alignment	Alignment of trigger data at the input of the pipelined trigger processor
L1 Validations	Synchronisation of L1 validation signal with data into the readout pipelines
Event	Assignment of global clock and event number to data fragments in the DAQ path

1116 basic functionalities: synchronisation distribution, global control and trigger transport.

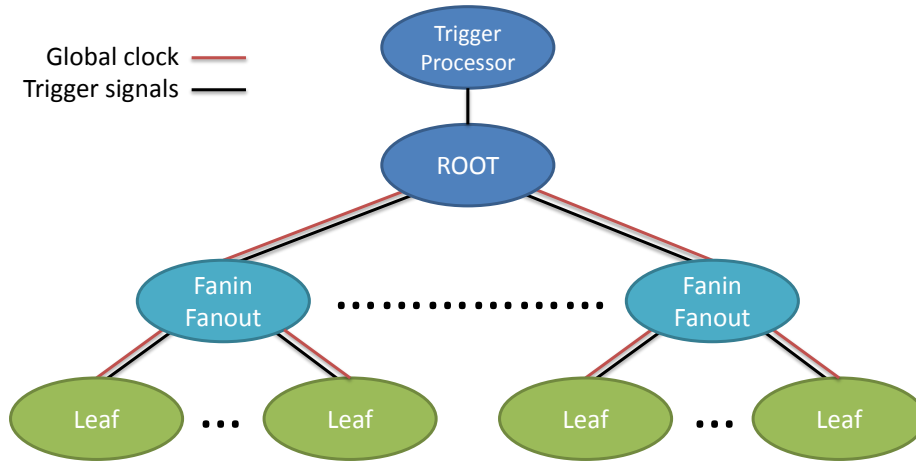


Figure 47: Topology of the GTS system

1117 All GTS nodes provide a fast ethernet connection, which is used for slow control and monitoring. A  
 1118 slow control procedure involving the whole tree allows the synchronisation of the clocks. Differently  
 1119 from the previous versions of GTS, in NEDA one GTS leaf should be able to serve multiple trigger  
 1120 requests in the same timestamp. To this end, as many trigger request lines are needed as the  
 1121 maximum number of detectors that concurrently may ask for a trigger. The trigger requesters will  
 1122 be implemented in the Virtex-6 FPGA of the NUMEXO2 board, while the GTS leaf will be on the  
 1123 Virtex-5 FPGA as the buffering of the events waiting for a validation or a rejection. Given the  
 1124 segmentation of the hardware, a maximum of 16 trigger requests are expected to be served for each  
 1125 clock cycle.

## 1126 8 Data Acquisition System

1127 NEDA will use the AGATA data acquisition (DAQ) system, which was already successfully used  
 1128 together with the MBS DAQ system during the AGATA-PRESPEC campaign at GSI in 2012 and  
 1129 2014. A description of the AGATA DAQ can be found in Ref. [1].

## 9 Neutron-Gamma Discrimination with BC501A and BC537

In this section, the NGD performance of four NEDA test detectors, filled with two different scintillators, the commonly used proton-based liquid BC501A and the deuterated liquid BC537, are compared. The newly built DESCANT array [37, 38] for neutron tagging experiments at TRIUMF-ISA is based on BC537, which has been claimed to have a better neutron energy response than BC501A. This feature could be used in combination with a measurement of TOF for neutron crosstalk discrimination [14]. Preliminary results of the work presented in this section have previously been reported in Ref. [39, 40]. Further details will be published in Ref. [41].

### 9.1 Scintillators

BC501A ( $C_8H_{10}$ ) [42, 43] has a light output that is about 78 % of anthracene and a hydrogen to carbon ratio of 1.287. It has three decay components with decay times of 3.16 ns, 32.3 ns and 270 ns [44]. BC537 [45] is made of purified deuterated benzene,  $C_6D_6$ , and has a light output that is about 61 % of anthracene, a deuterium to carbon ratio of 0.99 and a deuterium to hydrogen ratio of 114. The decay components of BC537 are not listed in the data sheet, but assumed to be similar to BC501A. For both scintillators, the relative amount of light produced by the fast and slow decay components is different for different particle species, which is the property used for NGD.

### 9.2 Experiment

The experimental setup is illustrated in Fig. 48. Four detectors (two BC501A, two BC537) of cylindrical shape and with a size of 5 inch by 5 inch were studied. The detectors were coupled to 5 inch diameter 10-stage photomultiplier tubes of the type XP4512 and with voltage dividers of type VD105K. A cylindrical 3 inch by 3 inch  $BaF_2$  detector was used as time reference for the TOF measurements. The data sets were collected using two neutron detectors and one  $BaF_2$  detector, triggered by a coincidence between the  $BaF_2$  detector and at least one neutron detector. CFD thresholds of 20 mV, corresponding to about 80 keVee, were used for both neutron detectors.

The anode signals from the detectors were digitised a STRUCK digitiser of model SIS3350 [46]. The SIS3350 has four channels with a sampling frequency of 500 MS/s and a resolution of 12 bit. This sampling frequency and bit resolution has been shown to be sufficient for PSA of the signals from liquid scintillator detectors [47]. Additionally a STRUCK digitiser of model SIS3302 [48] was used to digitise some of the slower analogue signals from the time-to-amplitude converters (TAC) and from the PSD unit. This digitiser has eight channels with a sampling frequency of 100 MS/s and a resolution of 16 bits. The analogue PSD was performed by using a BARTEK NDE202 unit [49], which was developed for and which is used by the Neutron Wall array [30]. For the TOF measurements a TAC was used with the neutron detector signal as start and the  $BaF_2$  signal as stop. The digitisers communicated with the data acquisition system via a VME controller using an optical link. The original data acquisition control software [50] was modified for this purpose.

The data were collected using several  $\gamma$ -ray calibration sources and a  $^{252}Cf$  neutron source with an activity of about 2 MBq.

### 9.3 Pulse-Shape Discrimination

Several sophisticated methods for digital pulse-shape discrimination in BC501A have been developed by various research groups, for example using artificial neural networks [51, 52],  $\chi^2$  fitting [53, 54], correlation functions [55], fuzzy logic [56, 57] and a pulse gradient method [58, 59]. All these

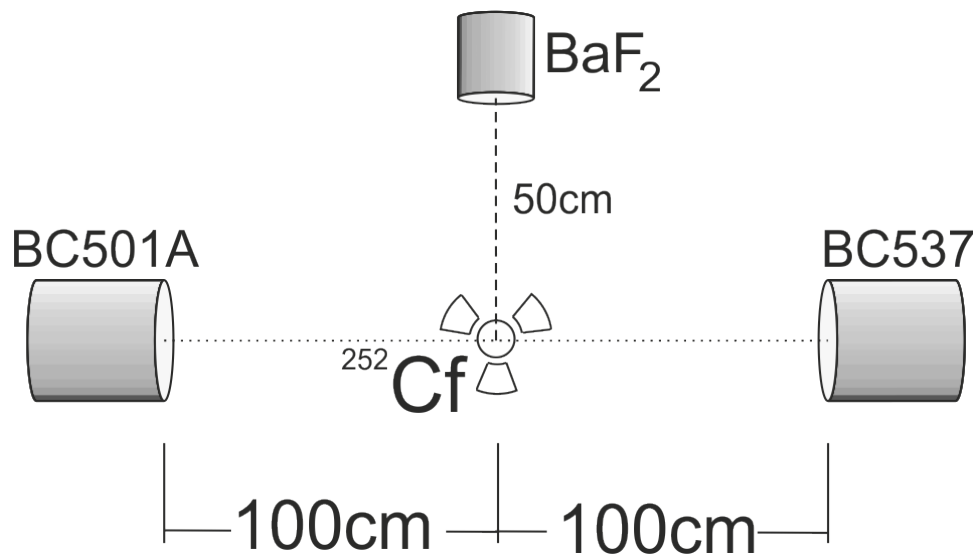


Figure 48: Illustration of the experimental setup.

methods have yielded good results regarding the discrimination of neutrons and  $\gamma$  rays. PSD of both proton-based and a deuterated liquid scintillator has been studied in Ref. [53]. However, in that work the detectors filled with different scintillators were not of the same size and worked in a different energy range. Therefore, it is difficult to draw conclusions from that work on how the performance of the two scintillators differ.

To minimise the influence of different electronics on the results, data sets with the same photomultiplier tube and electronics chain were used, where only the detector cell itself was different. In Ref. [60], BC501A and BC537 were compared using charge-comparison methods and BC501A was shown to perform better for low energy neutrons. However, no method taking full advantage of digital data analysis, for example a machine-learning algorithm, was implemented in that work.

Two methods were used to evaluate the NGD capabilities of the two scintillators. These were the digital implementation of the charge-comparison method, as described in Ref. [47], and artificial neural networks, as described in Ref. [52]. The fast component of the charge-comparison method was chosen to be 12 sampling points, which is in the time range 0 ns to 24 ns relative to the trigger. The slow component was defined as starting after 24 ns relative to the trigger and to have a variable length, extending to the maximum value of the integral. Average pulse shapes from BC501A and BC537 are shown in Fig. 49, together with the limits used for the different pulse-shape discrimination methods used.

A feed-forward neural network was created based on the ROOT `TMultiLayerPerceptron` class [61]. It was designed with 75 input nodes, corresponding to the first 75 sampling points after the leading-edge discriminator in the waveform, two hidden layers of 20 and 5 nodes, respectively, and an output layer with one node where the value 0 corresponds to a  $\gamma$  ray and the value 1 corresponds to a neutron. For each scintillator, the network was trained using 50000 events, and another 50000 events were used to test it. Of these  $10^5$  events, about 42000 (53000) were identified as  $\gamma$  rays and 58000 (47000) were identified as neutrons for BC501A (BC537). One reason for the discrepancy in the number of identified neutrons and  $\gamma$  rays could be the lower light output of BC537, which means that more neutron events will be below the detection threshold. The network was trained using the Broyden-Fletcher-Goldfarb-Shanno [62, 63, 64, 65] method. The typical error in the training data was  $\approx 5\%$  and  $\approx 6\%$  in the test data for BC501A, which confirmed that the neural network architecture was good. In Ref. [52], the network was trained using data taken at 300 MS/s in a time window between 0 ns to 237 ns (71 sampling points used as input nodes). In the present experiment, the sampling frequency was 500 MS/s and the time window was limited to 0 ns to 150 ns (75 input

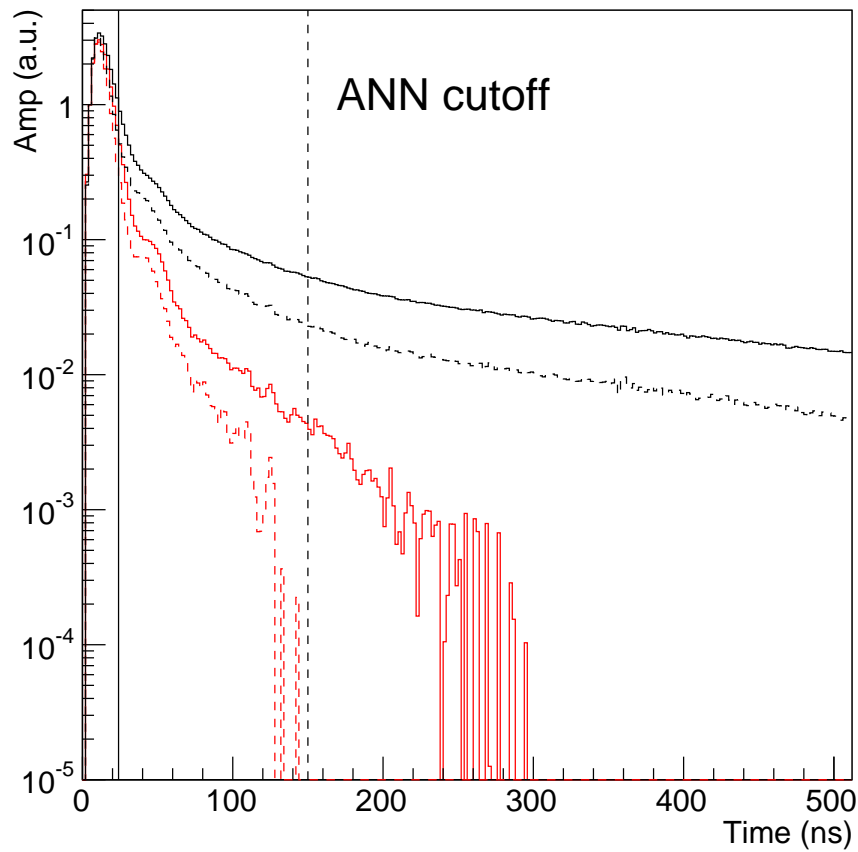


Figure 49: Average pulse shapes from BC501A (solid histogram) and BC537 (dashed histogram) for neutrons (black) and  $\gamma$  rays (red, grey). The solid vertical line shows the division between fast and slow scintillation components used for the charge-comparison algorithm, while the dashed line shows the cut-off time used in the artificial neural network analysis.

1203 nodes) in order to keep the size of the network small.

1204 Neutrons and  $\gamma$  rays were identified using three two-dimensional cuts: total charge (light produced in  
 1205 the scintillator and collected by the photomultiplier tube) versus TOF, total charge versus analogue  
 1206 PSD parameter, and TOF versus analogue PSD parameter, shown in Fig. 50. These cuts were used  
 1207 both for training of the artificial neural network, as well as for quantifying the performances of the  
 1208 different discrimination methods.

1209 Qualitative results from the artificial neural network applied to the full data set without pre-selection  
 1210 of neutrons and  $\gamma$  rays are shown in Fig. 51. In this figure, events identified as neutrons, with an  
 1211 output value from the artificial neural network larger than 0.99, are shown. As seen, the number of  
 1212  $\gamma$  rays are heavily reduced compared to Fig. 50, both inside and outside the gates used for training  
 1213 of the network. This shows that the artificial neural network works well for all events and that the  
 1214 selection of events for training and evaluation does not introduce a bias in the network.

1215 Two limits were defined for the different PSD algorithms, one containing 75 % of the neutrons in the  
 1216 selection and the other containing 95 % of the neutrons in the selection. See illustration in Fig. 52.

1217 The mis-identification error,  $\epsilon_{\gamma}$ , was then defined as the fraction of  $\gamma$  rays that was present within  
 1218 the neutron limit. Since this definition only includes the fraction of  $\gamma$  rays under different conditions  
 1219 it is independent of the relative number of emitted  $\gamma$  rays and neutrons. However, it is worth noting



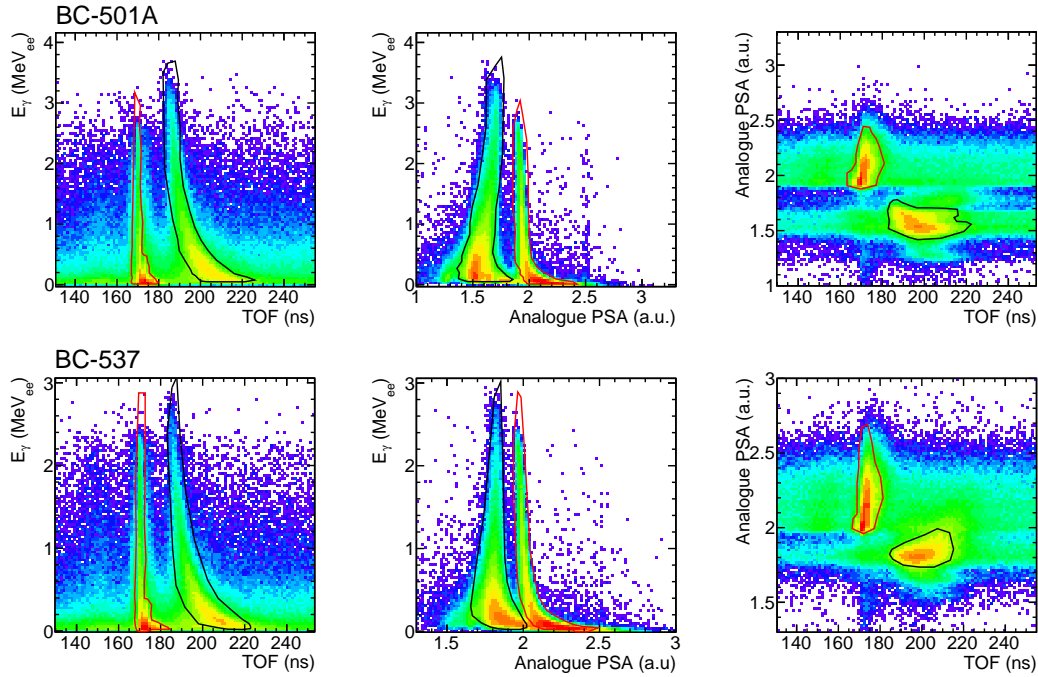


Figure 50: Two-dimensional cuts for selection of neutrons (black) and  $\gamma$  rays (red) for BC501A (top) and BC537 (bottom). The cuts are made on energy versus TOF (left), energy versus analogue PSD (middle) and TOF versus analogue PSD (right). An event is considered valid if it is present in all three cuts for a given scintillator cell. The scale on the z-axis is logarithmic for all plots.

that in a real experiment the neutron selection is usually based both on PSD and TOF. Thus, the final  $\epsilon_\gamma$  will be drastically reduced. The results are shown in Fig. 53.

One should note, however, that the electron equivalent light output depends on the intrinsic properties of the scintillator, in particular the light output per keV of deposited energy. For  $\gamma$  rays, this effect is cancelled by the calibrations. For BC501A the relation between the energy deposition of neutrons and  $\gamma$  rays is known to have a non-linear behaviour [43, 47], while the corresponding relation for BC537 has not been studied. Therefore, data points with the same energy in keVee do not necessarily correspond to the same incoming neutron energy for different scintillators.

The results show that BC501A performs better than BC537 over most of the energy range. This might be due to the fact that, for the same energy, BC501A gives a larger light output than BC537 because of the scattering kinematics. The improvement in discrimination between neutrons and  $\gamma$  rays using artificial neural networks are also consistent with the results in Ref. [52] both for BC501A and for BC537. It is also worth pointing out that the artificial neural network in this work uses only 150 ns of the pulse length, while the charge comparison uses 500 ns of the pulse length. Thus, it is possible that the artificial neural network results would improve even further if the number of input nodes is increased from 75 to 250. However, in this work 75 nodes were considered sufficient for evaluating the difference in performance of the two liquid scintillators while keeping the required computing power down.

## 9.4 Summary

The two liquid scintillators BC501A and BC537 were compared with respect to their NGD properties. It was shown that BC501A gives a better NGD performance than BC537. The worse NGD properties of BC537 compared to BC501A can be explained by the relatively smaller amount of scintillation photons and photoelectrons in the slow component of the pulse for BC537.

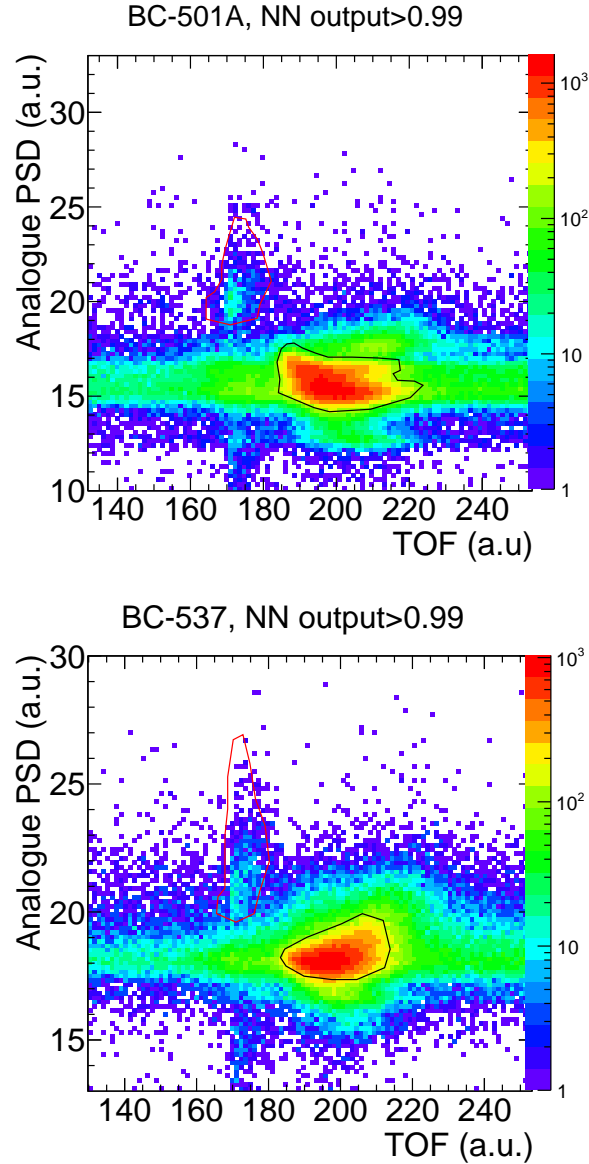


Figure 51: Two-dimensional cuts on time-of-flight versus analogue pulse-shape-discrimination for selection of neutrons (black) and  $\gamma$  rays (red) for BC501A (top) and BC537 (bottom) after neutron identification with the artificial neural network, with a network output  $> 0.99$ .

## 10 Digital Timing Measurements

NEDA has been conceived to use digital electronics with a sufficiently high sampling rate to enable good timing and NGD performance. For this purpose, a digitiser with 14 bits (11.7 effective number of bits; ENOB) and a sampling rate of 200 MS/s has been designed [27], see section 6

At present it has not been convincingly demonstrated that low sampling frequency digital modules are competitive with their analogue predecessors for fast photomultiplier tubes (PMT). Therefore, it was necessary to carefully check how the sampling rate and bandwidth constrain the digital timing performance compared to that obtained with analogue electronics. For example, for very fast timing applications, it has been shown that digital algorithms for BaF<sub>2</sub> scintillators, using a 1 GS/s sampling ADC, can give a timing performance that is better than that obtained with traditional analogue systems [66].

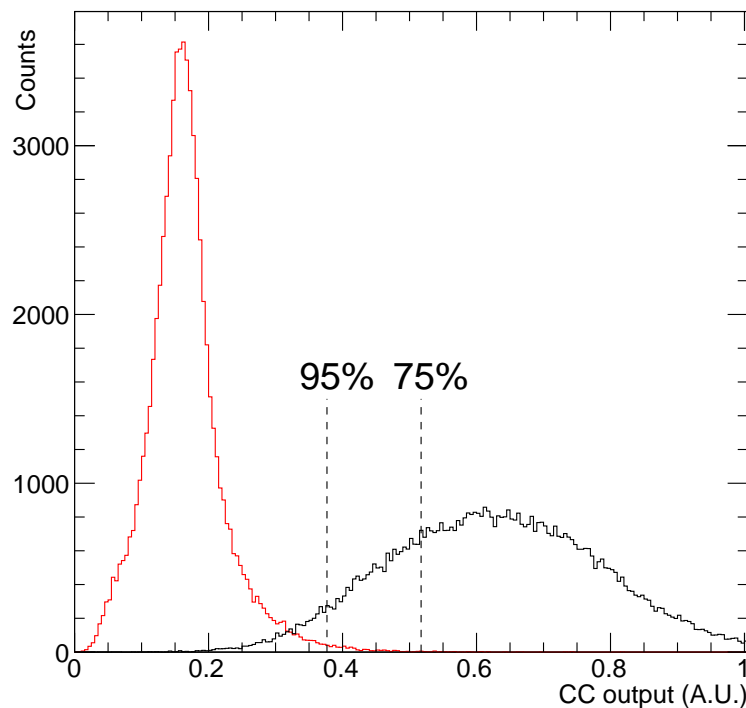


Figure 52: Example of a charge-comparison distribution (red, grey) and neutrons (black) for the BC501A scintillator. In this case, the 75 % neutron efficiency gate is in the interval  $[0.52, 1]$  and the 95 % neutron efficiency gate is in the interval  $[0.38, 1]$ .

Besides achieving the best possible timing resolution, digital systems have been widely employed for PSA to perform NGD with organic scintillators [67], using the zero-crossing [68] and double integration methods [69, 70]. Specifically for the BC501A scintillator, digital NGD has been widely exploited [71, 47, 52, 72] and it has been shown that for PSA purposes a digitiser with a sampling rate of 200 MS/s and a resolution of 14 bits is suitable [47].

The present work aims to study the pulse-timing performance of four 5 inch PMTs (XP4512, ET9390-kb, R4144 and R11833-100) coupled to a 5 inch by 5 inch BC501A scintillator detector. In order to quantify the timing properties of the PMTs, a CFD algorithm was developed. The zero-crossing of the CFD was obtained with a cubic spline interpolation, which was continuous up to the second derivative. The waveforms were digitised with a 12 bit resolution 500 MS/s FADC and were down-sampled to 200 MS/s in order to mimic the future electronics of the NEDA array. The performance of the algorithm, with respect to the timing resolution, was studied at the sampling rates 500 MS/s and 200 MS/s and compared to results obtained with a standard analogue CFD.

## 10.1 Experimental Setup and Measurements

A schematic picture of the experimental setup is shown in Fig. 54. Gamma rays from a  $^{60}\text{Co}$  source were measured in coincidence between a cylindrical 5 inch by 5 inch BC501A liquid scintillator detector and a cylindrical 1 inch by 1 inch  $\text{BaF}_2$  crystal. The distance from the source to the front face of the detectors was 20 cm and 5 cm for the BC501A and  $\text{BaF}_2$  detectors, respectively. The detectors were placed at an angle of  $90^\circ$  with respect to the outgoing  $\gamma$  rays. A 5 cm thick lead shield was placed between the detectors in order to minimise the detection of  $\gamma$  rays that were scattered from one detector into the other. The lead brick did not shadow the detectors from the

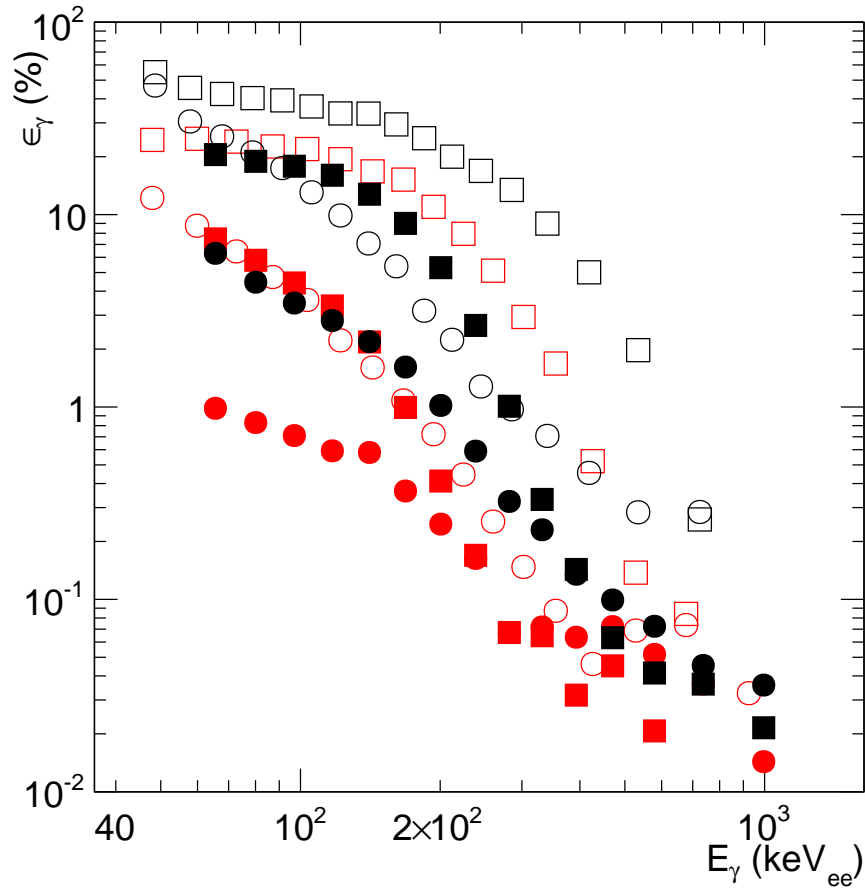


Figure 53: Fraction of  $\gamma$  rays that leaks into the neutron gate ( $\epsilon_\gamma$ ) for the 75 % neutron efficiency gate (red, grey) and the 95 % neutron efficiency gate (black). BC501A is shown as closed symbols and BC537 open symbols. The two discrimination algorithms are: artificial neural networks (circles) and charge comparison (squares). Note that the electron equivalent energy is related to the  $\gamma$ -ray energies in the detector, and not to the energies of the incoming neutrons.

<sup>60</sup>Co source.

The tested 5 inch PMTs were Photonis XP4512, Hamamatsu R4144, Hamamatsu R11833-100 and ET Enterprises ET9390-kb, which in turn were coupled to the same liquid scintillator detector. The BaF<sub>2</sub> crystal was coupled to a fast 2 inch PMT of model Hamamatsu R2059. All PMTs were magnetically shielded with  $\mu$  metal. The high voltage (HV) of all tested PMTs was set to get an anode signal amplitude of 1 V/MeV, while the HV for the BaF<sub>2</sub> PMT was set to -1806 V. Table 8 shows the HV values used for the 5 inch PMTs.

The anode signals from the detectors were connected to LeCroy N428A linear fan-in/fan-out units, from which the output signals were sent to the sampling ADCs and to analogue CFD units of type Phillips 715. The values of the thresholds and shaping delays of the CFD for the 5 inch PMTs are given in Table 8. The thresholds were adjusted to the minimum and the shaping delays were optimised to obtain the best possible time resolutions. For the BaF<sub>2</sub> detector, the CFD threshold was set to -40 mV and the shaping delay to 5 ns. All detectors were running with count rates of about 4 kHz and the coincidence rate was about 30 Hz.

The analogue time difference between the BC501A and BaF<sub>2</sub> detectors was obtained by using an Ortec 566 TAC (500 ns range). The start and stop signals of the TAC were the CFD signals from

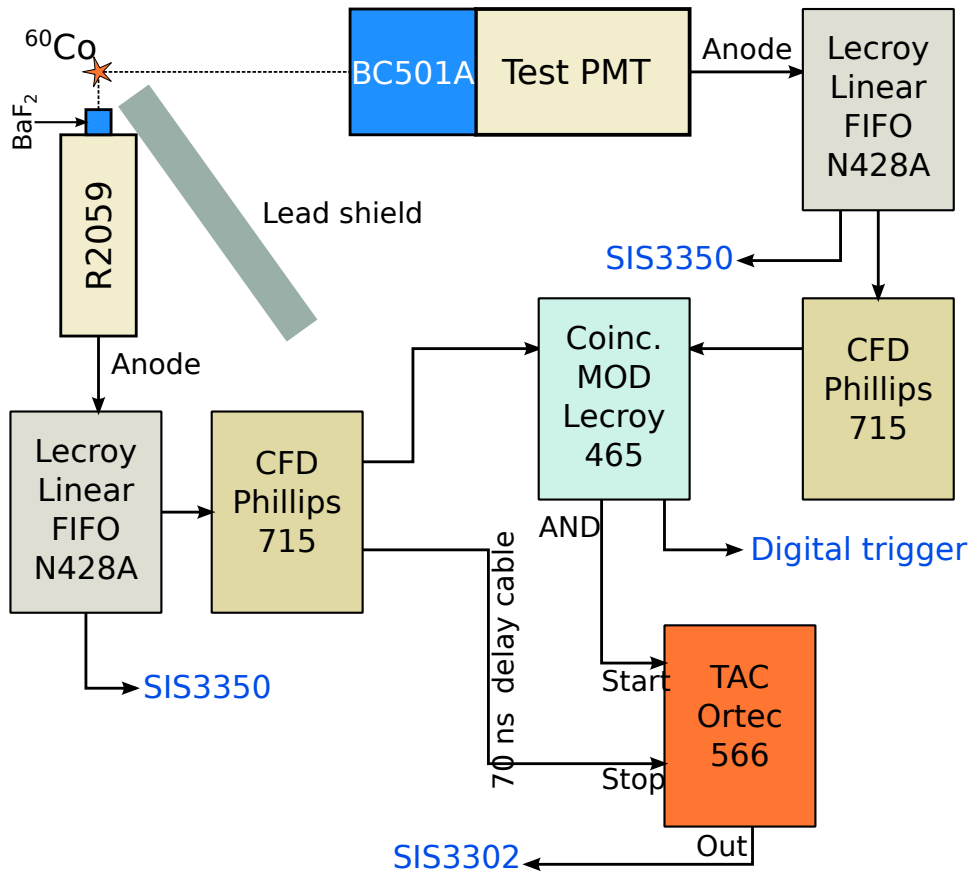


Figure 54: Schematic picture of the setup employed for the pulse-timing measurements. The analogue and digital electronics chains are indicated.

the BC501A and BaF<sub>2</sub> detectors, respectively. For the stop signal, a delay of 70 ns was used. The start signal was only produced if it overlapped in time with a wide BaF<sub>2</sub> signal in the coincidence unit LeCroy 465. A signal from this unit was also used as a trigger for the data acquisition system. The detector waveforms were digitised with a sampling ADC of model Struck SIS3350, a VME unit with four channels, each with a sampling frequency of 500 MS/s, a resolution of 12 bits (9.2 ENOB) and a dynamic range of 2 V. The analogue output signal from the TAC was digitised with a Struck SIS3302 sampling ADC (single width 6U VME, 8 channels, 100 MS/s, 16 bit). The digitisers were read out through the VME bus and the data were sent to the data acquisition system via a Struck SIS3100 controller using an optical link. The pulse-timing properties of the 5 inch PMTs were studied at the sampling rates 500 MS/s and 200 MS/s. The original waveforms, sampled at 500 MS/s were down-sampled to 200 MS/s, using as a filter a discrete averaging with an effective cut-off frequency at 100 MS/s. The signal from the BaF<sub>2</sub> detector was sampled at 500 MS/s and no down-sampling was performed for this detector.

## 10.2 Results and Discussion

In this section, the time resolutions obtained with the digital method will be discussed and compared with the results from the analogue measurements.

Fig. 55 shows the waveforms for the four tested PMTs, averaged over  $10^5$  signals, from the 500 MS/s digitiser. Average rise times of 4.9(4) ns, 3.8(3) ns, 6.3(7) ns, 13.5(13) ns, are measured with the XP4512, R4144, R11833-100 and ET9390-kb PMTs, respectively. The results are shown in Table 9. For the fastest PMTs, a 500 MS/s sampling rate provides only two or three sampling points in the

Table 8: High voltage (HV) settings of the PMTs, threshold and shaping delay ( $\Delta$ ) values used by the analogue CFD.

Detector	HV [V]	Threshold [mV]	$\Delta$ [ns]
R2059/BaF <sub>2</sub>	-1806	-40(5)	5
XP4512	-1140	-35(5)	10
R4144	-1452	-40(5)	10
R11833-100	-1390	-40(5)	12
ET9390-kb	-1206	-30(5)	25

rising edge of the signal. Thus, accurate timing algorithms should preferably use sampling points in a range larger than what is available in the rising edge of the signal.

Table 9: Measured rise times, blue photocathode sensitivity ( $S_{pc}$ ), number of photoelectrons per MeV (NPE, see Sec. 11.3), and time resolution of the tested PMTs. An energy threshold of 100 keV was applied.

PMT	Rise time	$S_{pc}$	NPE	Time resolution (FWHM) [ps]		
	[ns]	[ $\mu A/lm$ ]	[1/MeV]	Analogue	500 MS/s	200 MS/s
XP4512	4.9(4)	10.6	1330(70)	690(30)	660(30)	740(30)
R4144	3.8(3)	10.2	950(60)	750(30)	710(30)	870(30)
R11833-100	6.3(7)	13.5	1830(90)	743(13)	730(20)	760(20)
ET9390-kb	13.5(13)	12.0	1550(50)	1470(20)	1330(30)	1360(20)

Fig. 56 shows the rise time extracted from the digitised waveforms as a function of the signal amplitude. As seen in the figure, there is no appreciable dependence of the rise time on the signal amplitude for any of the PMTs, which shows that the constant fraction is a suitable technique for these signals.

Digital constant fraction algorithms have already been studied in different systems, such as 100 MS/s sampled waveforms from charge sensitive preamplifiers [73], or for signals from BaF<sub>2</sub> scintillators [66]. This algorithm has also been implemented digitally on FPGA devices employing a linear interpolation of the zero crossing [74]. However, the cubic spline interpolation for pulse timing has been shown to improve the resolution considerably in certain systems [73]. Consequently, a constant fraction algorithm was developed in this work with the zero-crossing time determined using a cubic spline interpolation, with continuous first and second derivatives.

A zero-crossing signal  $ZC_i$  is created by summing the original waveform  $S_i$  multiplied by a factor  $\chi$  and its inverted signal delayed by an integer number of samples  $\Delta$ :

$$ZC_i = \chi (S_i - BS) - (S_{i-\Delta} - BS). \quad (11)$$

The baseline  $BS$  is first calculated and then subtracted from both the delayed and scaled components. The zero-crossing point is then obtained by interpolating between the first negative sample and the preceding sample, at a reference height of 5 mV over the baseline. The interpolation consists of a cubic spline employing 6 sampling points, with continuous first and second derivatives ( $C^2$ ). The delay  $\Delta$ , together with the factor  $\chi$  were chosen in order to optimise the time resolution of each PMT. With this two-parameter digital method, the best timing result was obtained for all PMTs by using a slightly shorter delay compared to the shaping delay used for the analogue CFD module.

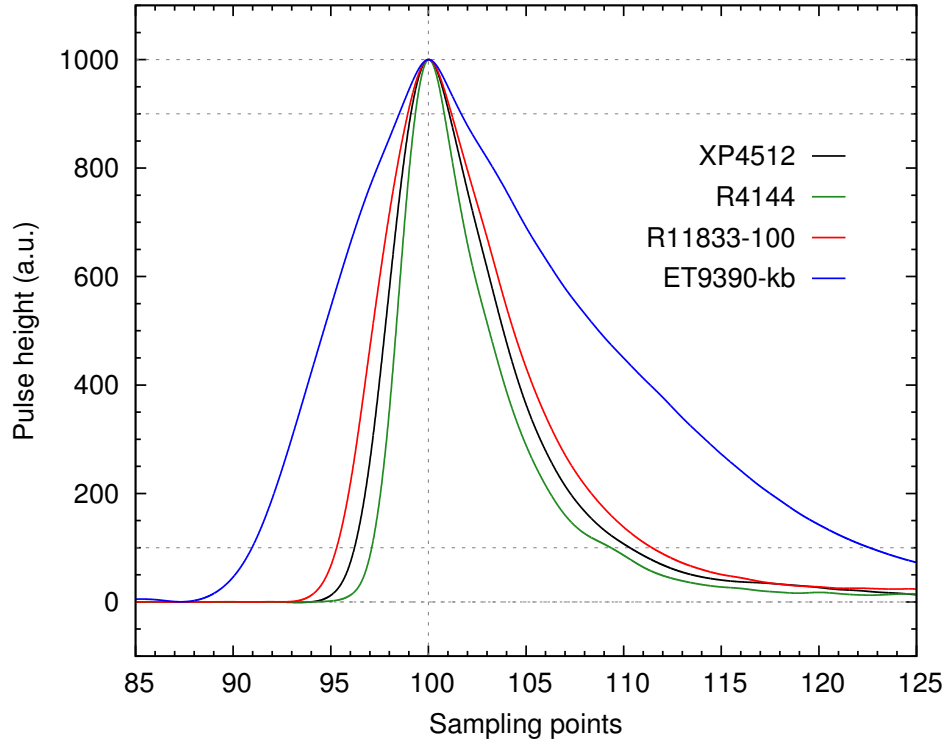


Figure 55: Digitised waveforms averaged over  $10^5$  events for the four 5 inch PMTs coupled to a cylindrical 5 inch by 5 inch BC501A. The sampling frequency of the digitiser was 500 MS/s. The waveforms were normalised to a pulse height of 1000 and time aligned at the maximum of the signal. Dashed lines are drawn at 10 % and 90 % of the rise time, at the maximum and at the baseline of the waveform to guide the eye.

Fig. 57a shows an example of the waveform  $S_i$ , the scaled signal  $\chi \cdot S_i$ , the delayed and inverted signal  $-S_{i-\Delta}$ , and the resulting zero-crossing signal  $ZC_i$  measured with the PMT R11833-100. The grey area highlights the six sampling points used for the zero-crossing interpolation. It contains all the samples in the leading edge of the delayed and inverted signal. The cubic spline interpolation  $C^2$  was compared with a cubic spline interpolation  $C^1$  (continuous only up to the first derivative), in which four points were employed, and with a linear interpolation.

Fig. 57b shows as an example the time distribution obtained for the PMT R11833-100 with the three different interpolations at a sampling rate of 200 MS/s and with a threshold of 100 keV. The use of a cubic spline interpolation improved significantly the time resolution with respect to the linear one: the FWHM was 1460(120) ps with the linear interpolation, 920(20) ps with the cubic spline interpolation  $C^1$  and 775(15) ps with the cubic spline interpolation  $C^2$ . The use of six sampling points and a  $C^2$  cubic function, led to much better results when the sampling rate was lowered. Fig. 57.c shows the time resolution for the cubic interpolations at the sampling rates 500 MS/s and 200 MS/s for the PMT R11833-100. While both algorithms achieve the same time resolution at 500 MS/s, the  $C^2$  cubic spline interpolation improves the time resolution by 15 % compared to the  $C^1$  interpolation at 200 MS/s.

The time resolutions of all four PMTs, using both analogue and digital electronics, were evaluated from time distributions containing  $10^5$  events. One additional measurement was performed by using two XP4512 PMTs and two cylindrical 5 inch by 5 inch BC501A detectors. This was done in order to estimate the contribution of the BaF<sub>2</sub> reference detector to the evaluated time resolutions. The result obtained was that the FWHM of the BaF<sub>2</sub> detector was at most 200 ps.

Fig. 58 shows the time resolution as a function of signal amplitude in keV for the four tested



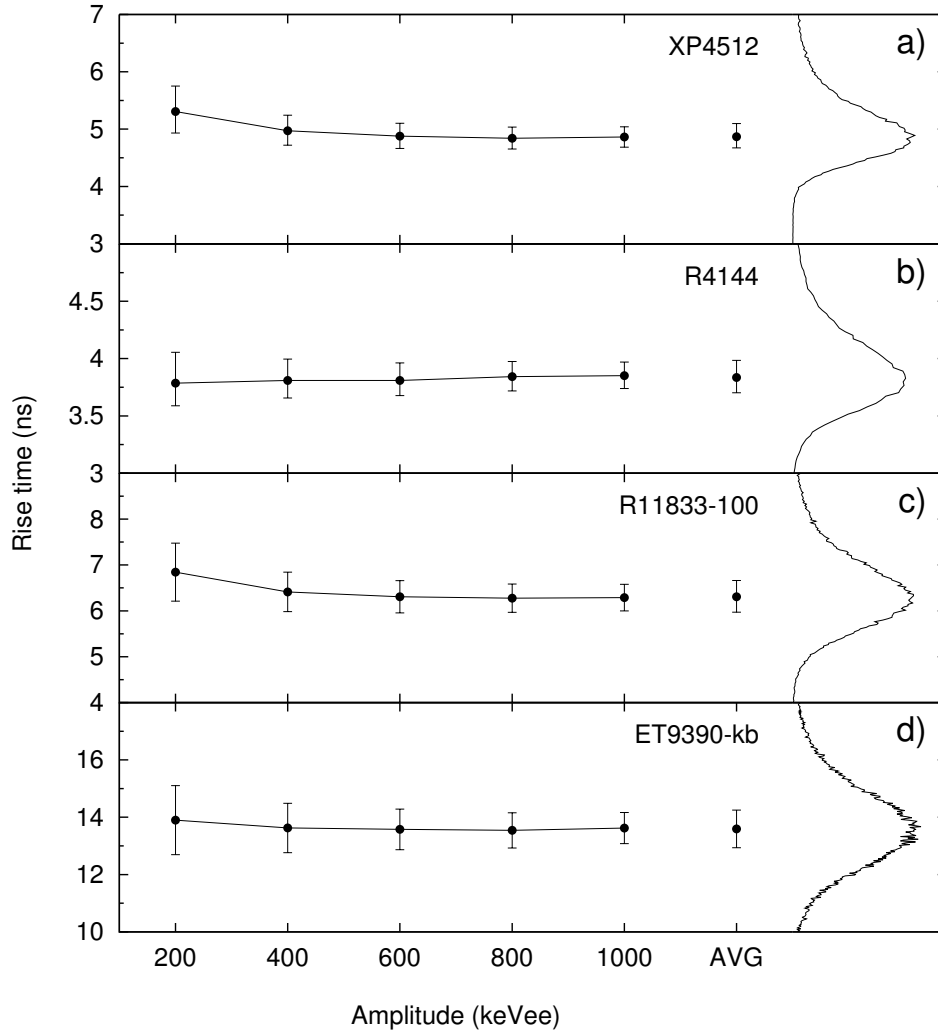


Figure 56: Rise time as a function of the signal amplitude determined from the digitised waveforms for PMT a) XP4512, b) R4144, c) R11833-100 and d) ET9390-kb. The width of the amplitude windows was 100 keV. The values obtained for all amplitudes above a threshold of 100 keV are shown at the x-axis position labeled AVG and the rise-time distributions for this case are plotted on the right hand side. Error bars indicate the  $1\sigma$  width of the rise-time distributions.

PMTs and measured with both analogue and digital electronics at the sampling rates 500 MS/s and 200 MS/s. For all measurements, the time resolutions achieved with the digital system at 500 MS/s was at least as good as the ones obtained with the analogue electronics. For signals with large amplitudes, the time resolution of the digital system at 500 MS/s was better than the analogue one for the XP4512 and R4144 PMTs.

It may be noticed that the intrinsic time resolution of the analogue and digital modules is considered similar, and negligible with respect to the nanosecond range of the time resolution for the whole system. For example, the time resolution of a pulser digitised with a 250 MS/s FADC is  $\approx 60$  ps [75], a value which is similar to the time walk of commercial analogue CFD modules.

A summary of the time resolutions obtained with the analogue and digital systems at a threshold of 100 keV, is shown in Table 9. For all measurements, the FWHM refers to the total resolution of the system, including the contribution from the BaF<sub>2</sub> reference detector. The digital performance of each PMT is correlated with the signal rise time and the number of photoelectrons. On one hand, the PMTs XP4512, R4144 and R11833-100, with rise times 4.90(44) ns, 3.8(3) ns, 6.30(77) ns, respectively, achieve a similar average time resolution of better than FWHM = 750 ps with analogue

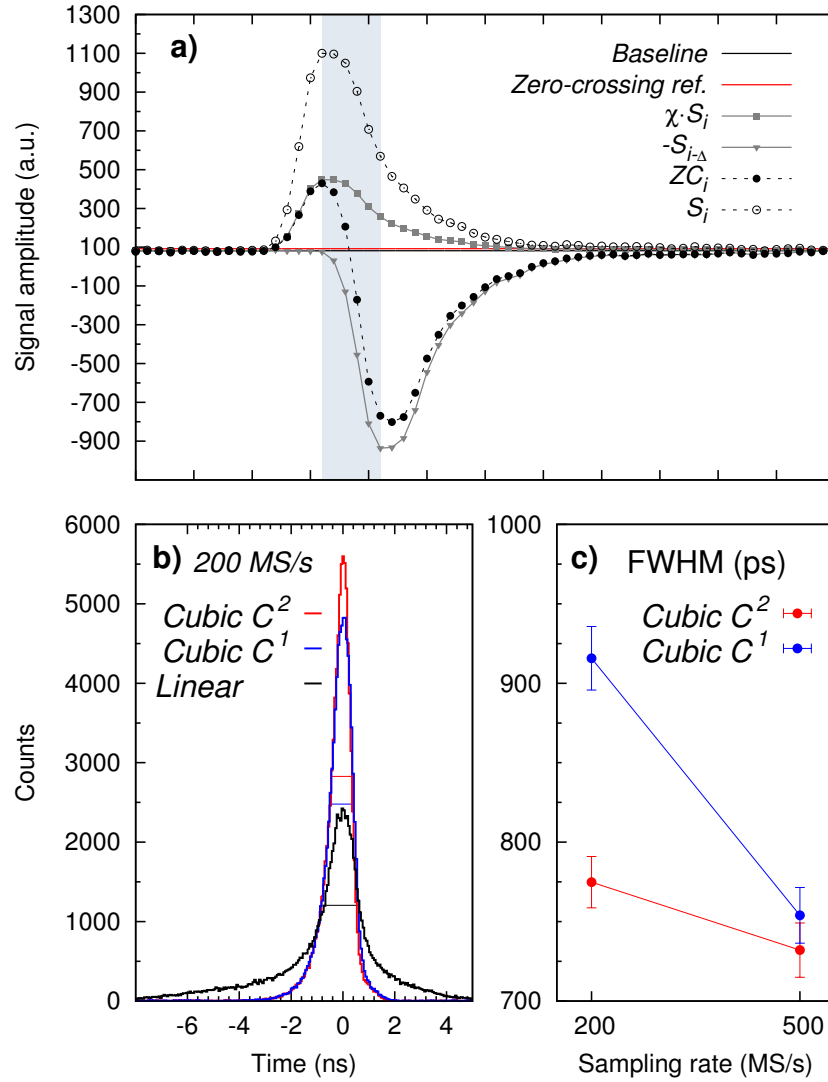


Figure 57: Illustration of the digital constant fraction algorithm. a) An example of a waveform and its zero-crossing signal, measured with the R11833-100 PMT at a sampling rate of 500 MS/s. The horizontal black line is the baseline and the horizontal red line is the reference to get the zero-crossing. The grey area indicates the samples used for the cubic interpolation  $C^2$ . b) Time-difference distribution obtained with the R11833-100 PMT at 200 MS/s using the linear, cubic  $C^1$  and cubic  $C^2$  interpolations. c) Time resolution as a function of sampling frequency for the R11833-100 PMT using cubic  $C^1$  and  $C^2$  interpolations.

electronics. The worse time resolution for the ET9390-kb, with a FWHM of 1470 ps, is due to its significantly larger signal rise time of 13.5(13) ns. On the other hand, the time resolution strongly depends on the number of photoelectrons (NPE, see Sec. 11.3) emitted from the photocathode. This is translated to a dependency in energy as  $1/\sqrt{E}$  [76], making also the PMT blue photocathode sensitivity  $S_{pc}$  an important parameter for the time resolution. The R11833-100 and ET9390-kb PMTs are slower, but have higher  $S_{pc}$  values, than the other two PMTs (see Table 9). Therefore they exhibit less degradation in time resolution when down-sampling from 500 MS/s to 200 MS/s.

The increase of the FWHM values at the very end of the Compton edge (above 800 keV, see Fig. 58) is worth noticing. This is interpreted as being due to multiple-Compton scattering of  $\gamma$  rays inside the detector. In such cases, the production of light at two (or more) locations inside the scintillator worsens the time resolution.

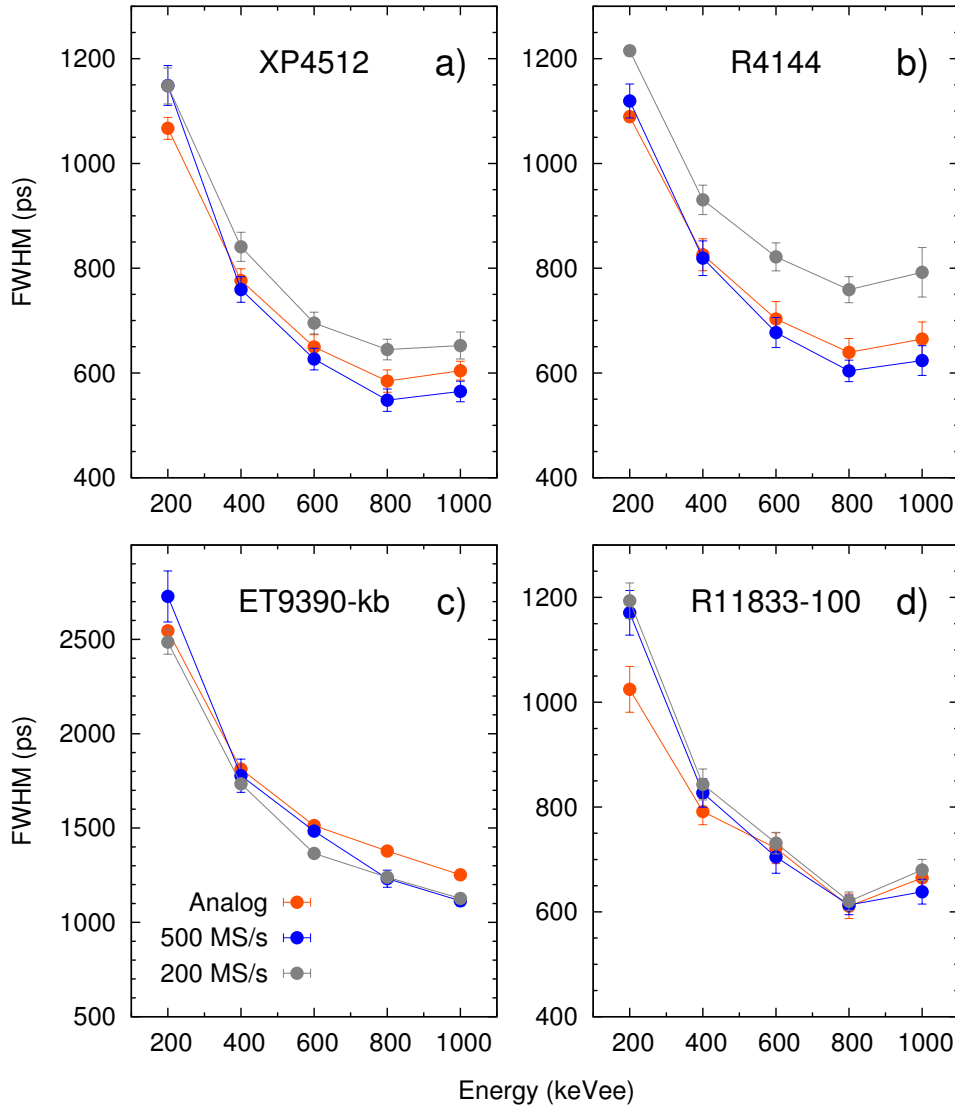


Figure 58: Time resolutions (FWHM) measured with a) XP4512, b) R4144, c) ET9390-kb and d) R11833-100 PMTs as a function of the waveform amplitude. blue: 500 MS/s, grey: 200 MS/s, red: analogue.

### 10.3 Conclusions

In summary, the timing performance of four 5 inch photomultiplier tubes (XP4512, R4144, R11833-100, ET9390-kb), connected to a cylindrical 5 inch by 5 inch BC501A scintillator detector, were measured by using digital electronics and a BaF<sub>2</sub> detector as time reference. The detector waveforms were digitised by a flash ADC with a resolution of 12 bits and sampling frequency of 500 MS/s. Measurements were also performed with a sampling frequency down-sampled to 200 MS/s. A CFD algorithm, consisting of a zero-crossing signal obtained as a cubic spline interpolation continuous up to the second derivative, was applied on the digitised waveforms. The obtained time resolutions were compared to the results obtained with a standard analogue CFD. Similar time resolutions were achieved with the analogue measurement and the digital measurement at 500 MS/s, with only a small degradation at 200 MS/s. Among the four different PMTs tested, the XP4512 and R11833-100 PMTs performed slightly better at 200 MS/s compared to the other models, giving a FWHM value that was lower than 800 ps. From the present digital measurements, one can state that the use of a digitiser with a sampling rate of 200 MS/s and a resolution of 12 bits will give a time resolution for the detectors of the future NEDA array that is as good as what can be obtained with standard

1396 analogue CFDs.

## 1397 11 Optimal Photomultiplier Tube for Neutron-Gamma Discrimina- 1398 tion

1399 This section describes the work performed to find a suitable 5 inch diameter PMT for NEDA [72].  
1400 The neutron- $\gamma$  discrimination (NGD) performance of a BC501A liquid scintillator detector coupled  
1401 to four different PMTs, with characteristics given in Table 10, were tested extensively.

Table 10: The characteristics of the studied 5 inch photomultiplier tubes. The given values for the anode pulse rise time are taken from the data sheets provided by the manufacturers. The measured rise times are considerably larger than these values, mainly due to the fact that the PMTs are coupled to a large scintillator [77].

PMT	ET9390kb	R11833-100	XP4512	R4144
Manufacturer	ET Enterprises	Hamamatsu	Philips/Photonis	Hamamatsu
Photocathode material	bialkali	superbialkali	bialkali	bialkali
Quantum efficiency [%]	28	35	24	22
Number of dynode stages	10	8	10	8
Anode pulse rise time [ns]	5	4.3	2.5	1.5
Voltage divider model	C636	E6316-01MOD2	VD123K (active)	E7693MOD2

### 1402 11.1 Experiment

1403 The measurements were carried out at INFN-LNL in Legnaro, Italy. The experimental setup is  
1404 illustrated in Fig. 59. All four tested PMTs have a diameter of 5 inches and were coupled to the  
1405 same cylindrical cell containing BC501A scintillator liquid, 5 inches in diameter and 5 inches in depth.  
1406 The BC501A detector was placed at 50 cm from a  $^{252}\text{Cf}$  source to detect the neutrons. The activity  
1407 of the source was about 2 MBq. The high voltage of the PMT was set to get a signal amplitude  
1408 of about 1 V/MeV for each PMT using a  $^{60}\text{Co}$  source. All PMTs were shielded with  $\mu$  metal from  
1409 magnetic fields. A lead brick with a thickness of 5 cm was put between the source and the BC501A  
1410 detector. This shielding reduced the count rate due to  $\gamma$  rays without losing too many neutrons, thus  
1411 keeping the count rate of the PMT at a reasonable value of around 2 kHz. In addition, a cylindrical  
1412 1 inch by 1 inch  $\text{BaF}_2$ , mounted on a 2 inch PMT R2059, was placed as close as possible to the  
1413  $^{252}\text{Cf}$  source for detection of  $\gamma$  rays, which provided a time reference for the time-of-flight (TOF)  
1414 measurements. A time-to-amplitude (TAC) module was used to measure the time difference between  
1415 the two detectors, using the coincidence signal (leading edge defined by the BC501A detector) as  
1416 start, and a delayed signal from the  $\text{BaF}_2$  detector as stop.

1417 The threshold of the CFD was set to approximately 30 keVee (keV electron equivalent). The counting  
1418 rate of the  $\text{BaF}_2$  detector was 200 kHz and the coincidence rate was 200 Hz. Signals from both  
1419 detectors were digitised with a Struck SIS3350 digitiser [46] working at a 500 MS/s sampling rate  
1420 and with 12 bit resolution (effective number of bits = 9.2). The analogue TAC and coincidence  
1421 signals were also digitised by a Struck SIS3302 digitiser [48] with 100 MS/s sampling rate and  
1422 16 bit resolution (effective number of bits 13). The data acquisition system was triggered by the  
1423 coincidence signals [78]. In this study, the digital signals from the BC501A detector, together with  
1424 the TOF information, were used for NGD. For each PMT, a total of 100000 pulse events were  
1425 analysed in the present work. The total numbers of recorded sampling points were 496 and 488 for

1426  
1427  
1428

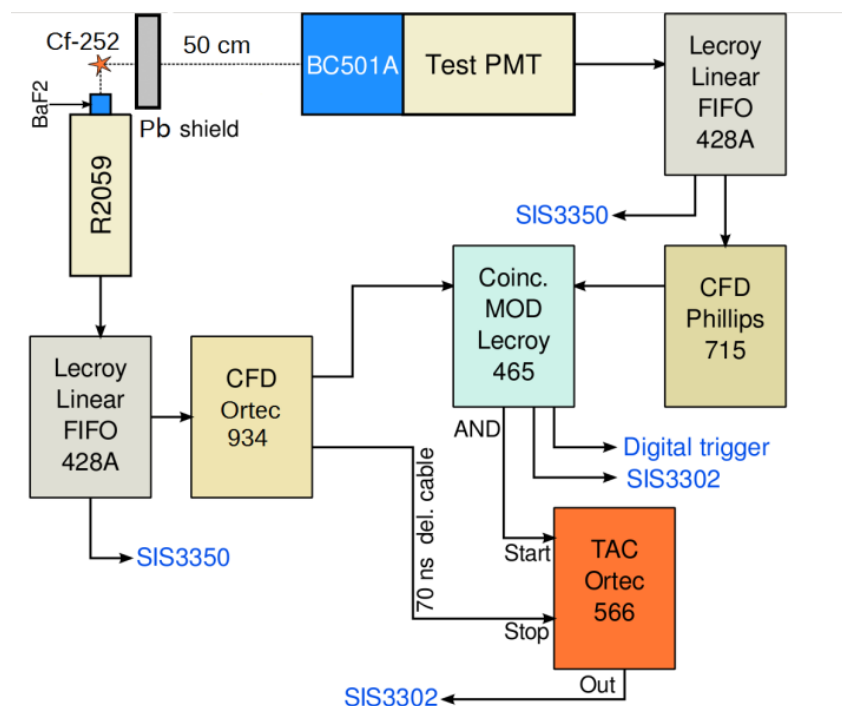


Figure 59: Block scheme of the experimental arrangement.

## 1429

1430  
1431  
1432  
1433  
1434  
1435  
1436  
1437  
1438  
1439  
1440  
1441  
1442  
1443  
1444

## 1445

1446  
1447  
1448  
1449

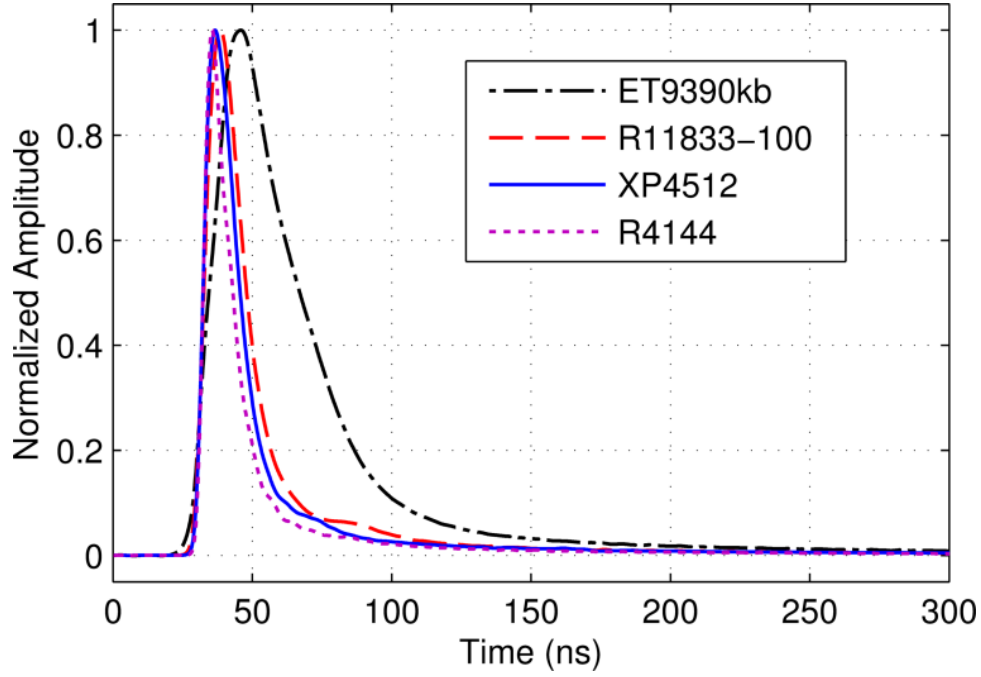


Figure 60: Average waveforms for PMTs ET9390kb, R11833-100, XP4512, and R4144 (100,000 pulses for each PMT) time-aligned using a digital CFD algorithm.

was measured by comparing the position of the peak corresponding to a single photoelectron to the position of the Compton edge of  $\gamma$ -ray emitted by a  $^{137}\text{Cs}$  source [80]. The results of the NPE measurement for the four PMTs are shown in Table 11. The NPE per MeV values are relatively low, because the photoelectron yield of large volume scintillators is reduced due to light attenuation inside the scintillator [71].

Table 11: Number of photoelectrons per  $\gamma$ -ray energy deposition for the four different PMTs.

PMT	NPE/MeV
ET9390kb	$1800 \pm 90$
R11833-100	$2070 \pm 100$
XP4512	$1350 \pm 70$
R4144	$950 \pm 60$

## 11.4 Digital NGD

In this section, two conventional pulse-shape discrimination methods, charge comparison (CC) and integrated risetime (IRT), have been implemented digitally to discriminate neutrons from  $\gamma$  rays. They are based on the principle that the fraction of light that appears in the slow component of the light yield of the liquid scintillators depends on the type of incident particle. In order to quantify the NGD performances of the four PMTs, a parameter named figure-of-merit (FOM) was used to evaluate the results of these two pulse-shape discrimination methods in sections 11.4.1 and 11.4.2. The FOM is defined as [79]

$$\text{FOM} = \frac{S}{W_{\gamma} + W_n}, \quad (12)$$

where  $S$  is the distance between the neutron and  $\gamma$ -ray peaks in the distribution spectrum of the discrimination parameter, and  $W_\gamma$  and  $W_n$  are their full width at half maximum values. A larger value of FOM normally indicates a better performance of the NGD. However, it should be noted that the FOM only measures the degree of separation that can be achieved between different types of event distributions and does not take into account any mis-identification cases. This means that in some extreme situations, even a poor NGD with a high mis-identification rate could still have a fairly large FOM value, though this is unlikely to happen as long as the pulse-shape discrimination method has been implemented properly. For example, the mis-identification due to pile-up effects is quite common when the count rate is very high, while the two peaks of the distribution spectrum of the discrimination parameter are well separated, resulting in a large FOM. Therefore, in section 11.4.3 the TOF information was included to further verify the validity of both the CC method and the IRT method used in this work.

#### 11.4.1 Pulse-shape Discrimination with the CC Method

The CC method identifies the particle by measuring the integrated charge over two different time regions of the pulse induced by a neutron or  $\gamma$ -ray event. The long integral (total charge) starts from the beginning of the pulse (8 ns before the CFD trigger point) to an optimised end point in the tail, while the short integral corresponding to the slow component is taken from an optimised start point after the pulse peak to the same end point as used for the long integral. The optimal start point of the short integral ( $t_s$ ) and the end point of both the short and long integrals ( $t_e$ ) were determined carefully by performing a maximisation of FOM value when leaving both  $t_s$  and  $t_e$  as free variables. Fig. 61 presents a three-dimensional plot of this process of optimising  $t_s$  and  $t_e$  using the CC method for PMT ET9390kb at  $(320 \pm 20)$  keVee as an example. The optimal values of  $t_s$  and  $t_e$  were set to 90 ns and 300 ns respectively. For  $t_e$ , the FOM did not improve for larger values than 300 ns. The value of  $t_e$  was kept constant at 300 ns in all cases to ensure as short time interval as possible for minimising pile-up effects. This is reasonable as the intensity of the slow component of the light pulse is quite low beyond 300 ns [13].

Fig. 62 shows the comparison of two-dimensional density plots of short integral versus long integral of each pulse measured with PMT ET9390kb, R11833-100, XP4512 and R4144 using an energy threshold of 100 keVee. It can be observed that even with such a large scintillator an effective separation between neutron and  $\gamma$ -ray events has been accomplished down to 100 keVee for each PMT. Since the relative intensity of the slow component of the pulse arising from neutrons (recoil protons) is larger than that of  $\gamma$  rays (electrons), the events located in the upper distribution in Fig. 62 were identified as neutrons while the lower distribution corresponds to  $\gamma$  rays according to the CC method.

Furthermore, the NGD performance was evaluated as a function of energy by employing different energy windows between 50 keVee and 1000 keVee in order to get a more quantitative comparison of the discrimination capability. Fig. 63 presents the NGD spectra, which are the distributions of the ratios of short to long integrals being measured at  $(320 \pm 20)$  keVee for the different PMTs. Gaussian functions were used to fit the distributions with the curve fitting tool available in MATLAB [81]. The FOM values were then extracted from these Gaussian fits for all the PMTs by applying eq. (12). The optimal  $t_s$  and the extracted FOM values are shown in the legends of Fig. 63.

The FOMs in different energy regions ranging from 50 keVee to 1000 keVee for all PMTs have been obtained in the way as shown in Fig. 63. The comparison of the measured FOMs of the CC method for each tested PMT is shown in Fig. 64. As seen in this figure, the FOM values rise gradually with increasing energy as expected for all PMTs. ET9390kb and R11833-100 generally perform best in terms of NGD with only slight difference in FOM values. The PMT XP4512 is slightly worse than R11833-100 and ET9390kb, while R4144 gives considerably lower FOMs compared to other PMTs indicating its poorest NGD capability. This trend of FOMs for different PMTs qualitatively agrees



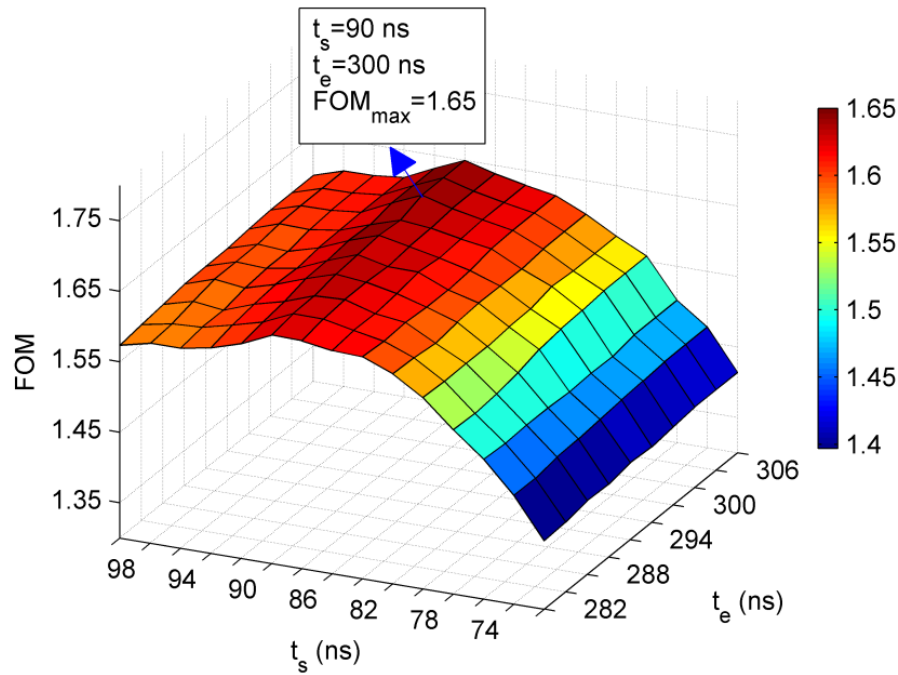


Figure 61: FOM values measured for PMT ET9390kb at  $(320 \pm 20)$  keVee as a function of  $t_s$  and  $t_e$  used in the CC method.

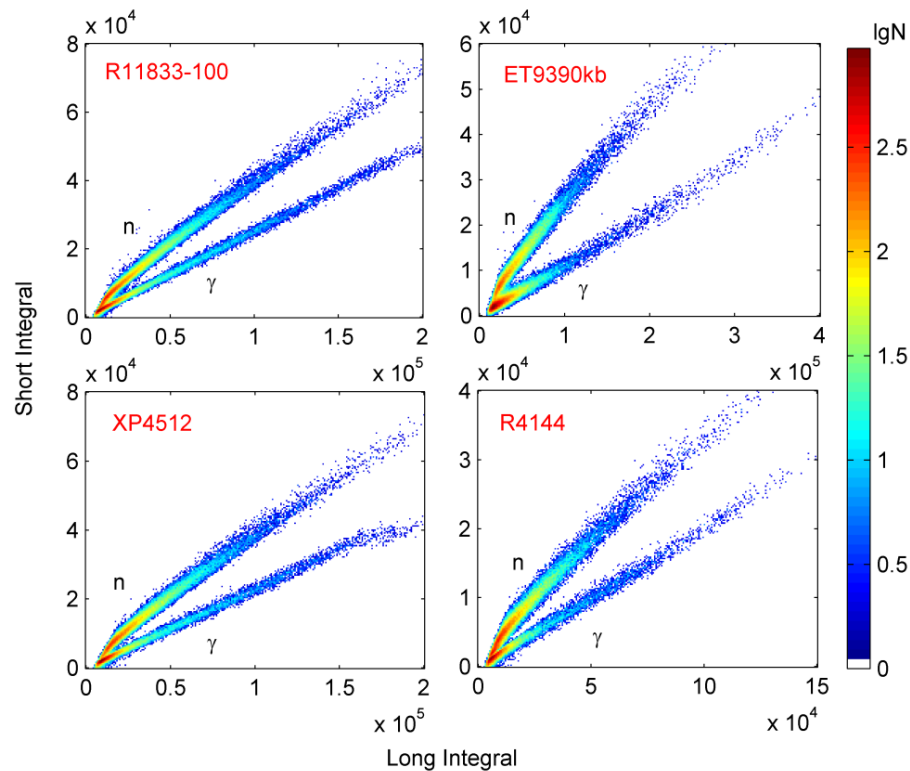


Figure 62: Density plots of short integral versus long integral of each pulse measured with PMT ET9390kb, R11833-100, XP4512 and R4144 with an energy threshold of 100 keVee.

1511 with the measured number of photoelectrons per MeV (Table 11). The error of FOM was calculated  
 1512 based on eq. (12) by propagating the errors of the parameters derived from the non-linear iterative



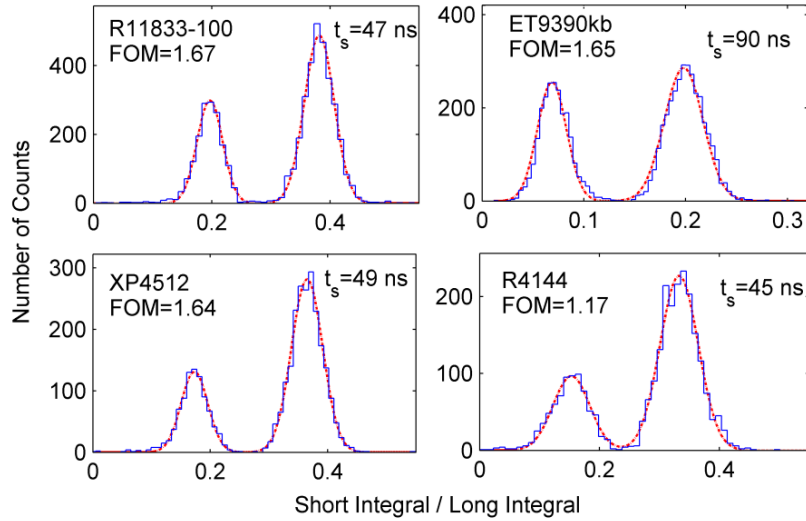


Figure 63: NGD spectra with fitted Gaussian distributions at  $(320 \pm 20)$  keVee using the CC method for PMT ET9390kb, R11833-100, XP4512 and R4144.

1513 curve fit.

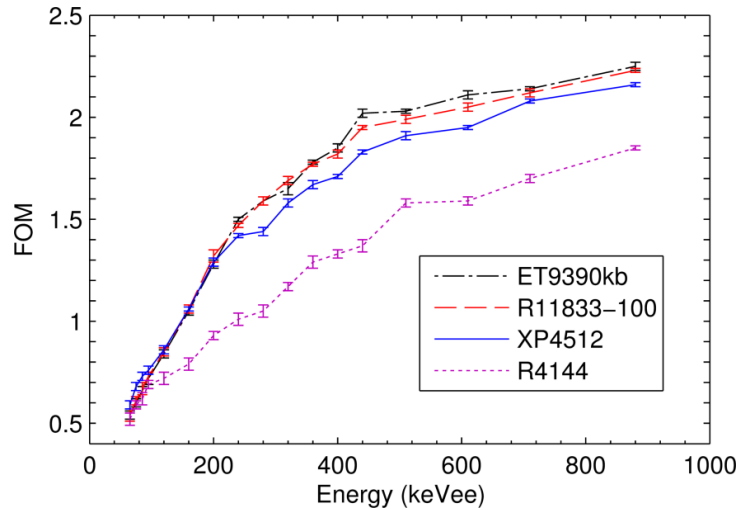


Figure 64: FOM values of the CC method for PMT ET9390kb, R11833-100, XP4512, and R4144 as a function of energy window. The widths of the windows are 10 keVee, 40 keVee, and 100 keVee in the energy regions 50 keVee - 100 keVee, 100 keVee - 500 keVee and 500 keVee - 1000 keVee, respectively.

#### 1514 11.4.2 Pulse-Shape Discrimination with the IRT Method

1515 The IRT method can be seen as a digital implementation of the analogue zero-crossover (ZCO)  
 1516 method since the integrated rise time can be evaluated directly by digital signal processing rather  
 1517 than first shaping it to extract the ZCO time. The rise time, defined here as the time difference  
 1518 between the point when the integrated pulse crosses a lower fraction and an upper fraction of its  
 1519 maximal amplitude, is used as a parameter to distinguish neutrons from  $\gamma$  rays. The optimisation  
 1520 of lower and upper points was performed in the same way as for the CC method as illustrated in  
 1521 Fig. 61. The optimal values of the lower/upper points for PMT ET9390kb, R11833-100, XP4512  
 1522 and R4144 were found to be 10%/92%, 11%/86%, 10%/84% and 12%/87% of the maximal  
 1523 amplitude, respectively. The principle of the IRT method is that the integrated rise time of the

neutron-induced pulse is longer than that of the  $\gamma$ -ray induced pulse.

Conventionally, the performance of an NGD method can be assessed qualitatively by plotting the amplitude of a given pulse against its discrimination parameter [58, 59, 82, 83, 84, 85]. Fig. 65 presents the comparison of two-dimensional density plots of amplitude against the integrated rise time of each pulse measured with PMT ET9390kb, R11833-100, XP4512 and R4144 using an energy threshold of 100 keVee. In each plot of Fig. 65, the events on the right hand were identified as neutrons and the left groups of events were regarded as  $\gamma$  rays.

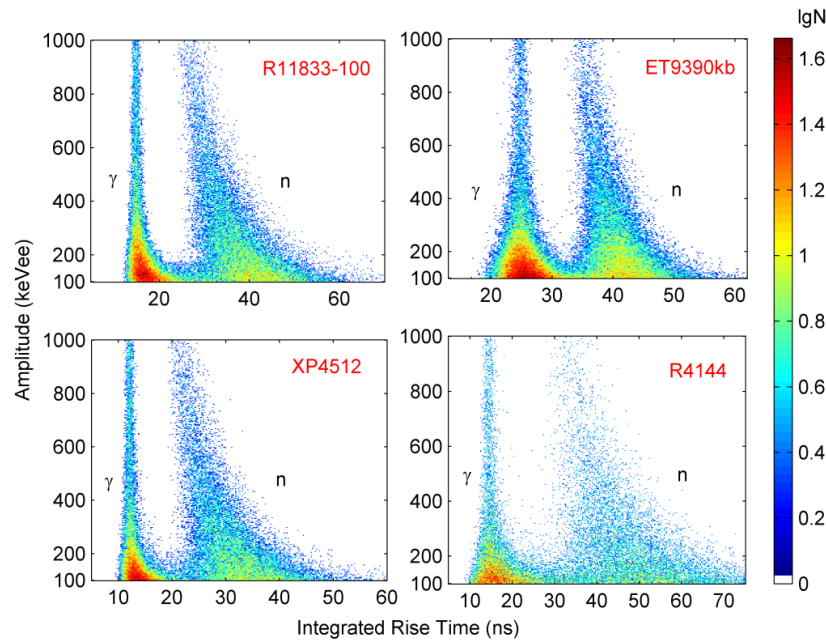


Figure 65: Density plots of amplitude versus the integrated rise time of each pulse measured with PMT ET9390kb, R11833-100, XP4512 and R4144 with an energy threshold of 100 keVee.

Like the CC method, the NGD quality was assessed as a function of energy for each PMT. Fig. 66 presents the NGD spectra which are the projections of the integrated rise time being measured at  $(320 \pm 20)$  keVee for the different PMTs. As seen in Fig. 66, the FOMs for each PMT have been extracted with Gaussian fits of the two peaks of the distribution curve corresponding to the  $\gamma$ -ray and neutron events.

Fig. 67 presents a quantitative comparison of the IRT discrimination performance of each PMT in terms of FOM in different energy regions between 50 keVee and 1000 keVee. It can be observed that the trend of FOMs of the IRT method for different PMTs is basically consistent with that of the CC method. Nevertheless, the FOMs of IRT method for R11833-100 are slightly higher than those for ET9390kb, while in the CC method ET9390kb is a little better regarding FOM values. Since these differences are insignificant when taking into account the error of the FOM values, it can be safely concluded that R11833-100 and ET9390kb have the best capabilities of NGD. In general, the IRT method performs slightly better than the CC method over most of the energy range for all PMTs, with the FOM values on average about 7 %, 4 %, 3 % and 6 % higher for PMT R11833-100, ET9390kb, XP4512 and R4144, respectively. This is probably because the IRT method can cancel out part of the high-frequency noise present in the signal by integrating the pulse. Yet at the same time, it should be noted that the FOMs of different PMTs under 100 keVee are quite similar, all suggesting deterioration in NGD performance at low energy. This results from the fact that the signal-to-noise ratio of the low energy signals is quite low due to the scintillation statistics and due to the electronic noise and the quantisation effects of the digitiser, which is a fundamental limitation of any discrimination method [86].

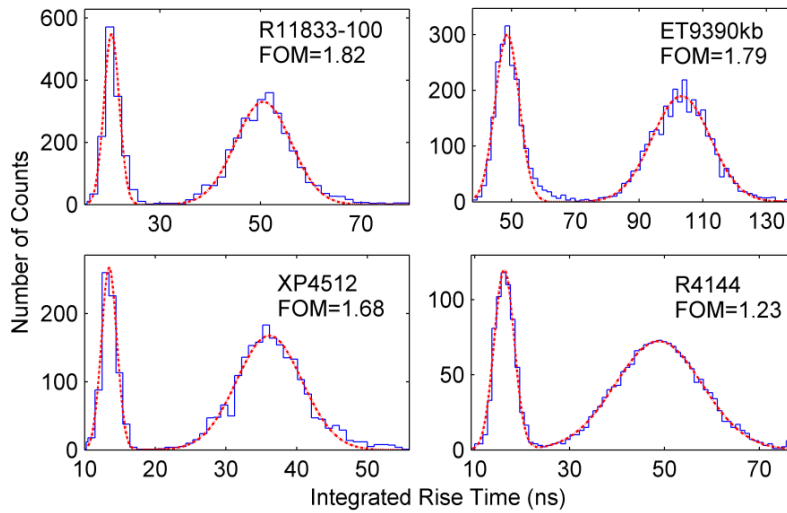


Figure 66: NGD spectra with fitted Gaussian distributions at  $(320 \pm 20)$  keVee using the IRT method for PMT ET9390kb, R11833-100, XP4512 and R4144.

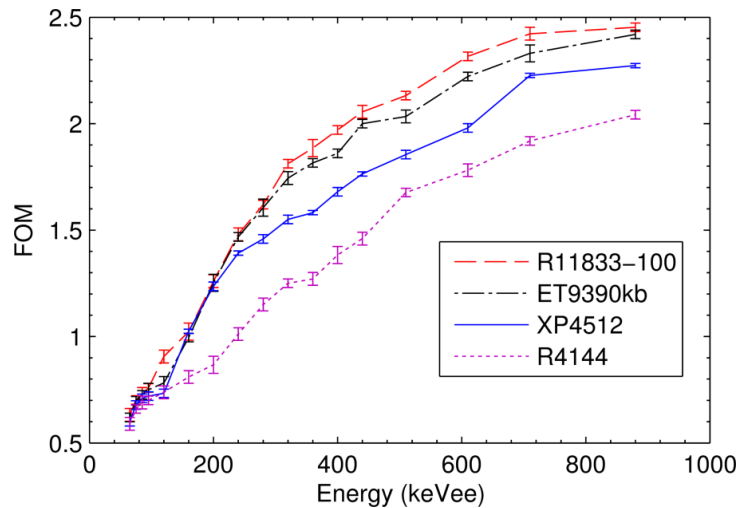


Figure 67: FOM values of the IRT method for PMT ET9390kb, R11833-100, XP4512, and R4144 as a function of energy window. The widths of the windows are 10 keVee, 40 keVee, and 100 keVee in the energy regions 50 keVee - 100 keVee, 100 keVee - 500 keVee and 500 keVee - 1000 keVee, respectively.

### 11.4.3 TOF Verification of NGD

Neutrons and  $\gamma$  rays can often be distinguished with a high accuracy by measuring their TOF between the emission point and the detector. Thus, the TOF parameter was used here, combined with both the CC method and the IRT method, to evaluate their discrimination quality on a qualitative basis. Fig. 68 presents the TOF distribution of the pulses measured with PMT XP4512. Density plots of the NGD parameter of the CC method and the IRT method versus the TOF measured with the PMT XP4512 are shown in Fig. 69 and Fig. 70, respectively. Two distinct clusters of events are clearly visible as areas of higher density centered at TOF values of  $\approx 0$  and  $\approx 0.38$ , each of which correspond to  $\gamma$  rays and neutrons respectively. This indicates that the NGD results of both the CC method and the IRT method are similar to that of TOF measurement, which has demonstrated qualitatively the correctness of the implementation of these two methods in sections 11.4.1 and 11.4.2.

However, there are some other events located elsewhere in Fig. 69 and Fig. 70, most of which are

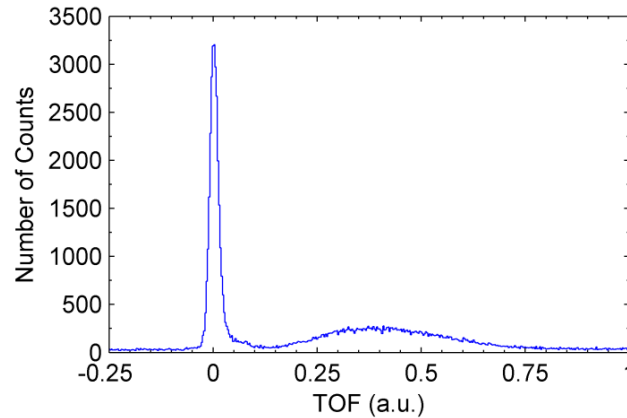


Figure 68: TOF spectrum of the pulses measured with PMT XP4512.

random and pile-up events. In Fig. 70, for instance, random events are mainly distributed parallel to the TOF axis. The TOF method failed to classify these events because TOF measurements require a time reference that is unavailable for them, whereas the IRT method can discriminate them based on the pulse shape. Moreover, the region with an integrated rise time larger than  $\approx 20$  ns and TOF of about 0 mostly contains pile-up events, because they tend to have longer integrated rise time, which results in the discrepancy between the NGD results of the TOF method and the IRT method. The reason for the invalidation of the IRT method in discriminating these events is that the original pulse shape has to some extent been distorted by pile up. Therefore, it is suggested that if available in a real experiment, pulse-shape discrimination and TOF measurement should complement each other to acquire relatively pure neutrons or  $\gamma$  rays.

## 11.5 Summary and Conclusions

In summary, a comparative study was made with four different PMTs (ET9390kb, R11833-100, XP4512 and R4144) with a diameter of 5 inches regarding the NGD performances when coupled to the same liquid scintillator detector, with a size of 5 inches in diameter and 5 inches in depth. The analysed waveforms were acquired with an experimental setup that comprised a  $^{252}\text{Cf}$  source, a BC-501A detector and a SIS3530 digitiser with a sampling rate of 500 MS/s and with 12 bit resolution. Firstly, the average waveforms as well as the photoelectron yield were measured and an energy calibration was made for each PMT. Secondly, both the CC method and the IRT method were implemented digitally to discriminate neutrons from  $\gamma$  rays. The FOM parameters were evaluated as a function of energy to quantitatively compare the NGD properties of the four PMTs. Finally, the NGD results were verified by combining the TOF measurement with both the CC method and the IRT method. The results suggest that an effective NGD can be achieved down to 100 keVee for all four PMTs. In general, PMT R11833-100 and ET9390kb have the best NGD capabilities with only slight difference in FOM values between them. The surprising result that the slow PMT ET9390kb can accomplish the NGD as well as the fast PMT R11833-100 is likely because the timing property of ET9390kb is sufficiently good for NGD. Therefore, the results are more associated with their relatively higher photoelectron yield per energy unit, which indicates that a scintillator detector coupled to a PMT with higher photoelectron yield can result in better NGD performance.

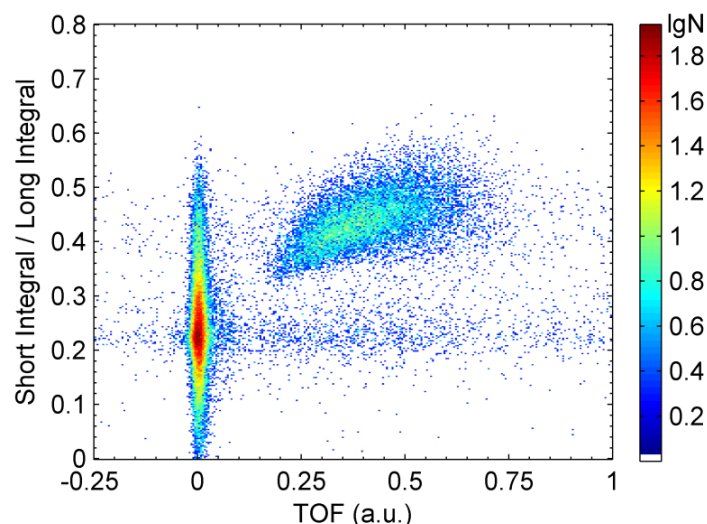


Figure 69: Density plot of the discrimination parameter of the CC method versus the TOF of each pulse measured with PMT XP4512. No energy threshold was set in the analysis.

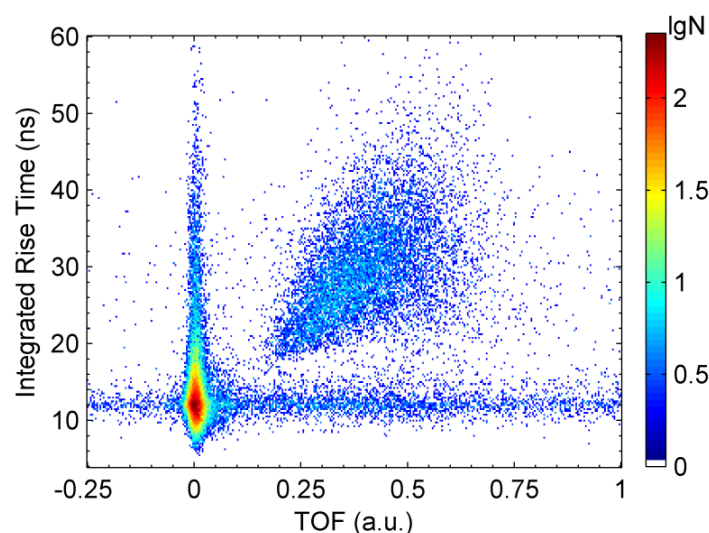


Figure 70: Density plot of the discrimination parameter of the IRT method versus the TOF of each pulse measured with PMT XP4512. No energy threshold was set in the analysis.

## 12 Detector Unit: Prototype Design and First Tests

This section describes the mechanical design of the NEDA prototype detector unit and the first test results obtained with the prototype.

### 12.1 Mechanical Description

The NEDA detector unit (cell) has the shape of a uniform hexagonal prism, with a side-to-side distance of 146 mm and a length of 205 mm (external dimensions). The active volume of the liquid scintillator is 3.2 litres. The mechanical design is made to reduce as much as possible the cost of the production process. Both the detector cell and the PMT housing are made by an extrusion of an Al-6060 bulk. The scintillator cell is constructed as shown in Fig. 71 by welding a bottom lid and a top flange (TIG welding) to the cylinder. The top flange holds an N-BK7 glass window with

a thickness of 8 mm and diameter of 133 mm. The glass window is bonded to the top flange with a 3.5 mm thick glue. Once mounted, the glass window stands out 1 mm from the flange, and has a 127 mm diameter (5 inch) for the light read out. The cell is internally painted with a  $\text{TiO}_2$ -based reflective paint.

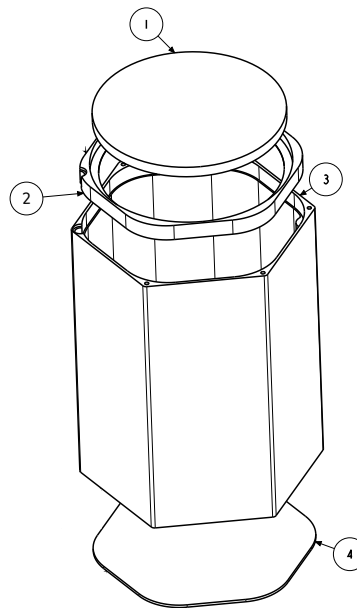


Figure 71: Exploded view of the NEDA cell showing 1) glass window, 2) top flange, 3) cylinder and 4) bottom lid.

The expansion chamber consists of a 3 inch diameter edge-welded steel bellow placed at the rear part of the PMT housing. The bellow has a stroke of 4.8 cm, which corresponds to a  $152 \text{ cm}^3$  volume difference. The pipe connecting the bellow with the cell has a flexible part to allow detaching the PMT housing. The flange on the top of the PMT housing holds a plastic ring to push the PMT against the glass window. All pieces of the prototype unit are shown in Fig. 72.

## 12.2 Test of Timing Performance

The analogue and digital time resolution of the prototype detector, coupled to a 5 inch photomultiplier tube of model R11833-100, was measured using a  $^{60}\text{Co}$  source and a 1 inch by 1 inch  $\text{BaF}_2$  detector as time reference. A setup identical to the one described in Sec. 10 was employed, see Fig. 54. The digital time resolution was obtained from the waveforms of both the prototype and of the  $\text{BaF}_2$  detector sampled at 500 MS/s, using a digital CFD algorithm with a cubic interpolation of the zero crossing (see Sec. 10.2 for details). Preliminary results of the measured time resolution (FWHM) as a function of signal amplitude are shown in Fig. 73. Even though the time resolution of this large volume detector is degraded by about 35 %, compared to what was obtained with a smaller 5 inch by 5 inch neutron detector tested in Sec. 10, the obtained overall time resolution with a  $^{60}\text{Co}$  source and an energy threshold of 100 keV is smaller than 1.2 ns (FWHM) both in the analogue and the digital measurements. Both the NEDA prototype detector and the 5 inch by 5 inch cell exhibit the same dependence of time resolution on energy.

## 12.3 Test of Neutron-Gamma Discrimination Performance

A test of the NGD capability of the NEDA prototype detector was performed using a  $^{252}\text{Cf}$  source, placed at a distance of 1 m from the detector. The setup of the electronics and data acquisition was



Figure 72: A photograph of the first NEDA prototype detector unit without liquid. Once filled with liquid, the pipe, the bellow and the cell are bonded together.

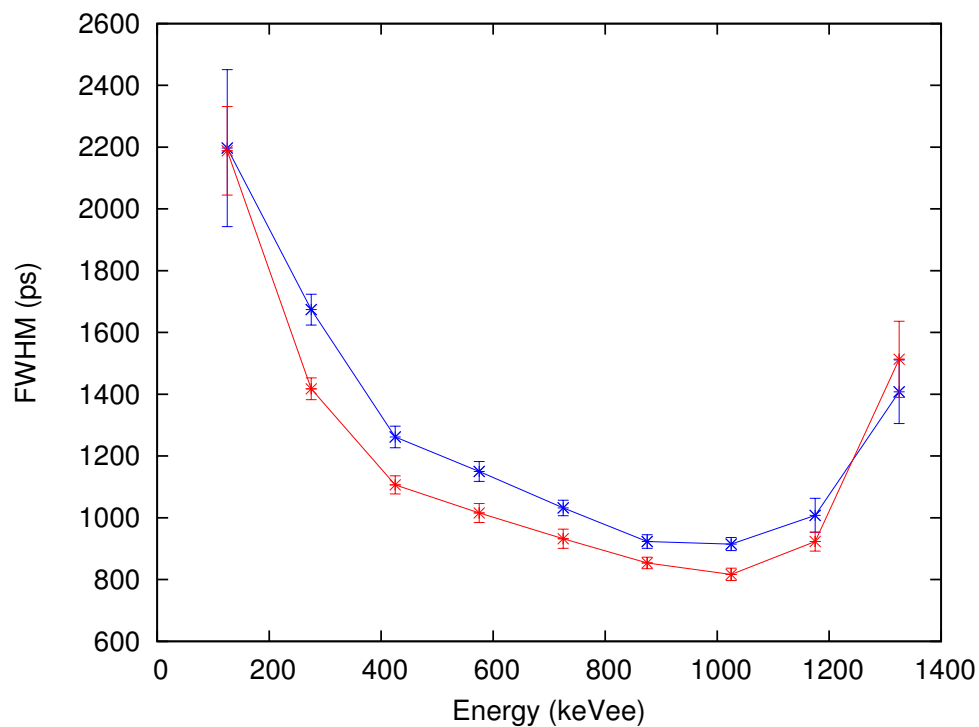


Figure 73: Time resolution (FWHM) versus signal amplitude measured with a  $^{60}\text{Co}$  source, the NEDA prototype detector and a  $\text{BaF}_2$  detector. The width of the energy windows was 100 keV. Blue: digital measurements. Red: analogue measurements. The results are preliminary.

1627 identical to the one used in the time-resolution measurements described in Sec. 12.2. The digital  
 1628 CC method was used to distinguish neutrons and  $\gamma$ -rays. The charge was integrated in two time  
 1629 gates:  $Q_{\text{slow}}$ , with a 400 ns width starting at 18 ns from the maximum of the signal, and  $Q_{\text{fast}}$ , with



a 30 ns width ending where  $Q_{\text{slow}}$  starts. Preliminary results are shown in figure 74.

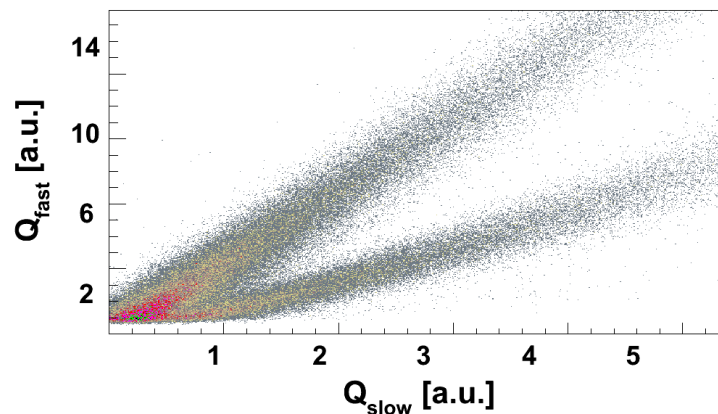


Figure 74: Neutron- $\gamma$  discrimination of the NEDA prototype detector using the digital charge-comparison method. See text for the definition of  $Q_{\text{fast}}$  and  $Q_{\text{slow}}$ . The results are preliminary.

These preliminary results show that the PSA performance is according to expected results for a cell of this volume (about 3 litres).

## 13 New Detector Materials

Recently, a new solid organic scintillator with good NGD properties has been developed [87] and become available on the market. The NGD capabilities of a cylindrical 3 inch diameter detector of type EJ299-33 was investigated within the NEDA collaboration, with the aim of finding out if this material would be a possible future upgrade for NEDA [88]. The results showed that the NGD quality is not quite as good as what is obtained with the best liquid scintillators available, but encouraging enough that the NEDA collaboration will keep a close eye on the developments of this material. If it improves, it may be that NEDA in a future upgrade would use the new solid scintillator instead of the liquid scintillator that currently has been chosen.

## 14 NEDA Organisation, Phases, Work Packages and Time Lines

### 14.1 Organisation, management, responsible persons

The organisation, management and responsible persons of the NEDA project are the following:

- **NEDA Project Manager:** J.J. Valiente Dobón, INFN-LNL, Italy.
- **NEDA Management Board:** J.J. Valiente Dobón (chair), N. Erduran, G. de France, A. Gadea, M. Moszynski, J. Nyberg, M. Palacz, D. Tonev, R. Wadsworth.
- **NEDA@HISPEC Contact Person:** Johan Nyberg, Uppsala University.
- **Collaborating countries and institutes:** See section 2.2.

### 14.2 Memorandum of understanding (MoU)

An MoU for the NEDA Development period 2012-2015 has been signed by all parties from Bulgaria, France, Italy, Poland, Spain, Sweden, Turkey, and the UK. A new MoU for the next period of NEDA is currently being prepared.



### 14.3 NEDA Phases and Campaigns

NEDA will be built in the following phases:

0. Upgrade of the Neutron Wall to use the new NEDA digital electronics (50 channels).
1. Construction of a NEDA array consisting of 48 detectors that can be run standalone or combined with the Neutron Wall (50 detectors) to cover a solid angle of about  $2\pi$  with a target-detector distance of 50 cm (98 electronics channels).
2. Construction of the full NEDA array with about 331 detectors covering a solid angle of about  $2\pi$  at a target-detector distance of 100 cm.

The NEDA array will be used in experimental campaigns at various accelerator facilities, like NUSTAR/FAIR, SPIRAL2/GANIL, SPES/LNL, etc. Currently, the decided campaign is to use NEDA with up to 46 detectors plus the Neutron Wall, with 50 detectors, combined with AGATA at GANIL in 2016-2017. The new NEDA electronics will then be used for the first time. For this campaign, a total of 18 letters-of-intent have been presented at the AGATA at GANIL Physics Workshop in 2013. From 2018, a setup of NEDA with 48 detectors, will be ready to be used at NUSTAR/FAIR.

### 14.4 Work Packages

The table below shows the NEDA work packages. The project is organised in working groups (one working group per work package), which are coordinated by the persons given in the table.

Work Package	Coordinator
Physics	R. Wadsworth (York)
Simulations and conceptual design	M. Palacz (Warsaw)
Light readout	M. Moszyński (Swierk)
Front-end electronics and DAQ	A. Gadea (Valencia)
Pulse-shape analysis	J. Nyberg (Uppsala)
Synergies with other detectors	P. Bednarczyk (Kraków)

### 14.5 Time Lines and Critical Milestones

Fig. 75 displays the foreseen time plane for the development and construction of 48 NEDA detectors, which will be ready to be used at HISPEC from 2018. Here is a list of critical milestones of the NEDA@HISPEC project:

- Simulations to select the shape and dimensions of the NEDA detector unit, 2012.
- Selection of the type of liquid (BC501A or BC537), 2012.
- NEDA digitiser mezzanine developments and prototype tests, 2013/Q2.
- Selection of the type of photomultiplier and design of voltage divider, 2014/Q3.
- Conceptual design and simulations of the NEDA array, 2014/Q3.
- Production of the first NEDA digitiser, mezzanine board 2014/Q2, carrier board 2014/Q4.
- Design and tests of the NEDA prototype detector units, 2014/Q4.

- Serial production of NEDA detector units and digitisers, 2015-2016.
- Tests of the first complete NEDA detector unit and NEDA digitiser, 2015/Q1.
- Final tests of complete detectors with electronics, 2017.
- Ready for experiments with NEDA@HISPEC, 2018/Q1.

## 15 Cost Estimates and Expected Funding

The cost estimates and expected funding for NEDA@HISPEC are described in a separate document.

## References

- [1] S. Akkoyun et al., Nucl. Instr. Meth. A668 (2012) 26.
- [2] P. Golubev et al., Nucl. Instr. Meth. A 723 (2013) 55.
- [3] J. Dobaczewski et al., Phys. Rev. Lett. 72 (1994) 981.
- [4] J. Dobaczewski et al., Phys. Scr. T56 (1995) 72.
- [5] T. Otsuka et al., Phys. Rev. Lett. 104 (2010) 012501.
- [6] P. Adrich, Phys. Rev. Lett. 95 (2005) 132501.
- [7] D.D. Warner, J. Res. Natl. Inst. Stand. Technol. 105 (2000) 33.
- [8] D. Vretenar et al., Phys. Rev. Lett. 91 (2003) 262502.
- [9] K. Pham et al., Phys. Rev. C 51 (1995) 526.
- [10] G. Jaworski et al., Nucl. Instr. Meth. A 673 (2012) 64.
- [11] S. Agostinelli et al., Nucl. Instr. Meth. A506 (2003) 250.
- [12] E. Farnea et al. Nucl. Instr. Meth. A621 (2010) 331.
- [13] M. Moszyński et al., Nucl. Instr. Meth. A 350 (1994) 226.
- [14] J. Ljungvall, M. Palacz, and J. Nyberg, Nucl. Instr. Meth. A 528 (2004) 741.
- [15] K. Banerjee et al., Nucl. Instr. Meth. A 608 (2009) 440.
- [16] T. Hüyük et al., Conceptual Design of the NEutron Detector Array (NEDA) and an early implementation of NEDA with AGATA, to be submitted to Nucl. Instr. Meth. A.
- [17] J.G. del Campo and R.G. Stockstad, Oak Ridge National Laboratory, Report No. TM7295 (1981), unpublished.
- [18] P. Coelho et al. Nucl. Instr. Meth. A280 (1989) 270.
- [19] A. Di Nitto et al., Eur. Phys. J. A47 (2011) 83.
- [20] R. Moro et al., Eur. Phys. J. A48 (2012) 159.
- [21] A.J. Koning and J.P. Delaroche, Nucl. Phys. A713 (2003) 231.
- [22] R.D. Hoffman et al., Tech. Rep., LLNL (2006) 222275.
- [23] S.I. Al-Quraishi et al., Phys. Rev. C67 (2003) 015803.

- 1715 [24] A. Di Nitto et al., J. Phys. Conf. Ser. 267 (2011) 012053.
- 1716 [25] T. Hüyük et al., LNL Annual Report 2011 (2012) 62.
- 1717 [26] J. Cederkäll et al., Nucl. Instr. Meth. A 385 (1997) 166.
- 1718 [27] F. J. Egea et al., IEEE Trans. Nucl. Sci. NS-60 (2013) 3526.
- 1719 [28] F. J. Egea et al., A New Front-End High-Resolution Sampling Board for the New-Generation  
1720 Electronics of EXOGAM2 and NEDA Detectors, Proceedings of the 19th Real-Time Conference,  
1721 Nara, Japan, 2014, submitted.
- 1722 [29] F. Egea et al., A Digital Front-End Electronics for the Neutron Detector NEDA, Proceedings  
1723 of the 19th Real-Time Conference, Nara, Japan, 2014, submitted.
- 1724 [30] Ö. Skeppstedt et al., Nucl. Instr. Meth. A 421 (1999) 531.
- 1725 [31] L.P.G. Bardelli and G. Poggi, Nucl. Instr. Meth. A560 (2006) 270.
- 1726 [32] X. Grave et al., 14th IEEE-NPSS Real Time Conf. (2005) 119.
- 1727 [33] <http://narval.in2p3.fr/>.
- 1728 [34] B.G. Taylor, IEEE Trans. Nucl.Sci. 45 (1998) 821.
- 1729 [35] M. Bellato, Tech. Rep. hal-00729086, Nov. 2005.
- 1730 [36] M. Bellato et al., IEEE Trans. Nucl. Sci. 55 (2008) 91.
- 1731 [37] P. Garrett, Hyp. Int. 225 (2014) 137.
- 1732 [38] J. Wong et al., EPJ Web of Conferences 66 (2014) 11040.
- 1733 [39] P.-A. Söderström et al., LNL Annual Report 2011, 64.
- 1734 [40] A. Pipidis et al., LNL Annual Report 2010, 78.
- 1735 [41] P. Söderström et al., Pulse-shape discrimination of neutrons and  $\gamma$  rays in the liquid scintillators  
1736 BC501A and BC537, to be submitted to Nucl. Instr. Meth. A.
- 1737 [42] Saint Gobain Crystals, USA, BC501/BC501A/BC519 data sheet, [http://www.detectors.saint-](http://www.detectors.saint-gobain.com/)  
1738 [gobain.com/](http://www.detectors.saint-gobain.com/).
- 1739 [43] R. A. Cecil, B. D. Anderson, and R. Madey, Nucl. Inst. Meth. 161 (1979) 439.
- 1740 [44] F. Kuchnir and F. Lynch, IEEE Trans. Nucl. Sci. NS-15 (1968) 107.
- 1741 [45] Saint Gobain Crystals, USA, BC537 data sheet, <http://www.detectors.saint-gobain.com/>.
- 1742 [46] <http://www.struck.de/sis3350.htm>.
- 1743 [47] P.-A. Söderström, J. Nyberg, and R. Wolters, Nucl. Instr. Meth. A 594 (2008) 79.
- 1744 [48] <http://www.struck.de/sis3302.htm>.
- 1745 [49] D. Wolski et al., BARTEK NDE202 Manual, EUROBALL Neutron Detectors Electronics  
1746 (Świerk 2001).
- 1747 [50] J. Agramunt, A triggerless digital data acquisition system for nuclear decay experiments, Mas-  
1748 ter's thesis, Univesitat de Valencia, Valencia (2012).
- 1749 [51] G. Liu et al., Nucl. Instr. Meth. A 607 (2009) 620.
- 1750 [52] E. Ronchi et al., Nucl. Instr. Meth. A 610 (2009) 534.
- 1751 [53] S. Marrone et al., Nucl. Instr. Meth. A 490 (2002) 299.

- 1752 [54] C. Guerrero et al., Nucl. Instr. Meth. A 597 (2008) 212.
- 1753 [55] N. Kornilov et al., Nucl. Instr. Meth. A 497 (2003) 467.
- 1754 [56] D. Savran et al., Nucl. Instr. Meth. A 624 (2010) 675.
- 1755 [57] X. Luo, G. Liu, and J. Yang, Proceedings of the First International Conference on Pervasive  
1756 Computing, Signal Processing and Applications (PCSPA 2010), IEEE, 994.
- 1757 [58] B. Mellow et al., Nucl. Instr. Meth. A 578 (2007) 191.
- 1758 [59] M. Aspinall et al., Nucl. Instr. Meth. A 583 (2007) 432.
- 1759 [60] C. Xiaohui et al., Nucl. Instr. Meth. A 694 (2012) 111.
- 1760 [61] <http://root.cern.ch/root/html/TMultiLayerPerceptron.html>.
- 1761 [62] C. G. Broyden, J. Inst. Maths. Appl. 6 (1970) 76.
- 1762 [63] R. Fletcher, Comp. J. 13 (1970) 317.
- 1763 [64] D. Goldfarb, Math. Comp. 24 (1970) 23.
- 1764 [65] D. F. Shanno, Math. Comp. 24 (1970) 647.
- 1765 [66] M. A. Nelson et al., Nucl. Instr. Meth. A 505 (2003) 324.
- 1766 [67] M. Flaska et al., Nucl. Instr. Meth. A 729 (2013) 456.
- 1767 [68] M. Nakhostin and P. Walker, Nucl. Instr. Meth. A 621 (2010) 498.
- 1768 [69] M. Flaska and S. A. Pozzi, Nucl. Instr. Meth. A 599 (2009) 221.
- 1769 [70] Y. Kaschuck and B. Esposito, Nucl. Instr. Meth. A 551 (2005) 420.
- 1770 [71] M. Moszyński et al., Nucl. Instr. Meth. A 317 (1992) 262.
- 1771 [72] X. Luo et al., Nucl. Instr. Meth. A 767 (2014) 83.
- 1772 [73] L. Bardelli et al., Nucl. Instr. Meth. A 521 (2004) 480.
- 1773 [74] A. Fallu-Labruyere et al., Nucl. Instr. Meth. A 579 (2007) 247.
- 1774 [75] J. Agramunt, priv. comm. (2013).
- 1775 [76] B. Bengtson and M. Moszyński, Nucl. Instr. Meth. A 81 (1970) 109.
- 1776 [77] V. Modamio et al., Nucl. Instr. Meth. A (2014), submitted.
- 1777 [78] V. Modamio et al., LNL Annual Report 2012 (2013) 78.
- 1778 [79] G.F. Knoll, Radiation Detection and Measurement, Fourth Edition, Wiley, 2010.
- 1779 [80] M. Moszyński et al., Nucl. Instr. Meth. A 307 (1991) 97 .
- 1780 [81] MathWorks, <http://www.mathworks.com>.
- 1781 [82] M.J. Joyce et al., IEEE Trans. Nucl. Sci. 57 (2010) 2625.
- 1782 [83] G. Liu et al., IEEE Trans. Nucl. Sci. 57 (2010) 1682.
- 1783 [84] J. Yang et al., Chin. Phys. C36 (2012) 544.
- 1784 [85] K.A.A. Gamage et al., Nucl. Instr. Meth. A642 (2011) 78.
- 1785 [86] X.L. Luo et al., Nucl. Instr. Meth. A717 (2013) 44.
- 1786 [87] N. Zaitseva et al., Nucl. Instr. Meth. A 668 (2012) 88.

1787 [88] Q. Nishada, Master's thesis, Uppsala University (2014).

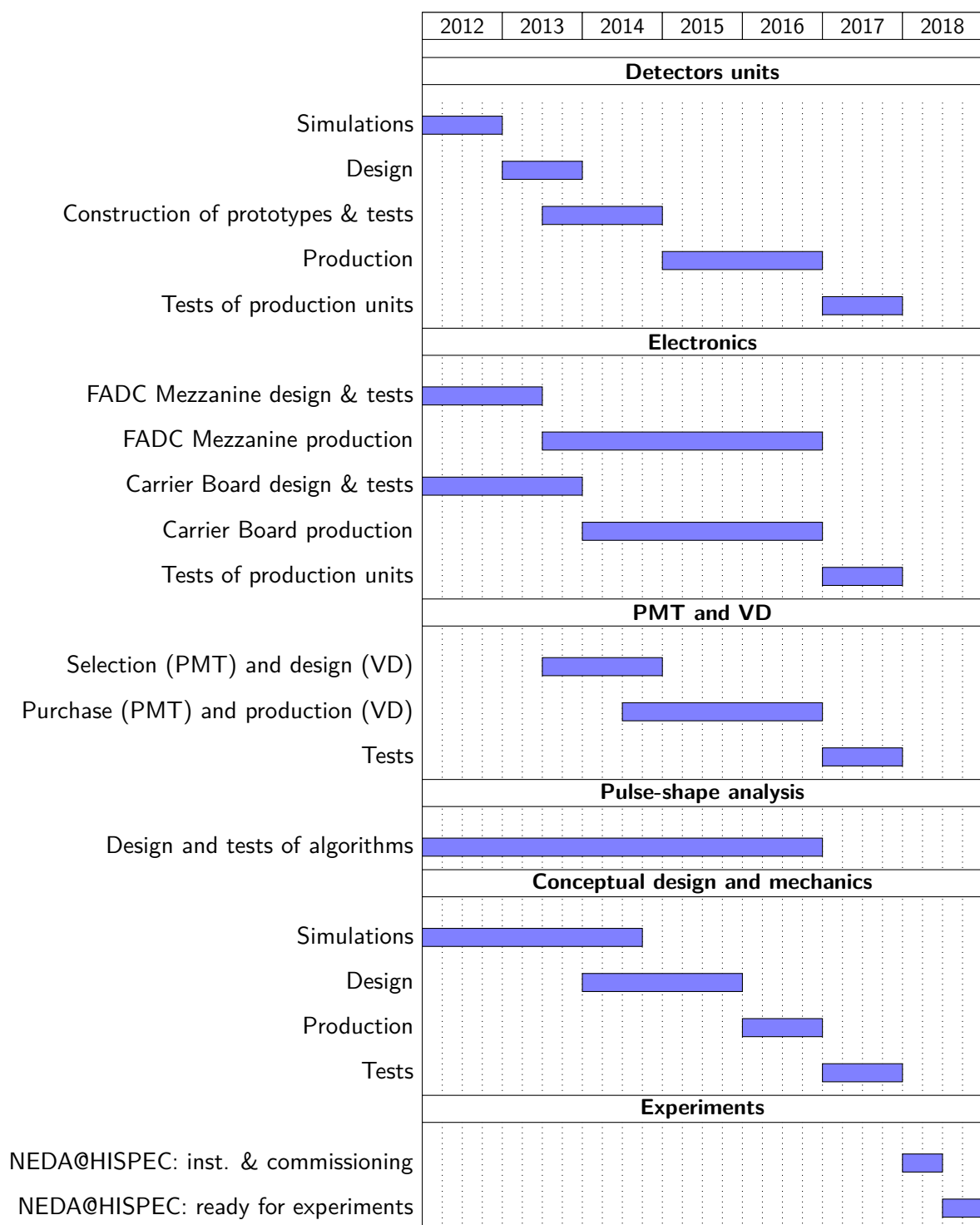


Figure 75: Time plan for the NEDA@HISPEC project.